

Mission Design for Safe Traverse of Planetary Hoppers

by

Babak E. Cohanim

B.S., Iowa State University (2002)
S.M., Massachusetts Institute of Technology (2004)

Submitted to the Department of Aeronautics & Astronautics
in Partial Fulfillment of the Requirements for the Degree of

Doctor of Science in Aeronautics & Astronautics
at the
MASSACHUSETTS INSTITUTE OF TECHNOLOGY

June 2013

© 2013 Babak E. Cohanim. All rights reserved

Signature of Author.....

Certified by.....

Thesis Committee Chairman: Jeffrey A. Hoffman
Professor of the Practice, Aeronautics & Astronautics

Certified by.....

Thesis Committee Member: Olivier L. de Weck
Associate Professor, Aeronautics & Astronautics and Engineering Systems

Certified by.....

Thesis Committee Member: David W. Miller
Professor, Aeronautics & Astronautics

Certified by.....

Thesis Committee Member: Tye M. Brady
Space Systems Group Leader, Draper Laboratory

Accepted by.....

Aeronautics & Astronautics Graduate Chairman: Eytan H. Modiano
Professor, Aeronautics & Astronautics

Mission Design for Safe Traverse of Planetary Hoppers

by

Babak E. Cohanim

Submitted to the Department of Aeronautics & Astronautics
on May 2013 in Partial Fulfillment of the
Requirements for the Degree of Doctor of Science in Aeronautics & Astronautics

ABSTRACT

Planetary hoppers are a new class of vehicle being developed that will provide planetary surface mobility by reusing the landing platform and its actuators to propulsively ascend, translate, and descend to new landing points on the surface of a planetary body. Hoppers enhance regional exploration, with the capability of rapid traverse over hundreds to thousands of meters, traverse over hazardous terrain, and exploration of cliffs and craters.

These planetary mobility vehicles are fuel limited and as a result are enabled by carrying sensor payloads that require low mass, low volume, and low onboard computational resources. This thesis describes methods for hoppers to traverse and land safely in this constrained environment.

The key questions of this research are:

- What types of missions will hoppers perform and how does a hopper traverse as part of these missions?
- How does a hopper traverse from its current location to a new landing site safely?

This thesis:

- describes various hopper mission scenarios and considerations for their mission designs
- creates an operational concept for safe landing for the traverse hop mission scenario
- develops a method that can be used to rapidly and safely detect landing areas at long ranges and low path angles
- develops a method to do fine detection of hazards once at the landing area

Thesis Supervisor: Jeffrey A. Hoffman

Title: Professor of the Practice of Aerospace Engineering

Keywords: hopper, hopping, planetary hopper, planetary hopping, lunar hopper, propulsive hopper, planetary mobility, Talaris hopper, hazard detection, hazard detection and avoidance, optical hazard detection, LIDAR, size density method, sparse slope and roughness

Table of Contents

Acronyms	8
Mathematical Symbols	9
1 Introduction	10
1.1 Motivation.....	11
1.2 Literature Review	15
1.3 Thesis Objectives.....	18
1.4 Thesis Overview	19
2 Current Methods for Landing and Traverse.....	20
2.1 Hoppers as an Extension of Landers	20
2.2 Techniques leveraged from Landers and Rovers.....	23
3 Hopper Mission Scenarios.....	31
3.1 Traverse Hop Scenarios.....	31
3.2 Steep Slope Exploration	35
3.3 Crater Exploration	36
3.4 Chapter 3 Summary	38
4 Landing Area Selection.....	39
4.1 Landing Area Selection Operational Concept.....	40
4.2 Size Density Method	43
4.3 Size Density Method Algorithm Description.....	45
4.4 Size Density Method Simulations and Results	56
4.5 Chapter 4 Summary	87
5 Landing Aim Point Selection	89
5.1 Sparse Slope & Roughness Operational Concept	90
5.2 Sparse Slope & Roughness Detection Method Description.....	93
5.3 Simulation Environment	96
5.4 Performance and Timing Analysis.....	102
5.5 Combined SDM and SSR Analysis.....	104
5.6 Chapter 5 Summary	109
6 Conclusions	111
6.1 Summary of Contributions.....	111
6.2 Future Work.....	112

6.3	Final Remarks	114
6.4	Acknowledgements.....	115
	Bibliography	116
	Appendix A – Surface Image Rendering.....	126

Tables in Thesis

Table 1	– Comparison of Planetary Exploration Systems	12
Table 2	– Navigation and Hazard Detection Architectures Past and Current.....	24
Table 3	– Sensors to Measurements.....	27
Table 4	– Relative Statistically Safety for Landing Area Selection	40
Table 5	– Cost Comparison for SDM vs. MDM.....	71
Table 6	– Timing analysis between DEM-based and Size Density Methods.....	73
Table 7	– View and Sun Angle Tradespace	75
Table 8	– Laser Range Sensors	89
Table 9	– Full tradespace results, combining SDM with SSR	106
Table 10	– Full tradespace results across all variables	107
Table 11	– Cost Comparison for Rendered vs. Real Image	133

Figures in Thesis

Figure 1	– Hopper Capabilities.....	11
Figure 2	– Modes of operation for hopper missions.	14
Figure 3	– Sun and View Elevation Angles affecting Apollo Missions.....	15
Figure 4	– Lunar Landing Trajectory.....	21
Figure 5	– Hop Trajectories: Phases, Times, Ranges, and Delta-Vs	22
Figure 6	– Hopper Actuator Configuration	23
Figure 7	– Hopper Architecture including Navigation Sensors	28
Figure 8	– Autonomy, Guidance, Navigation, and Control (AGNC) architecture for hoppers.....	29
Figure 9	– Landing Area Selection and Hazard Detection Operational Concept Illustration.....	32
Figure 10	– Ultraprecise landings using hopping (55).....	34
Figure 11	– Site Survey Hop Scenario	35
Figure 12	– Concept for navigating steep slopes using a short-range scanning LIDAR	36
Figure 13	– Simple and Complex crater morphology (106)	37
Figure 14	– Crater with prominent shadow.....	38
Figure 15	– Field of View, Landing Area, and Landing Aim Point	42
Figure 16	– Size Density Method illustration	43
Figure 17	– Grid cell definition.....	44
Figure 18	– Size Density Method Algorithm Flow Diagram	46
Figure 19	– Lunar image and corresponding image intensity histogram (Luna 23/24 region).....	46

Figure 20 – Binary feature map (Luna 23/24 photograph).....	47
Figure 21 – Vehicle Footprint Dispersion Ellipse (VFDE).....	48
Figure 22 – Gridding Geometry Parameter Diagram.....	49
Figure 23 – Field of View Angle Geometry.....	49
Figure 24 – Gridding Illustration.....	50
Figure 25 – Greedy Selection Flow Diagram.....	55
Figure 26 – “Spread” Parameter.....	56
Figure 27 – Angles for applying lighting conditions to DEMs.....	57
Figure 28 – Flow Diagram of Simulation Environment.....	58
Figure 29 – Flow diagram of DEM-based Hazard Detection Method.....	59
Figure 30 – Flow diagram of Modified DEM-based Hazard Detection Method.....	60
Figure 31 – Luna 23/24 DEM.....	61
Figure 32 – Luna 23/24 slope map.....	62
Figure 33 – Luna 23/24 roughness map.....	62
Figure 34 – Luna 23/24 blended hazard map.....	63
Figure 35 – Luna 23/24 MDM Frozen Cost Map.....	64
Figure 36 – Luna 23/24 MDM Weighted Cost Map.....	65
Figure 37 – Rendered image of the Luna 23/24 Landing Site.....	66
Figure 38 – Binary feature map (Luna 23/24 rendered image).....	66
Figure 39 – Luna 23/24 SDM Frozen Cost Map (for rendered image).....	67
Figure 40 – Luna 23/24 SDM Weighted Cost Map (for rendered image).....	68
Figure 41 – MDM vs. SDM Weighted Cost Maps.....	68
Figure 42 – MDM vs. SDM Weighted Cost Map differences.....	69
Figure 43 – Comparison of weighted cost maps for the SDM vs. MDM Luna 23/24 site.....	70
Figure 44 – Fraction of hazardous LAPs for Luna 23/24 Landing Areas.....	71
Figure 45 – SDM landing area rankings vs. absolute cost.....	72
Figure 46 – Varying values of N for SDM.....	74
Figure 47 – Landing area comparison for all sun and view angles.....	75
Figure 48 – Sun elevation angle images and weighted cost maps.....	76
Figure 49 – Landing area comparison for varying sun elevation angles.....	77
Figure 50 – Comparison of SunEL mean and STD to mean and STD of all points.....	78
Figure 51 – Kaguya Descent Imagery.....	79
Figure 52 – Sun azimuth angle images and weighted cost maps.....	80
Figure 53 – Landing area comparison for varying sun azimuth angles.....	81
Figure 54 – Comparison of SunAZ mean and STD to mean and STD of all points.....	82
Figure 55 – View Elevation angle images and weighted cost maps.....	83
Figure 56 – Landing area comparison for varying view elevation angles.....	84
Figure 57 – Comparison of ViewEL mean and STD to mean and STD of all points.....	85
Figure 58 – Illustration of shadows cast by rocks vs. craters.....	86
Figure 59 – Slope & Roughness Flow Diagram.....	89
Figure 60 – Illustration of Hopper Slope & Roughness Detection using a Range Sensor.....	90
Figure 61 – Illustration of Window of Regard for Slope & Roughness Detection.....	91

Figure 62 – Pointing geometry for slope and roughness range sensor	92
Figure 63 – Slope computed as angle between Normal and gravity vectors	93
Figure 64 – Slope & Roughness Simulation Environment Flow Diagram	97
Figure 65 – Slope & Roughness simulation output for timing analysis	98
Figure 66 – LA DEM1 from the Luna 23/24 region	99
Figure 67 – LA DEM1 truth slope and roughness map	99
Figure 68 – DEM1 safety map	100
Figure 69 – LA DEM1 SSR smooth map.....	100
Figure 70 – Estimated slope and roughness map using Sparse Slope & Roughness	101
Figure 71 – SSR LAPs	101
Figure 72 – Comparison of truth LAPs to SSR LAPs.....	102
Figure 73 – TP, TN, FN, FP as a function of scan density	102
Figure 74 – TP, TN, FN, FP as a function of scan density at half hazard tolerances.....	103
Figure 75 – Sparse Slope and Roughness algorithm run times for given scan densities.....	104
Figure 76 – Mare Crisium basin	104
Figure 77 – Landing Region 1	108
Figure 78 – Landing Region 1 selected Landing Area.....	108
Figure 79 – Landing Region 8	109
Figure 80 – Landing Region 8 selected Landing Area.....	109
Figure 81 – Illustration of Shadowing Algorithm	126
Figure 82 – Rendered traverse image of Luna 23/24 landing site	127
Figure 83 – Real image of the Luna 23/24 Landing Site (114)	128
Figure 84 – Rendered image of the Luna 23/24 Landing Site.....	129
Figure 85 – Real and Rendered Image Histograms.....	130
Figure 86 – Luna 23/24 DEM.....	130
Figure 87 – DEM vs. Rendered vs. Real Weighted Cost Maps	131
Figure 88 – DEM vs. Rendered vs. Real Weighted Cost Map differences.....	133
Figure 89 – Comparison of SDM Relative Costs to MDM Absolute Costs.....	134

Acronyms

ALHAT	Autonomous Landing and Hazard Avoidance Technology
DEM	Digital Elevation Map
DSN	Deep Space Network
FN	False Negative
FOV	Field of View
FP	False Positive
GLXP	Google Lunar X-Prize
GNC	Guidance, Navigation, and Control
GSD	Ground Sample Distance
HD	Hazard Detection
IMU	Inertial Measurement Unit
LA	Landing Area
LAP	Landing Aim Point
LIDAR	Light Detection and Ranging
LR	Landing Region
LRO	Lunar Reconnaissance Orbiter
MER	Mars Exploration Rovers (2004)
MDM	Modified DEM-based Hazard Detection Method
MSL	Mars Science Laboratory
SDM	Size Density Method
TALARIS	Terrestrial Artificial Lunar And Reduced Gravlty Simulator
TP	True Positive
TN	True Negative
TRN	Terrain Relative Navigation
T/W	Thrust-to-Weight Ratio
VFDE	Vehicle Footprint Dispersion Ellipse
WoR	Window of Regard for hazard detection

Mathematical Symbols

$a, b, c, e; x, y, z; A, u, B$	plane fitting parameters
binSizes	vector defining the feature size bins
$\text{Cost}_{i,j}$	cost of each grid cell
d	distance to the horizon
d_2	surface distance that is visible
h	estimated altitude above mean surface
N	weighting factor between size and number of features
$\text{Path}_{\text{estimated}}$	the least squares estimate of the range sensor beam path on a smooth plane
$\text{Path}_{\text{actual}}$	the actual range sensor beam in three dimensions
$\text{pixels}_{\text{chopped}}$	pixels remaining in the traverse direction with horizon removed
$\text{pixels}_{\text{total}}$	pixels in the traverse direction of the full image
r	radius of planet
$\#_{i,j}^{\text{features}}$	vector of feature counts, binned by size, for each grid cell
$\#\text{GridCells}$	total number of grid cells in a given direction (either downrange or crosstrack)
$\#\text{LAPs}$	number of landing aim points desired per landing area
$\#\text{Pixels}$	number of pixels in the image in a given direction
$\#\text{Pixels}_{\text{GridCell}}$	number of pixels for a given side of the grid cell
α	FOV of the camera
γ	angle between the heel and center of the FOV
v	vehicle horizontal relative velocity
σ	standard deviation of the range precision noise
τ	time to aim point
θ	angle between nadir and the heel of the FOV

1 Introduction

To date, planetary exploration has occurred through stationary landers, rovers, and orbiters. Landers explore the region immediately within reach. Rovers explore locally, or within a “neighborhood”. Orbiters explore globally, but are only capable of remote observation.

This thesis describes mobility for a new type of vehicle: a hopper. A hopper explores regionally by operating as a sedentary lander in any given location, but with the capability of exploring several locations hundreds to thousands of meters apart by propulsively moving from one landing location to another.

Hoppers have been proposed as a possible form of planetary surface mobility since the days of the Apollo missions. The first instance of a “hop” occurred with the Surveyor 6 lunar lander (1) as an experiment to test the re-ignition of the Surveyor engines while on the lunar surface. The Surveyor 6 lander fired its vernier engines for 2.5 seconds after landing on the lunar surface. This was the first planetary “hop” that was performed, but this mission mode was not adapted for any future missions (2). Since then, there have been several theoretical concepts for mechanical and propulsive hoppers for planetary mobility. As a form of planetary surface mobility for astronauts, several mechanical hopper concepts were developed (3)(4)(5)(6), which were followed by a design for a propulsive hopper that could transport astronauts over greater distances (7)(8)(9)(10). The hopper concept was expanded to several studies done for Martian surface exploration (11)(12)(13)(14)(15)(16)(17). These propulsive hoppers were not prototyped, and ultimately rovers were used for both Lunar and Martian mobility systems. An upcoming proposed NASA mission, CHopper (Comet Hopper) (18) proposes to do multiple landings on a comet, giving merit to hopping on planetary bodies with low gravity and possibly the first planetary mission to employ hopping.

Recently, at MIT and Draper Laboratory, the Terrestrial Artificial Lunar And Reduced Gravity Simulator (TALARIS) project was started to develop a prototype of a hopping vehicle for development and demonstration of hopping technologies (19)(20)(21)(22)(23)(24). Under this project, several concepts have been explored for planetary hopper architectures, and extensive studies have been done to understand advanced concepts required for a prototype hopper system (25)(26)(27)(28)(29)(30)(31)(32)(33)(34).

To expand the research on hoppers further, this thesis describes hopper mission scenarios and provides an operational concept and methods to safely traverse from one landing location to another on a planetary body using hopping. This thesis develops the following complementary methods to safely guide a hopper to a safe landing location, enabling future missions by ensuring the survival of the hopper at landing:

- A method to do safe landing area selection at long ranges and shallow path angles, when the desired landing target is considerably downrange, or has just come into view over the horizon.
- A method to do more detailed hazard detection at short ranges, near the very end of the hopper traverse.

1.1 Motivation

Draper Laboratory and MIT have developed a terrestrial prototype hopper (TALARIS) to test methods for autonomous guidance, navigation, and control of a hopper (19). The TALARIS prototype uses guidance, navigation, and control techniques developed for lunar landing (35)(36)(37). While these techniques will work to demonstrate hopping as a viable form of planetary surface mobility, new approaches will need to be developed to address the diverse and unique set of mission possibilities that hoppers enable.

Several enabling hopper mission concepts have been discussed with local experts and published in the literature:

- Planetary stratification characterization (38)(39): hoppers can precisely traverse steep terrain such as cliffs or crater walls, exploring exposed regolith to study the history of a planetary body.
- Planetary magnetometry (40): hoppers enable long, straight, stable flight over a planetary surface, maintaining a constant altitude and attitude to take measurements of the magnetic field near the planet's surface.
- Site certification (41): hoppers can fly low over a desired science or future landing site providing a high-resolution survey for future missions.

Ultra-precise landings (41): hoppers can enable precision landing by performing a coarse landing and hopping to the desired final landing target.

Figure 1 shows some of the comparisons and capabilities afforded by hoppers. The Mars Exploration Rovers (42) have travelled tens of kilometers over the better part of a decade. Hoppers would be capable of covering this distance in several minutes. Rovers are not ideal for traversing hazardous terrain and are unable to scale cliffs, while hoppers are able to fly alongside steep surfaces and over hazardous terrain.

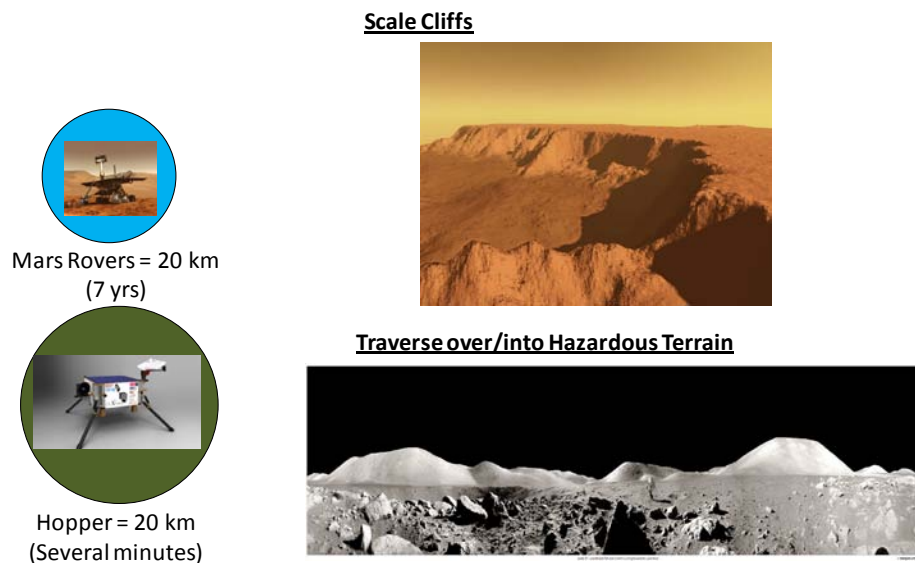


Figure 1 – Hopper Capabilities

Table 1 shows a comparison of planetary exploration systems and describes where hoppers fit into the gap left by sedentary landers, rovers, and orbiters.

Table 1 also outlines other exploration systems that have not been demonstrated in a relevant environment yet, but may benefit from similar site selection and mission operational concepts as those discussed in this thesis for hoppers.

Table 1 – Comparison of Planetary Exploration Systems

Method	Extent	Drawbacks
Sedentary Lander	<ul style="list-style-type: none"> •Simple architecture •In situ science and exploration 	<ul style="list-style-type: none"> •Single shot science & exploration •Single chance precision landing
Penetrators	<ul style="list-style-type: none"> •Simple architecture •In situ science and exploration •Simple deployment •Surface networks 	<ul style="list-style-type: none"> •Not demonstrated in relevant environment •Impact hardened avionics & payload
Rover	<ul style="list-style-type: none"> •Local explorer (rock-to-rock) •In situ science and exploration 	<ul style="list-style-type: none"> •Requires additional descent vehicle •Complicated egress •Terrain-limited
Hopper	<ul style="list-style-type: none"> •Same platform for landing and mobility •Precision through multiple hops •Rapid traverse •Regional explorer •Rough terrain exploration •In situ science and exploration •VTOL 	<ul style="list-style-type: none"> •Fuel-limited •Requires engine restart •Not demonstrated in relevant environment
Airship	<ul style="list-style-type: none"> •Long lifetime •In situ science and exploration •Regional explorer •Rough terrain exploration •VTOL 	<ul style="list-style-type: none"> •Not demonstrated in relevant environment •Atmopheric bodies only •Less rapid traverse/greater disturbances
Airplane	<ul style="list-style-type: none"> •Rapid traverse •In situ science and exploration •Regional explorer •Rough terrain exploration 	<ul style="list-style-type: none"> •Fuel-limited •Not demonstrated in relevant environment •Atmopheric bodies only •Runway for takeoff and landing
Orbiter	<ul style="list-style-type: none"> •Simple architecture •Global 	<ul style="list-style-type: none"> •Remote observations

Stationary landers (43) and penetrators (a form of hard landers) are relatively simple and allow initial exploration of a planetary body’s surface by studying the area of the planet that is in immediate proximity, or at least within “arm’s reach” of the lander. Landing autonomy and navigation for planetary surfaces has been demonstrated for lunar and Martian landings and is a current area of development under NASA’s Autonomous Landing and Hazard Avoidance Technology (ALHAT) program (44).

Rovers provide an initial level of mobility (45)(46) that allow neighborhood exploration within a vicinity of several kilometers. Orbiters provide global exploration of a planetary body, but these observations are remote, rather than being in-situ.. Navigation of these vehicles has been mainly performed manually between planetary rovers and operators from Earth, though low levels of automation have been demonstrated recently with the Mars Exploration Rovers (MER) (47).

Hoppers enable regional exploration capabilities by allowing the exploration platform to fly from one location to another. Other types of proposed explorers that could provide regional exploration, such as airships and airplanes, are also new methods of surface mobility that would benefit from the analysis and techniques performed in this thesis. Vehicles that traverse rapidly and travel above the planetary surface must make decisions quickly about where they are and where they need to go. These systems are also limited in what they can carry onboard as mass allocations are at a premium for flying spacecraft. This limits vehicle payloads for sensors and computational resources that can be carried onboard. These systems would benefit from techniques that still enable them to target and navigate, but with smaller, simpler sensors and algorithms that require less computational load.

Hopper mission scenarios have similar challenges to rover and lander missions for autonomous mission execution, but hoppers differ from planetary rovers (the standard method for providing planetary surface mobility) and landers in several key ways:

- Planetary rovers are not required to perform real-time site selection and navigation, because they have the ability to stop as necessary to plan and maneuver each step without the risk of flying into hazards or running out of fuel. Humans can also provide supervisory control between each maneuver. Hoppers are flying vehicles and must operate real-time, performing navigation, site selection, hazard detection, and hazard avoidance autonomously.
- Planetary rovers perform local, or neighborhood exploration. Hoppers are beneficial for long range, regional exploration.
- Planetary rovers travel at relatively low speeds. Hoppers are capable of traversing long distances in a relatively short time. As an analogy, this could be related to driving a car versus flying cross-country.
- Hopper approach angles to the planetary surface may be very shallow. The Apollo landers came in on relatively low trajectories from orbit, but hop trajectories (41)(48)(49) have a shorter horizon and may be flying a grazing trajectory over the surface. Methods are needed to address this type of flight scenario. The landing site of interest may be located at a very shallow view angle and distinct features may be hard to detect or may be masked by other features.
- For beacon/ground/science station emplacement (41)(50) missions, hoppers can be used to emplace or act as beacons, ground stations, or scientific stations. Hoppers can be emplaced as a beacon marking a desired landing site. Hoppers can provide a base of operation for remote locations or relays. Hoppers can emplace or act as science instruments, e.g. seismometry, telescope arrays, or weather stations. Such assets may need to be precisely placed into or on top of hazardous regions which may only be accessible by a flying vehicle.

Hopper vehicles enable several unique mission scenarios because they are able to fly from one location to another. Figure 2 shows some of the typical modes hoppers may experience. Hoppers, like conventional stationary landers, will land from orbital trajectories, but they will also land after doing a low altitude traverse. Hoppers also provide unique operational modes such as crater exploration and the ability to scale vertical terrain for science and exploration.

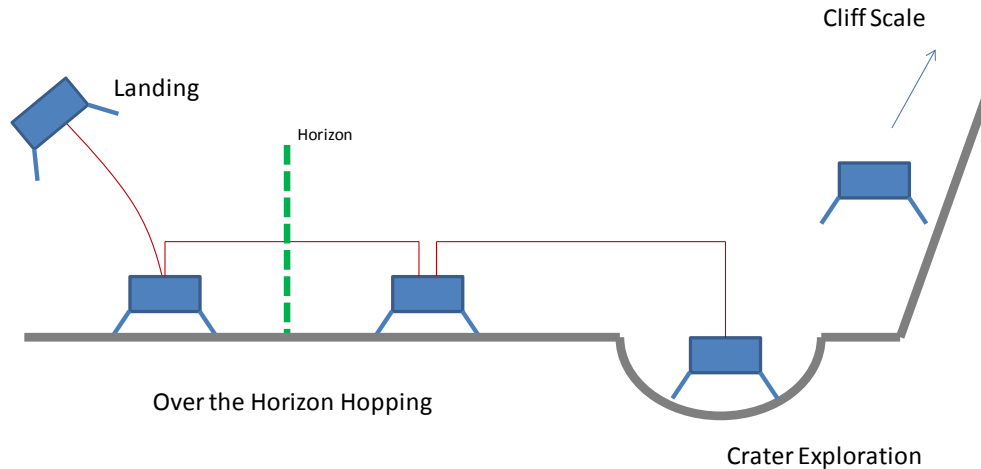


Figure 2 – Modes of operation for hopper missions.

Hopping allows a vehicle to fly over hazards, navigate steep surfaces, and rapidly relocate from one landing location to another. These vehicles are predicated on flying and being able to safely land at the end of the hop. An assessment of the current architectures available for safe landing and traverse were conducted as part of this thesis. The gaps identified through the survey were:

- Current hazard detection techniques are very precise, but require sensors that are large and heavy, and algorithms that require large amounts of computational power. These techniques work under any lighting conditions, but are limited at shallow path angles and long ranges. A new method is needed that can rapidly assess surface hazards, and work at shallow path angles and long ranges.
- A simple, short-range method is needed to assess the slope and roughness near the landing site that has low mass, low power consumption, and does not require high computational processing, but can still precisely detect hazards.
- Certain surface locations are dangerous to spacecraft because of the possible thermal or lighting conditions. A vehicle is needed that can quickly access a location, perform a task, and then relocate to a safe location.
- Highly sloped regions on planetary surfaces are hard to access, and an operational concept to explore these regions needs to be defined.

To help a hopper land safely, active and passive surface feature detection methods are developed in this thesis. Passive visual detection methods are inherently dependent on sun angle and surface reflection. Major et al. (51) describe expected lunar lighting conditions and effects on the Apollo astronauts. Brady and Paschall (52) describe the challenges of safe lunar landing for the Apollo astronauts. The ability to detect hazards based on cues, such as shadows, allowed the crew of Apollo 11 to divert from their initially targeted landing site, which turned out to be in a boulder field, and relocate to a safe landing site. Depending on the path angle of approach, the sun elevation, and the sun azimuth, shadows may or may not be present in the field of view during traverse. Figure 3 shows a diagram of the sun and view angles affecting the Apollo missions.

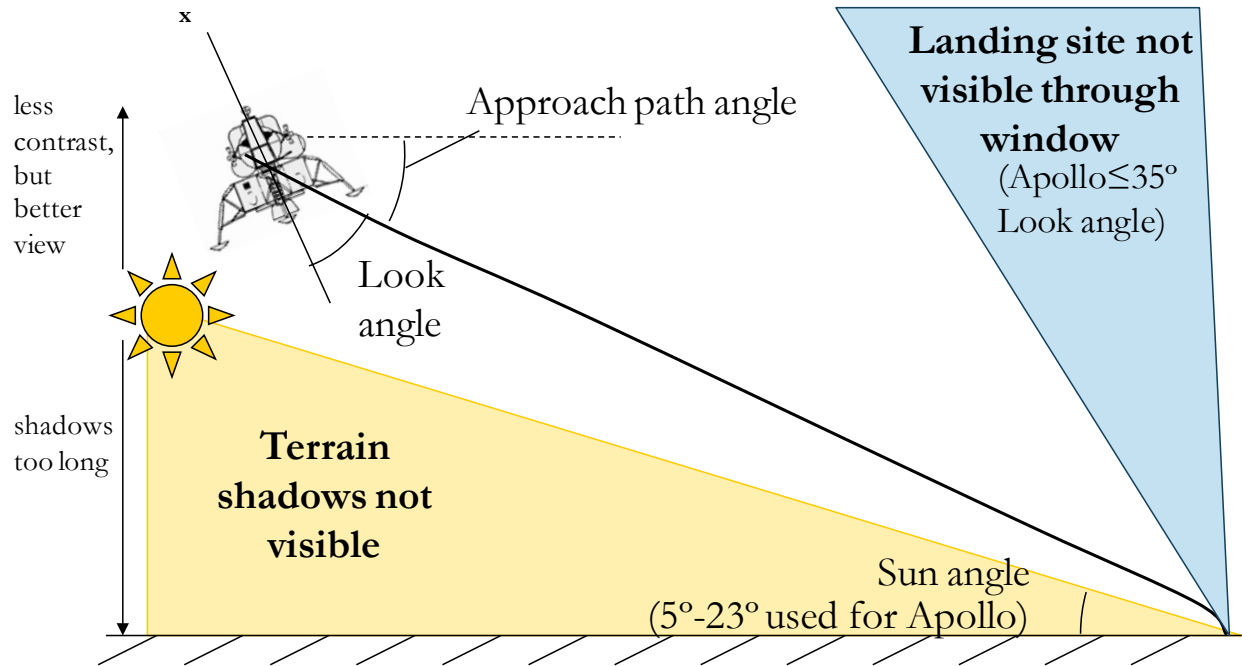


Figure 3 – Sun and View Elevation Angles affecting Apollo Missions

Active sensors are range limited, and require more power and mass (for larger optics) to operate at longer ranges. Sensors are under development that will provide precise measurements at longer ranges, but current short-range LIDARs can be used to adequately provide hazard detection near a landing site.

Though these techniques may be limited by lighting (for the passive feature-based hazard detection method), and range (for the active short-range LIDAR), combining the techniques in this thesis can provide a low mass, simple solution for safely traversing from one surface location to another.

1.2 Literature Review

A literature review was conducted to study the problem of navigating and site selection for planetary hoppers. Hopper site selection and navigation has similarities to planetary rovers and landers, but with some key differences.

Hoppers are a new class of robotic vehicle being developed for planetary surface mobility (41)(48). Hoppers use the same platform that lands on a planet's surface to provide mobility around that surface. The same sensors and actuators are used for landing and to propulsively "hop" from one surface location to another.

Once on the surface, hoppers fly unique trajectories: low altitude, rapid traverse, and grazing trajectories. Previous papers describe hopper trajectories, including the "hover hop" trajectory (37)(53)(49)(54). The hover hop trajectory maintains a fixed attitude and fixed altitude during traverse, providing a stable platform to perform exploration and scientific observations during flight. This type of trajectory also enables hazard detection at low viewing angles for landing points at sites near the horizon. Hoppers will have to constantly assess the terrain ahead to determine a feasible landing site. As

described in prior papers (41)(48)(55), hoppers will be able to traverse hundreds to thousands of meters in a single hop, and may not have any knowledge of the landing site characteristics before beginning the hop. Existing state-of-the-art technologies and methods include many techniques for detecting landing hazards and selecting landing aim points, using both passive and active methods (56)(57)(58)(59)(60)(61)(62)(63)(64)(65). These methods have been developed for landing from orbit, where a view of the landing site is provided from a top-down perspective and from a birds-eye view. Though they can be very precise, a downside of these techniques is that they place a significant computational burden on spacecraft avionics and computers by attempting direct detection of hazards through computationally costly algorithms.

Current research in precision landing and hazard detection and avoidance, done through NASA's Autonomous Landing and Hazard Avoidance Technology (ALHAT) project (44), uses sophisticated sensors to map and track features during the last 1-2 minutes of the descent profile (66). A dual-state navigation approach is taken, where inertial data is fused with surface-relative data to update the state of the vehicle during descent. This is an expansion on methods used during Apollo for landing (inertial instruments with humans as surface relative navigators) (52)(67) and Rendezvous and Proximity Operations (RPOP), e.g. shuttle docking with space station (spacecraft-to-spacecraft relative).

Precision landing systems use maps generated by scans from onboard sensors to correlate to a priori maps stored in memory using Terrain Relative Navigation, or TRN (68)(69)(70). TRN can pinpoint the location of a vehicle with respect to catalogued surface features to within the error of the map to the inertial frame (map-tie error). The Lunar Reconnaissance and Mars Reconnaissance Orbiters are creating detailed maps of the Moon and Mars that can be used for TRN. Traditionally, TRN has been used from an overhead view. These methods are applicable to hoppers for detection of terrain features, but have been mainly developed for landing-from-orbit applications. For hoppers, TRN can be done by looking horizontally, discerning surface features by looking tangent to the surface to correlate to an overhead view map. These techniques have been proposed for rover (71)(72)(73)(74) and terrestrial UAV navigation (75), but have yet to be demonstrated autonomously on a real-time platform. The vehicle limitations to carry the mass of the sensors and computing power required to perform real-time TRN are being alleviated as sensors and avionics are miniaturized to provide the resources needed to carry this capability aboard mass-constrained vehicles. Hoppers may also be able to fly over landing sites to create maps of the surface that can then be used to navigate for future hops. This technique uses more fuel, but may enable certain mission objectives by allowing for detailed mapping of a hazardous or unknown area of interest before entering it.

Adams et al (69) describe a system being developed for lunar TRN that uses two optical cameras. The two optical cameras view the surface of the moon and compare the images to rendered onboard maps that have shadows added to correlate with the time of day of the surface being imaged. This technique uses maps of the lunar surface, guidance trajectory data, and shadow information to precisely pinpoint the spacecraft during descent to the lunar surface. It requires onboard maps and views surface features at oblique angles, i.e. not from straight overhead.

Johnson (57)(68) describes methods for both hazard detection and terrain relative navigation. These methods are proposed for lunar landing platforms with the capability to carry and power large LIDARs and cameras to accurately assess the lunar surface and guide a lunar landing vehicle to the surface. The algorithms and methods for detecting and tracking features will be useful for hopper navigation, but need to be adapted to provide rapid updates and oblique viewing angles. Also, with their repeated takeoff, hover, and landing requirements, small hoppers are sensitive to onboard mass and so cannot afford massive, power-hungry navigation and hazard detection sensors.

Mars rovers use optical instruments to capture terrain images and ship this information back to Earth for rock identification and path planning. Rovers also have the benefit of non-time-critical site selection and navigation. Rovers take imagery, send it back to Earth for processing, and wait for commands before moving. Hoppers will not have this luxury as they will be thrusting continuously throughout their traverses and need to make site selection and navigation assessments in real-time. The Mars Exploration Rovers (MERs) demonstrated visual odometry as an experiment during traverse (47) and, although this technique is promising, it still requires significant onboard processing.

Cozman and Krotkov (72) (73) propose methods for rover navigation using the sun and surface features. A sun sensor is used to measure sun altitude and correlate it to the expected location of the sun in the sky based on latitude/longitude of the vehicle on the planet. An algorithm for pose estimation identifies mountain peaks and correlates them to a topography map to locate the rover on the surface. Though this algorithm seems very applicable for rover and hopper navigation, it requires human-in-the-loop operators to help select peaks and correlate with surface features. This technique is promising to help develop new ways to perform TRN from a “horizontal” perspective.

Volpe (76) also proposed using a sun sensor with an odometer to track rover progress over the Martian surface. Unfortunately, hoppers will not have accurate onboard odometers because they are not in contact with the surface. Hoppers may be able to track distance by a combination of integrating accelerometer data and optical tracking of surface features through optical flow techniques.

Dupuis (74) describes a method for using a LIDAR to create 3D images of the surface out ahead of a rover. This performs TRN from a side perspective, but automation of this process is not found in the literature. This process also requires significant computing and power to produce imagery. Rovers have the ability to pause and take stable imagery to make precise correlations. Hoppers will be in constant motion, traversing horizontally and jittering in attitude. Coarse horizontal TRN techniques may be applicable to hoppers, since they traverse over hazards and may require only gross hazard detection and avoidance until landing.

Methods for lander, rover, and UAV navigation are promising, but still have limitations for hoppers that need to be addressed. These methods can be used as benchmarks and expanded on to apply to hopper site selection and navigation.

Other proposed methods for planetary exploration include blimps (77) and airplanes (78). These forms of mobility will only work for planetary bodies with atmospheres. These vehicles are also new viable

forms of planetary surface mobility, and new methods of hazard detection and landing site selection developed in this thesis will be applicable to these other low-flying vehicles.

1.3 Thesis Objectives

The key questions of this research are:

- What types of missions will hoppers perform and how does a hopper traverse as part of these missions?
- How does a hopper traverse from its current location to a new landing site safely?

This thesis:

- describes various hopper mission scenarios and considerations for their mission designs
- creates an operational concept for safe landing for the traverse hop mission scenario
- develops a method that can be used to rapidly and safely detect landing areas at long ranges and low path angles
- develops a method to do fine detection of hazards once at the landing site

There are many techniques that are applicable from lander and rover navigation and site selection that can be used for hoppers. Since hoppers are fuel-limited, low-flying traverse vehicles, they can benefit from new methods to navigate and safely select landing sites. This thesis proposes to address these gaps by:

- Describing various hopper mission scenarios and the challenges associated with each of them.
- Developing a feature-based detection technique to rapidly assess relative landing safety. Current hazard detection techniques are very precise, but require sensors that are too large and heavy, and algorithms that require too much computational power for a small robotic hopper. These techniques work under any lighting conditions but are limited at shallow path angles. A new method is needed that can rapidly assess surface hazards and work at shallow path angles. The Size Density Method (SDM) described in this thesis enables rapid landing area selection during traverse. This technique is beneficial for small, mass-constrained vehicles, but is agnostic to vehicle size. Even though bigger vehicles may have the capacity to use better sensors, these methods will still be applicable.
- Developing a method to directly detect and assess the slope and roughness environment at a desired landing location: The Size Density Method proposed in this thesis is able to detect rock and crater hazards and provide alternate safe landing area suggestions based on that information but is light-limited and detects hazards coarsely. A complementary algorithm, Sparse Slope and Roughness (SSR), is developed utilizing active sensing techniques to detect hazards at the very end of the hop, right before landing. This method utilizes short range LIDARs and studies the ability to make accurate hazard detection through sparse sampling of surface features at short range during the final stages of traverse before a hopper lands.

1.4 Thesis Overview

Chapter 1 provided a background on previous work done on planetary landing and mobility and compares it to challenges unique to the hopper mission. Motivation is provided for why new methods are needed for hopper mission scenarios.

Chapter 2 reviews the past and current navigation architectures that have been used for planetary landing and traverse. A comparison is presented between traditional landers and newly developed concepts for hoppers. Techniques to navigate hoppers that can be leveraged from other work are described.

Chapter 3 discusses several hopper mission scenarios and provides operational concepts for them. This chapter describes the operational concepts for traverse site selection and hazard detection which have been developed in this thesis for landing area selection and safe landing aim point identification during a hopper traverse.

Chapter 4 presents the Size Density Method developed for narrowing down potential landing areas upon approach from long distances and shallow path angles. This method uses passive optical imagery to rapidly and statistically determine safe landing area locations. It provides information well uprange of the final landing target, allowing early decisions to be made about where to direct the hopper to improve the probability that a safe landing aim point can be found near the end of the hop. The analysis in Chapter 4 explores the performance of the method for varying lighting and viewing conditions.

Chapter 5 presents a method to detect slope and roughness at short range using a LIDAR to make sparse measurements of the surface and detect a safe landing aim point. It complements the Size Density Method by providing more precise hazard detection once at a landing area, near the end of a hop.

Together, the Size Density Method and the Sparse Slope and Roughness method increase the likelihood that a safe landing aim point can be found for the hopper at the end of a traverse. Chapter 5 presents analysis of the passive and active hazard detection methods working together to provide a complete hazard detection solution from the beginning of a hop to the end.

Chapter 6 summarizes the work in this thesis and presents ideas for future work.

2 Current Methods for Landing and Traverse

This chapter will describe current methods of landing and traverse used by space vehicles that are similar to hoppers: landers and rovers. It also discusses how the navigation and site selection architectures for those vehicles can be leveraged and updated to provide navigation and site selection for hopper missions.

2.1 Hoppers as an Extension of Landers

Hoppers can be described as landers that are allowed to perform multiple landings once at the surface of a planetary body. Historically, landers have been designed to land once, and their navigation and site selection systems were designed for descent from orbit. Hoppers provide new challenges because they also need to ascend and traverse across the surface.

Since hoppers move propulsively across the surface repeatedly, they require more fuel for the same dry mass than a single lander vehicle. This puts mass and volume at a premium, and any reduction in the infrastructure needed for sensing adds mission capability to the hopper by freeing up mass that can be used for fuel.

2.1.1 Landing site approach trajectories

Lander trajectories descend from high altitudes and have both large vertical and horizontal relative velocities that need to be arrested to safely touch down on the surface of a planetary body. Precision is realized by a combination of pre-flight surveying (from orbital mapping), onboard sensor systems, and proper actuation control authority (35)(36).

A typical lander trajectory, modeled after Apollo landings and developed for possible modern missions to the Moon, is shown in Figure 4 (79).

This approach gives anywhere from 30 to 120 seconds of view time of the landing site and 15 to 90 degree view angles into the landing site (80). Horizontal relative velocities range from 100 m/s at the start of the approach phase to 0.1 m/s upon the start of the terminal descent phase (81).

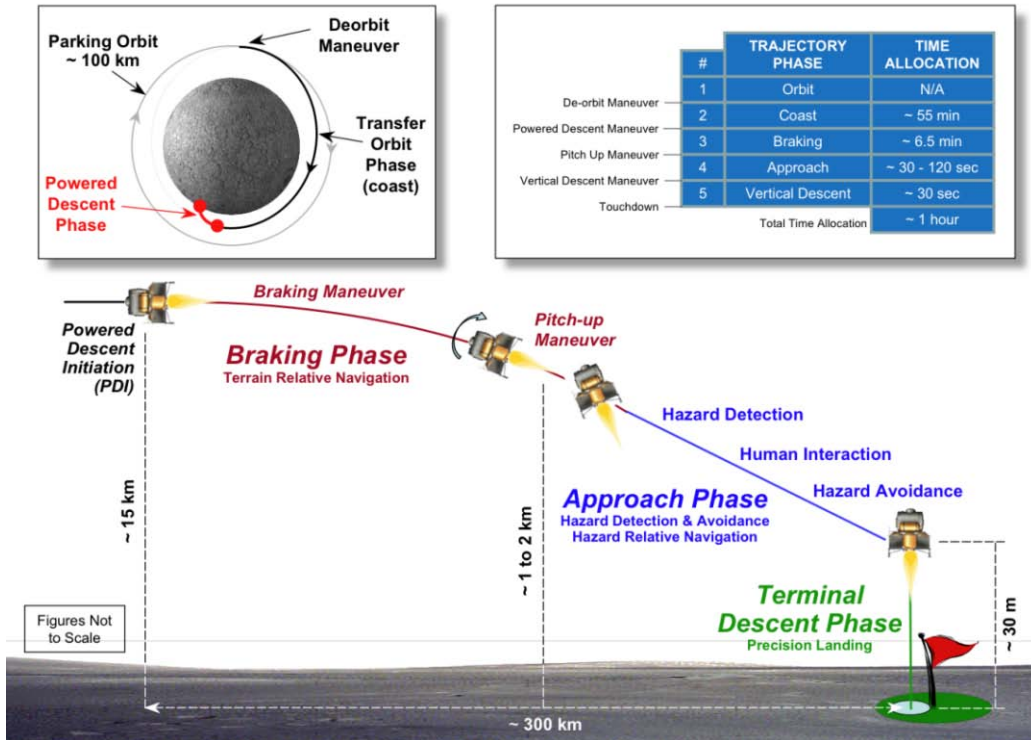


Figure 4 – Lunar Landing Trajectory

Figure 5 shows hopper trajectories of interest: a 500 meter hover-hop (short, within the horizon at takeoff) and a 5000 meter hover-hop (long, over the horizon). These two trajectories were selected from the mission goals for the Google Lunar X-Prize (GLXP) minimum distance and extended mission (82). The hover-hop mission is also beneficial for science and exploration missions by providing a stable attitude platform for sensors (41)(48).

The typical times, ranges/altitudes, and delta-V required for both hops is presented in the table in Figure 5 (49). The numbers reported in Figure 5, chosen trajectories from Middleton 2010 (49), approximate to the minimum delta-V trajectories presented for the 500 and 5000 meter hops. The nominal traverse acceleration used was 0.7 of the initial Thrust to Weight (T/W) ratio, and the vertical max T/W was 1.2 of the initial system T/W. Altitudes for 500 meter hops were capped at 5 meters, and for 5000 meter hops were capped at 20 meters. For these trajectories, 10 and 30 second traverse burn times were used respectively.

For hover-hop trajectories (20)(27)(49), typical altitudes for traverse are 2 to 20 meters (49)(54) above the surface, to conserve the fuel needed for ascent and descent. These create very shallow approach path angles to the landing site. The landing sites also may only come into view with several seconds remaining before landing. Horizontal relative velocities upon approach to a landing site may be on the order of 1, 10, or even 100 meters/sec (49). Consequently, the duration of the traverse phase for a hopper is comparable to that of the approach phase during landing, but is at a much shallower angle to the landing site. This limits direct views of the site and requires a technique to be able to do safe site selection with less available time and at lower angles.

#	TRAJECTORY ACTIVITY (Containing 0.7 traverse T/W and 1.3 vertical T/W)	TIME ALLOCATION (sec) (Short vs Long Hop)	RANGE ALLOCATION Short Hop (meters)	RANGE ALLOCATION Long Hop (meters)	DeltaV (m/s) (Short vs Long Hop)
1	Ascend	~10-20	5 (altitude)	20 (altitude)	~10-20
2	Accelerate	10-30	~50	~500	~10-50
3	Coast	~50-180	~400	~4000	~60-160
4	Brake	10-30	~50	~500	~10-50
5	Descend	~10-20 sec	5 (altitude)	20 (altitude)	~10-20
Total Allocations		~90-280			~100-250

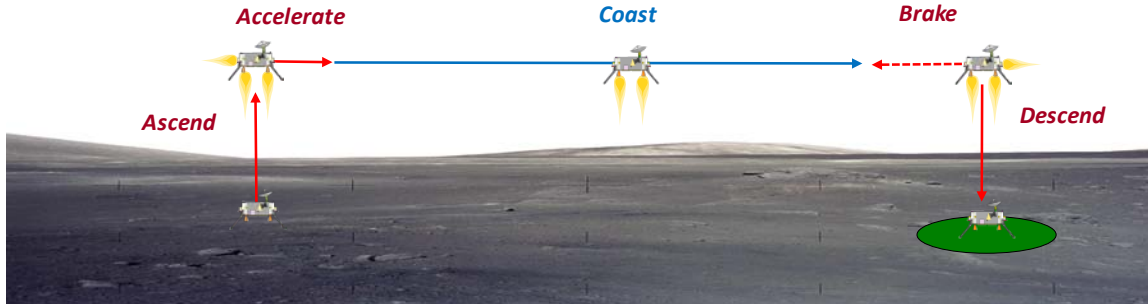


Figure 5 – Hop Trajectories: Phases, Times, Ranges, and Delta-Vs

2.1.2 Mass allocations and vehicle actuators

Hoppers are landers with additional fuel onboard to provide mobility across the surface of a planetary body. The additional fuel mass needed for mobility puts a premium on sensor and payload mass allocations for a hopper. Therefore sensors that can be used for navigation and site selection for landing and traverse need to be smaller, efficient, and benefit from serving multiple functions within the same sensor.

The vehicle actuators on a lander may only be ignited once and require less dynamic range than that of a hopper. For a hopper mission, the actuators must be able to reignite, as well as provide enough thrust for the ascent portion of the hop (T/W ratio >1 prior to ascent).

Hopper actuators may also be limited on the spacecraft. The Next Giant Leap GLXP team developed a hopper configuration to minimize the number of thrusters for a fixed attitude/fixed altitude hopper to provide adequate vertical and traverse control authority, shown in Figure 6 (33). This configuration allows the hopper to maintain a fixed altitude and fixed attitude during a hop (hover-hop), which is beneficial for science and exploration missions (48).

A typical lander may have up to four additional fixed thrusters (two in the +Y axis and two in the -Y axis) to support lateral control during descent.

The configuration shown in Figure 6 allows enough control authority to maintain vertical (X direction), pitch, and yaw control. Traverse occurs in the +Z direction and directional control is provided by “steering” or “rolling” the hopper about its vertical axis towards the intended target. This configuration creates controllability in the vehicle and reduces mass, but also enables the use of simple optical

cameras and range sensors to provide landing and traverse navigation and site selection by creating a stable platform for these sensors to operate on during traverse.

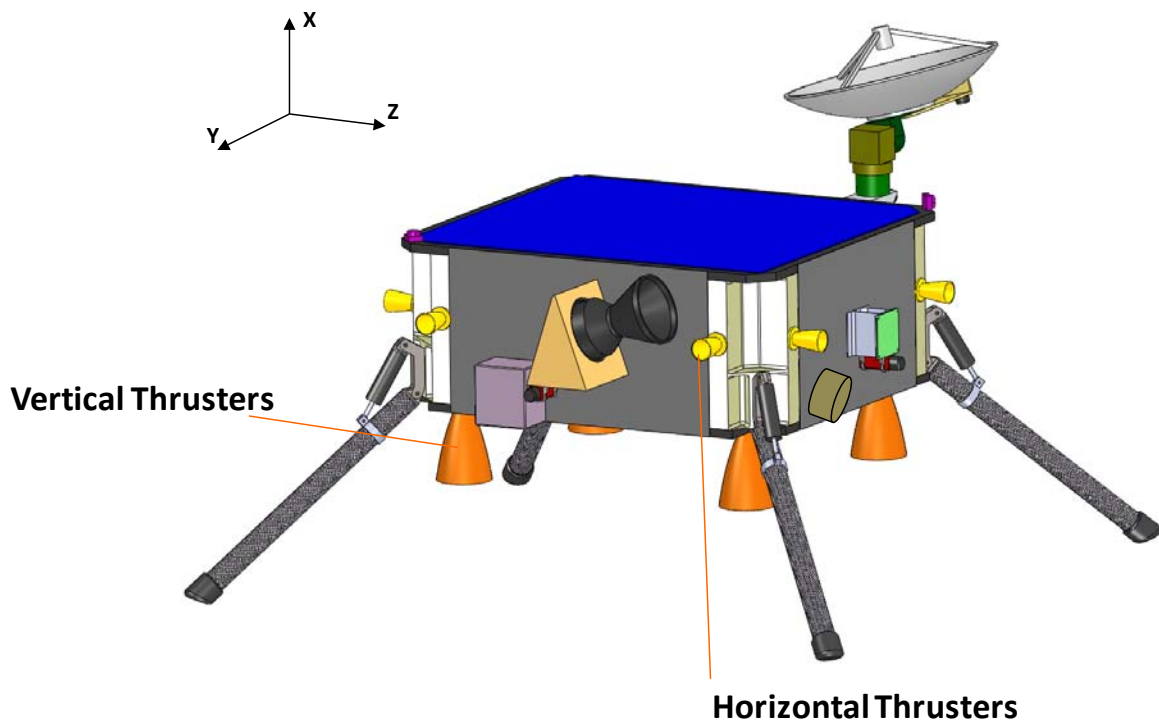


Figure 6 – Hopper Actuator Configuration

2.2 Techniques leveraged from Landers and Rovers

This section describes techniques used in previous landing and rover missions. Some techniques used during past missions for landing and traverse navigation and site selection architectures can be applied for hopping. A historical context of previous and current missions is given, and then applied to the hopper problem. The following section will describe gaps and pitfalls with using only past and current architectures and presents several new methods developed in this thesis to further enhance hopper capability by providing the navigation and site selection capability in a smaller, less computationally expensive package.

2.2.1 Navigation and Site Selection Architectures Past and Current

Table 2 shows past technologies and current technologies under development. Possible navigation architectures include inertial measurement units, surface relative position and velocity sensors, ranging sensors, and star sensors. Though some of these sensors are high performing, many of them are too large, heavy, or require too much power to be used on a hopper vehicle.

Table 2 – Navigation and Hazard Detection Architectures Past and Current

Mission Type	Mission Example	Mission Date	Methods/Sensors used for Navigation and Hazard Detection
Lunar Robotic Impactor	Ranger (USA)(83)	1961 - 1965	Gyro Triad Sun Sensors Earth Sensor Radar Altimeter
	Hiten (Japan)(84)	1990 - 1993	Sun Sensors Star Scanner Horizon Sensor Accelerometer Triad
	SMART-1 (ESA)(85)	2003 - 2006	Optical Navigation Star Mapping
	Chandrayaan-1 (India)(86)	2008	Star Sensors Gyros
Lunar Robotic Lander	Luna (USSR)(87)	1958 - 1976	Gyros Radar
	Surveyor (USA)(1)(88)	1966 - 1968	Gyro Triad Sun Sensor Star Tracker Radar Altimeter Radar Doppler Velocimeter
Lunar Robotic Rover	Luna (USSR)(89)	1970 - 1973	Optical Cameras w/ Human Operator
Lunar Human Landing	Apollo (USA)(52)	1969 - 1972	IMU Sextant (for attitude updates) Radar Altimeter Human Eyes (Terrain Relative Navigation and Site Selection) Ground Contact Sensor
	ALHAT (USA)(44)(66)	2006 - 2012	IMU Star Camera Laser Altimeter Laser Doppler Velocimeter Optical or Flash LIDAR Terrain Relative Navigation Flash LIDAR Hazard Detection and Avoidance

Martian Robotic Landing	Pathfinder (USA)(90)	1997	Star Scanner Sun Sensors DSN update before entry Radar altimeter
	MER (USA)(42)	2003 - 2004	Descent Imager IMU Radar Altimeter Star scanner Sun sensor
	Phoenix (USA)(91)	2008	IMU Doppler Radar Altimeter/Velocimeter
	MSL (USA)(92)	2012	IMU Doppler Radar Altimeter/Velocimeter Star scanner Sun sensor
Martian Robotic Roving	Sojourner (USA)(93)	1997	Optical Cameras w/ Human Operator Tilt Sensors Structured light hazard sensor
	MER (USA)(42)	2004 - ?	IMU Optical Stereo Cameras Human Operator or Autonomous Visual Odometry Autonomous Hazard detection and Avoidance
	MSL (USA)(92)	2012 - ?	IMU Optical Stereo Cameras Human Operator or Autonomous Visual Odometry Autonomous Hazard detection and Avoidance

Beginning with early lunar impactor, lander, and rover heritage, the basic suite of sensors consisted of inertial instruments, course attitude sensors (such as sun sensors), and radar for landing altimetry and velocimetry. This basic suite of sensors, coupled with Deep Space Network (DSN) updates from Earth, provided the functionality to update the inertial solution of the lander during the braking and approach phases to the Moon (83).

During the early days of robotic lunar missions, the Soviet Union also had several successful rover missions (89). These first planetary rovers traversed by sending optical camera imagery back to Earth, where human operators would command small movements, wait for new imagery updates, and then continue driving the rover. Though this technique works well between Earth and the Moon, where communication delay times are low (1-2 seconds), it poses problems for exploration on other planets. These types of latencies would also greatly affect hoppers. Since hoppers are flying vehicles, tight closed-loop control of the system is required to keep the system stably flying. Even short delays could cause unrecoverable instabilities. If operators back at Earth were to teleoperate them, hoppers would be required to at least be inertially stabilized, but in this case manual control and delays would also impose fuel penalties that are undesirable.

The Apollo program (52)(80) employed human eyes and cognitive abilities to perform terrain relative navigation and hazard detection for the human lunar landings. Terrain relative navigation using optical crater matching was done with a stopwatch and stored onboard imagery correlated against views out of the lander's window. Astronauts correlated known groups of craters to the expected times that they came into view over the horizon. For planetary bodies that have a priori maps, such as the Moon and Mars, these techniques can be used to maintain a global heading and position by correlating these priori maps of craters with crater triangulation taken during flight (68). Current techniques are being developed to provide precise terrain relative updates using optical imagery or flash LIDARS, with sophisticated algorithms to perform the terrain correlation (freeing the humans to perform other tasks, or enabling TRN for robotic vehicles).

During landing, the astronauts would use their eyes to locate hazards such as craters and boulders. However, human eyes and passive optical techniques have problems detecting slope, especially on the Moon where the surface's brightness is intensified when the sun angle approaches the viewing angle (94). A single range sensor can give a decent approximation of surface curvature near landing (assuming continuity of surface). Multiple range sensors can provide a relatively strong idea of the slope beneath the hopper for landing (95) and will be discussed in this thesis.

Martian landers and rovers began using more sophisticated onboard sensors and algorithms as onboard processing had improved since the early lunar missions. The Martian landers employed optical descent imagery to maintain low relative horizontal velocities and high-resolution imagery for rover traverse navigation (96)(42). The detailed imagery was used to detect features and correlate the descent overhead imagery with the features contained in the rover cameras' fields of view. Mainly, human operators used this imagery to help steer the rovers once they had landed, but the MERs also employed visual odometry techniques to track features and provide surface relative position and velocity updates for long range autonomous roving over benign terrain and slip detection in rough terrain.

The ALHAT project is providing the most state-of-the-art research for descent and landing navigation and site selection architectures (44). ALHAT is developing a new set of sensors to further enable precise landing for the Moon and Mars. This system employs several technologies that are useful for consideration in hopper missions as well. NASA's Flight Opportunities Program is providing testbeds for demonstration of these technologies (32).

Table 2 lists the ALHAT suite of sensors under development, and the list is repeated below with more detail:

- Inertial Measurement Unit (IMU): consists of triads of accelerometers and gyros to detect the accelerations and attitude rates of the vehicle. These sensors drift without any external updates, degrading accuracy over time.
- Star Camera: provides attitude updates when properly pointed to dark sky. This helps give an absolute attitude reference frame.
- Laser Altimeter: provides range measurement to the surface (97) and can be used for both surface relative attitude, as well as basic terrain relative navigation.

- Laser Doppler Velocimeter: provides surface relative velocity updates (97)(98)(99)(100)(101)(102)(103).
- Optical or Flash LIDAR Terrain Relative Navigation (TRN): provides global position updates by correlating onboard stored imagery with sensor data (68)(97)(104).
- Flash LIDAR Hazard Detection and Avoidance: creates 2.5-dimensional topography maps of the surface that can be processed to detect hazards and select safe landing aim points (57)(97).

Table 3 shows how the different sensors can be used to provide measurements to aid in navigation of a landing or hopping vehicle.

Table 3 – Sensors to Measurements

	IMU	Star Camera	Laser Altimeter	Doppler Velocimeter	Optical Camera	Flash LIDAR
Inertial Accelerations	X					
Inertial Attitude Rates	X					
Inertial Attitude		X				
Surface Relative Position			X			X
Surface Relative Velocity				X	X	
Surface Relative Attitude (tip/tilt)				X	X	X
Hazard Detection					X	X
Surface-to-Inertial Updates via Correlated Terrain Relative Navigation			X		X	X

2.2.2 Limitations for Planetary Hoppers with current sensor systems

Planetary hoppers have mass, power, and computational bandwidth limitations. Active ranging sensors, such as flash LIDARs, give high precision, but are currently too massive, and require too much power and too many computational resources for hopper missions. Though these sensors provide the ability to perform navigation and hazard detection under any lighting condition, they are limited in hazard detection at shallow path angles.

For the Google Lunar X-Prize (82), a hopper vehicle was designed to address the mission needs of landing on the surface and traversing at least 500 meters while taking surface imagery. This was one of the first comprehensive designs for a hopper mission (41)(48). For the lunar landing portion of the mission, the lander/hopper would need to provide 2 km/s of delta-V (81). Delta-V costs for hopper missions as a function of delta-V are given by Middleton et al (49)(30). Figure 5 shows the typical values for hop delta-Vs. The delta-V, fuel Isp, and the dry mass of the vehicle can be used to compute the amount of fuel needed for each type of hop. Each kilogram of mass required for sensing corresponds to additional mass on the vehicle, trickles through the design of the structure and ultimately the amount of fuel needed for each hop.

Current technologies being developed under the ALHAT program for Flash LIDARs weigh in the neighborhood of tens-of-kilograms (97). The techniques described in this thesis use an optical camera and short-range LIDAR. This thesis describes a method for hazard detection for landing and traversing

vehicles using a sensor payload that can be an order of magnitude less in mass than the current systems that are being developed.

2.2.3 Possible Navigation and Site selection Architecture leveraging Past and Current Sensor Configurations

Employing the architectures seen in previous landing and traversing missions (Table 2), a possible system could consist of (Figure 7):

- IMU (not pictured) to provide inertial accelerations and angular rates.
- A short Range Altimeter to provide hazard detection close to the landing site.
- A velocimeter to provide both surface relative Doppler velocity and range measurements in the $-X$ direction to be used during terminal descent and traverse maneuvers. This sensor would provide updates to horizontal relative velocity and range to the surface (97).
- Optical cameras: one in the $-Z$ direction during the braking phase to perform Terrain Relative Navigation, and two others to be used during hops. These other two cameras (in the $+Z$ and $-X$ direction) can be used to provide position and attitude updates during traverse. This sensor can also be used for site selection.
- A star camera to initialize the inertial attitude of the vehicle if a proper view of dark sky is provided.
- A sun sensor as another coarse attitude update.

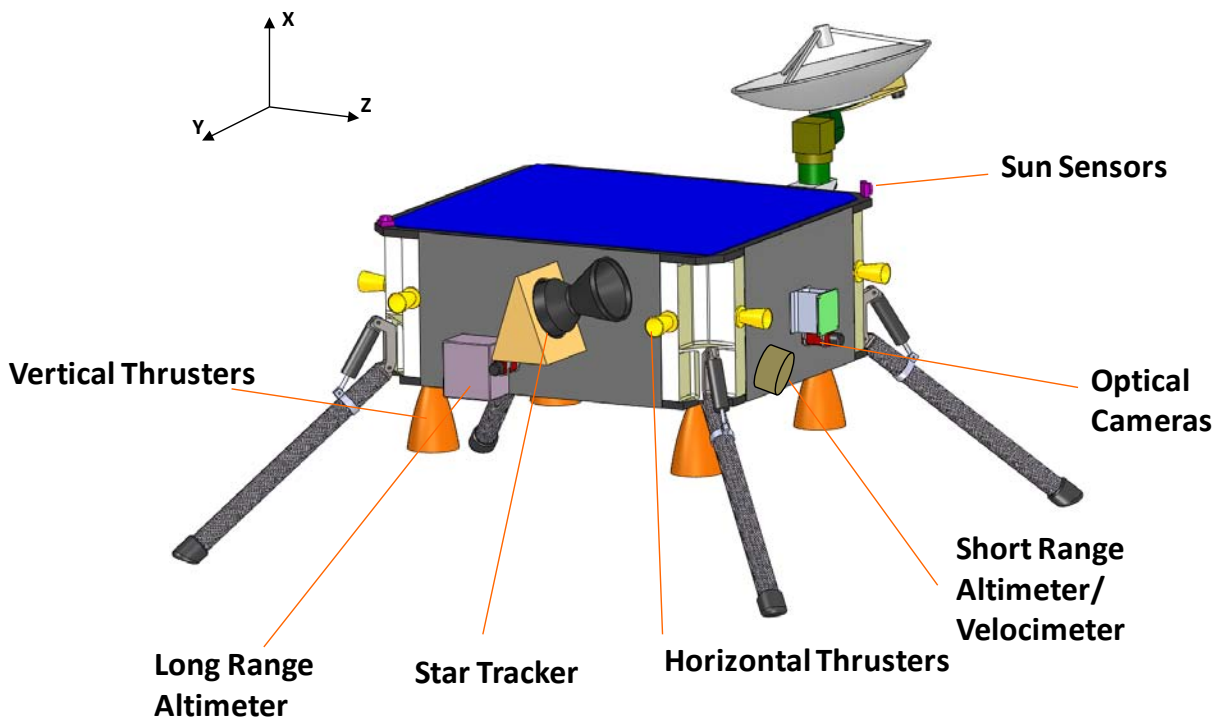


Figure 7 – Hopper Architecture including Navigation Sensors (not-pictured: IMU)

This system allows the vehicle to have inertial (IMU and Star Camera) updates during initial descent to a planet and initialize the vehicle prior to any hops. Once a hop begins, the range sensors and optical cameras that are viewing the surface can be used to provide surface relative navigation and site selection updates. Figure 8 shows a diagram of how the different sensors can be used to aid in autonomous guidance, navigation, and control of a hopper vehicle while also enabling the autonomous capabilities of site selection and hazard detection.

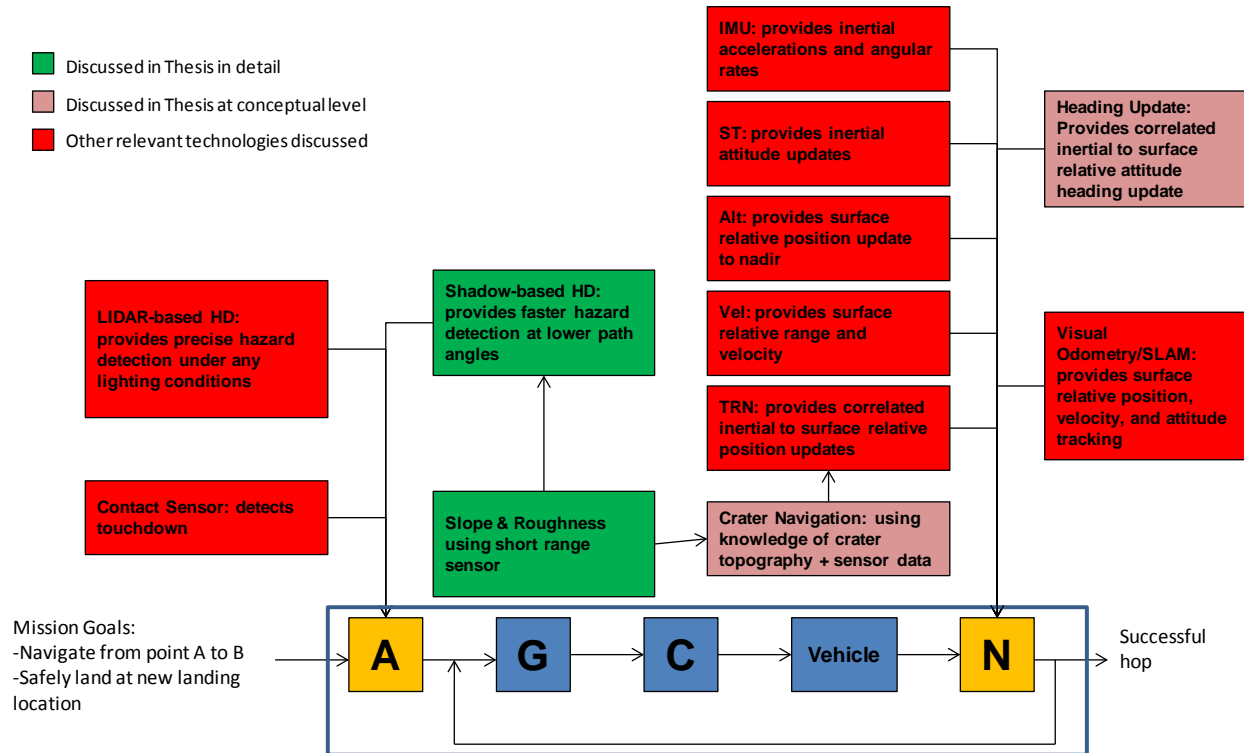


Figure 8 – Autonomy, Guidance, Navigation, and Control (AGNC) architecture for hoppers. The sensors outlined in red boxes refer to the ALHAT Sensor Suite. The sensors outlined in green boxes refer to the sensor suite proposed in this thesis for small hopping vehicles.

This thesis will utilize pieces of this current architecture to provide inertial and surface relative position and attitude updates, as well as information for safe site selection. Several methods are described that will help target safe landing sites, enable rapid traverses, and enable crater exploration for hopping vehicles beyond current available architectures. The techniques developed in this thesis use simple architectures and fast algorithms to enable site selection and hazard detection for hopper trajectories.

Current methods used and being developed for hazard detection either deduce structure from optical imagery, through stereo imaging of hazards, or by determining hazard structures from shadows. Some techniques use active sensing to directly measure range and develop digital elevation maps that can be used to process surface features and determine which features are hazardous. These techniques are direct and accurate, but require significant computational resources.

To meet the technology requirements for a traversing hopper vehicle, this thesis poses a method for rapid site selection for landing sites that come into view relatively quickly at shallow path angles. This

thesis develops techniques that use forward-looking imagery using passive optical cameras to perform autonomous landing area selection. Landing area selection is performed statistically depending on numbers and sizes of hazards, instead of directly imaging hazards, which allows more area to be covered, much faster, at lower path angles, and at longer ranges.

Hoppers also uniquely enable missions exploring steep surfaces, such as the interior of craters or the regolith along a cliff. This thesis describes operational concepts to carry out these specialized missions. Hoppers can thus land, hop next to, hop into, explore, and hop out of craters. Hoppers can also explore inside a crater based upon the known general morphology of craters.

Finally, this thesis also discusses techniques for detecting slope using simple short-range LIDAR, for crater and steep slope navigation, as well as detection of slope and roughness out ahead of the hopper during the final stages of the hop, prior to landing.

3 Hopper Mission Scenarios

Figure 2 shows several mission modes available to hoppers. These modes include landing, traversing over flat land, traversing into craters, and scaling steep slopes. Hoppers are unique: they are flying vehicles and are able to go to places other vehicles cannot easily go because of their ability to rapidly traverse over hazardous landscapes. This enables several unique mission scenarios for hoppers. However, hoppers are mass limited, putting a premium on mass used for sensing and propellant. Mission scenarios that use the strengths of hopper modes are outlined in this chapter.

The first mode of a hopper is landing from orbit. This problem has been studied extensively and new methods are being developed to address landing safely and precisely from orbit (44)(52). Planetary landings have been performed on the Moon, Mars, Titan, and smaller bodies (asteroids and comets). This thesis focuses on the hopper's modes once it has landed on the surface.

Once the hopper is on the surface, it can determine its planetary surface location and use that to aid it in planning for a hop.

There are many mission scenarios involving a traverse from a single location to a new location on the planetary surface. Foremost in enabling safe hopping, a method is needed to determine safe locations upon approach to the landing area. Once near a landing area, detailed hazard detection of the slope and roughness of the landing aim points within the landing area can be evaluated to determine a safe location for a hopper to land on without tipping over or being crippled by impacting a rock or crater. The main contributions of this thesis are methods for providing safe landing area detection. These methods will be discussed in further chapters.

The traverse hop can be used to precisely place the hopper globally, perform fixed altitude/fixed attitude science missions, and/or fly over a sight of interest for exploration and close inspection of the slopes and hazards in that area.

Hoppers uniquely enable the exploration of steep surfaces, such as cliff faces and the interiors of craters, which may be of great interest for science exploration. Being able to traverse a cliff in close proximity for sensor measurements while maintaining a safe distance enables stratigraphic analysis of exposed planetary regolith that may reveal the history of the planet over different eras. Craters may contain exposed regolith or water ice in permanently shadowed areas. The ability of hoppers to fly into, explore, and fly back out of craters is a key enabler for exploring these regions.

3.1 Traverse Hop Scenarios

The traverse hop can be used to relocate the hopper from one location to a new location on the planetary body. This enables exploration missions that require precise global placement or a stable platform for scientific instruments that scan the surface for scientific exploration or potential future landing sites.

As described in Chapter 2, the hopper can use inertial sensors (IMU and Star Camera) during the main part of the traverse to maintain global heading and a fixed attitude/fixed altitude profile (which is conducive to the best use of surface relative science and navigation sensors).

3.1.1 Operational Concept for Hopper Traverse Landing Area Selection and Hazard Detection

To enable safe hopping from one location to another, methods are needed to assess sites at the intended Landing Area (LA) and then perform precise hazard detection for safe landing. An operational concept for safe landing area selection and precise hazard detection is illustrated in Figure 9. The method described in this thesis incorporates two stages of hazard detection:

- 1) Long range, gross hazard detection to improve the likelihood of directing the vehicle to an area that is likely to have a safe landing aim point.
- 2) Short range, precise hazard detection to find the final landing aim point (LAP) during the final stage of the hop.

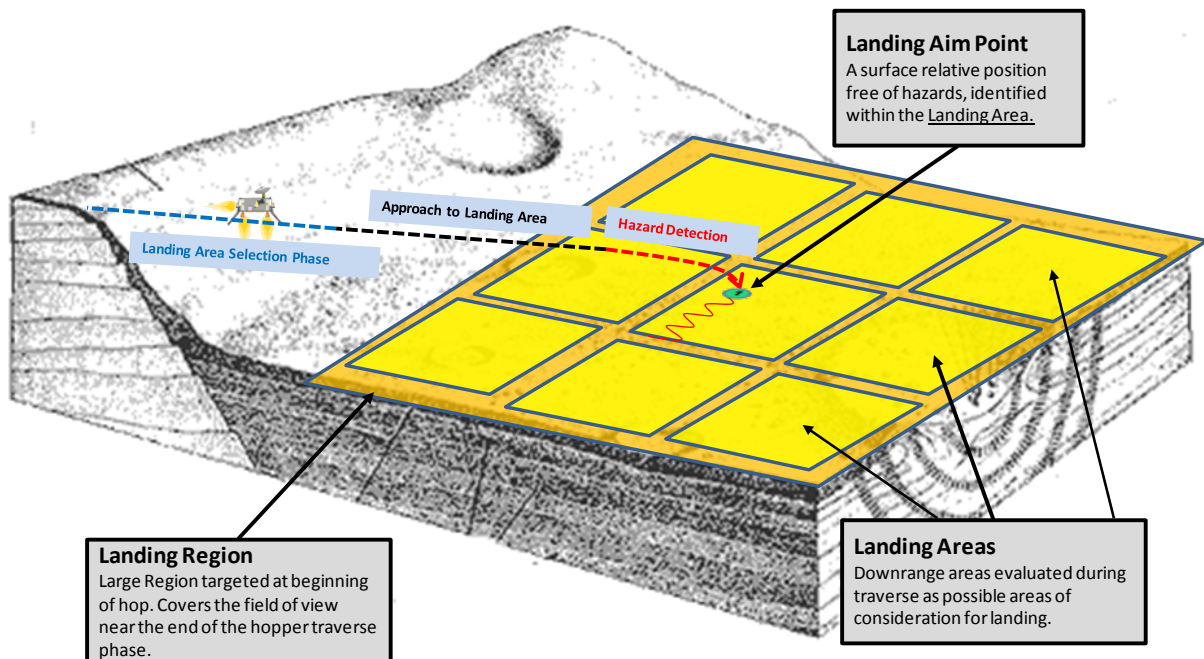


Figure 9 – Landing Area Selection and Hazard Detection Operational Concept Illustration¹

As the vehicle approaches the Landing Region (LR) at the end of a traverse, landing area selection can begin well uprange of the final intended landing location. A landing region is a large area near the intended landing location that the vehicle is approaching during the hop. Landing areas are located within the landing region and are sized based on the intentions and risk tolerance of mission planners. The larger the landing area is, the less precise the landing may be, but the higher probability that the hopper will ultimately land safely. Within a landing area, a landing aim point is a location the size of the lander footprint which is safe to set the vehicle down upon. Being able to identify a safe landing area at low path angles and at long ranges is a new method that is described in this thesis, called the Size Density Method. The method uses feature size and number within landing areas to assess the relative

¹ Adapted from Autonomous Landing and Hazard Avoidance Technology Project Operational Concept (141)

safety of one landing area to another. This redirects the hopper from long range as it approaches the landing area and directs it towards a landing area that would give it the best chance of landing safely. This is a gross hazard detection method intended to improve the likelihood of a safe landing by increasing the probability of finding a safe landing aim point within the landing area.

Without the Size Density Method, or another type of gross landing area selection, the likelihood that the vehicle may reach the intended landing location and find itself in a highly hazardous area with no safe landing aim points is increased. At this point, if all that is used is a technique to precisely determine landing aim point safety, the hopper may find itself in a location far from any safe landing aim points. Fuel will be expended for the hopper to continue downrange or cross range until it determines a safe landing location. This is similar to what happened during the Apollo 11 mission.

However, using bright features and shadows does not give a precise detection of slope and roughness at the actual landing site. To deal with this final stage of landing site selection, this thesis also describes a method using an active short-range LIDAR to interrogate the surface and estimate local surface slope and roughness more precisely.

Combining landing area selection from afar, using the Size Density Method, with slope and roughness detection near the end of the hopper traverse provides a strong operational concept for safely delivering the hopper to a new landing location. These methods also use relatively simple sensors that reduce costs for fuel and enable a longer mission life.

Chapter 4 describes the Size Density Method and analyzes its ability to select landing areas that improve the probability of landing safely. Chapter 5 describes and analyzes a short-range LIDAR-based method for direct surface characterization that can be used to find a safe landing aim point (within the chosen landing area).

3.1.2 Ultra-Precision Landings

Hoppers can provide global precision placement through multiple landings. Precision landing from orbit requires a small landing ellipse, with only one chance to land at the desired location. Landing precisely directly from orbit requires high performing sensors and actuators to provide the knowledge and control authority to hit the desired location. Hoppers, on the other hand, can afford to initially land coarsely using lower performing sensors and techniques and with actuators that have less control authority. The subsequent ability to do multiple landings enables a hopper to traverse to the desired global landing location and refine global precision through multiple hops. Using orbital reconnaissance for mapped planetary bodies (such as the Moon and Mars) improves global precision from hop to hop by correlating the hopper location with identified surface features throughout each traverse. Figure 10 shows a representation of precision landing from orbit versus landing and hopping to the desired landing location (55).

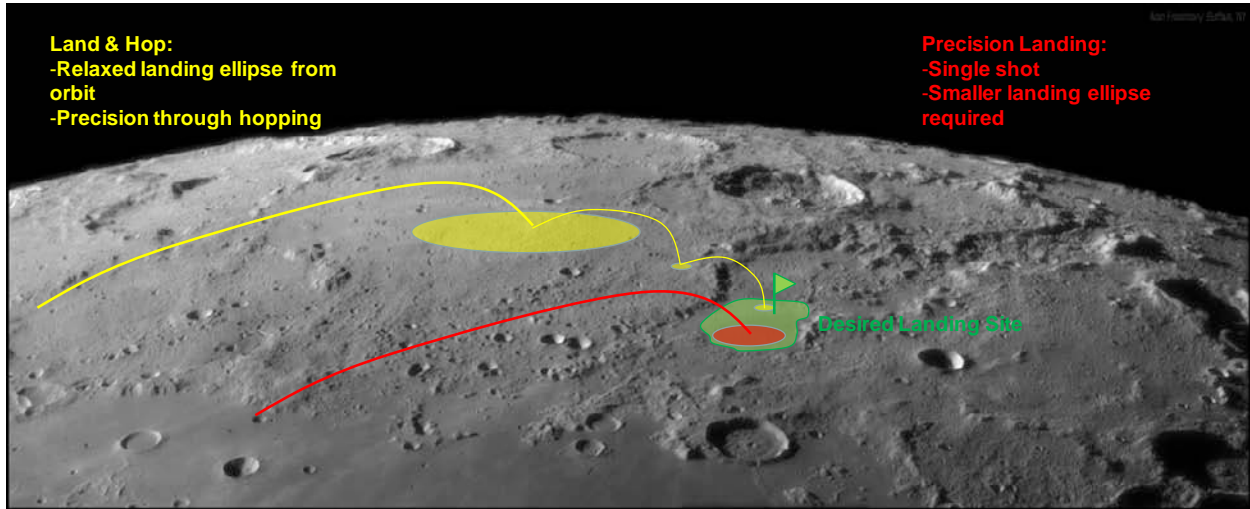


Figure 10 – Ultraprecise landings using hopping (55).

As shown in Figure 10, the hopper can use multiple hops to hone in on a desired landing target. The hopper can progressively approach the desired target by flying successive hops. Localization can be done between each hop to estimate how close the previous hop was to achieving the target and how the next hop should be targeted to head towards the final target. This can be done by using orbital reconnaissance and correlating with imagery during a hop, or between hops by integrating updated state information from onboard sensors or external navigation updates.

This method allows the hopper to safely traverse long ranges over hazardous terrain using coarser navigation and control. This reduces the complexity of the mission and enables precision global location on a planetary body.

3.1.3 Low Altitude Science Missions

There are several science missions that are uniquely enabled by hoppers. Hoppers can traverse rapidly, low to the ground, and over hazardous terrain. Furthermore, they are able to traverse while maintaining a fixed attitude and altitude.

Low and level traverses can be useful for science instruments such as magnetometers, surface imagers, and spectrometers. These sensors can view a large portion of the surface relatively quickly.

Maintaining a fixed altitude and attitude during a hop is highly desirable for taking measurements along the surface (41). A fixed altitude provides a constant field of view and range-to-surface for sensors during the hop. A fixed attitude reduces measurement noise from spacecraft slewing. A constant, predictable rate makes it easier to design and deploy sensors for science missions.

3.1.4 Low Altitude Exploration Missions

Robotic hopper missions can be used to perform site surveys for future missions or before entering into a hazardous or unknown region of interest.

Figure 11 shows the operational concept for the hopper flying over the region of interest, performing a scan and landing safely downrange. The hopper, once safely on the surface, can process the scan data and plan a precise hop from its current location to a location within the hazardous region. It can even use the hazards detected during the hop to perform terrain relative navigation against features from the hazard scan.

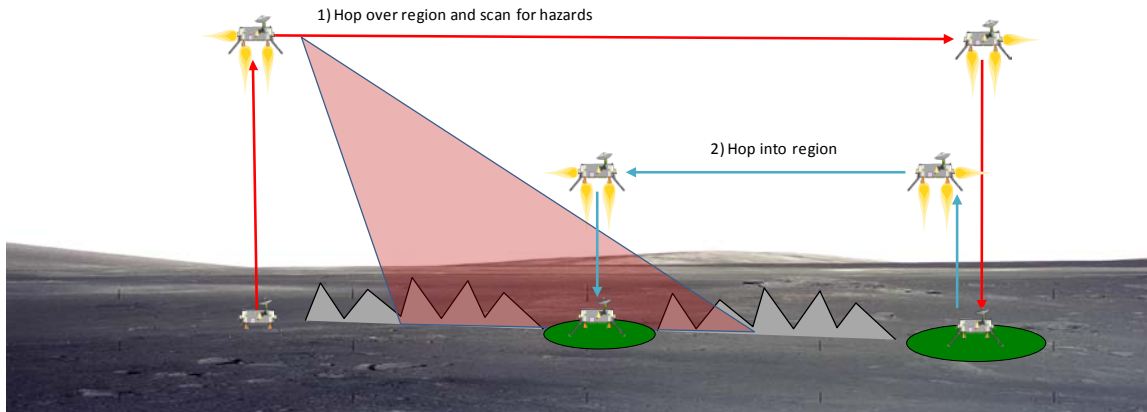


Figure 11 – Site Survey Hop Scenario. The hopper flies over the landing site and scans the surface from low altitude. Once safely landed downrange, the lander can target a hop into the hazardous region based on the hazard scan.

3.2 Steep Slope Exploration

Steep slopes may contain exposed layered regolith that can be used for studying the history of a planetary surface. These areas can be imaged or scanned by cameras and spectrometers to understand the composition of the material. These steep slopes may also have juts or crags that would harm the hopper if left undetected.

Figure 12 shows an illustration of a hopper traversing a steep slope similar to those within rilles or craters. This task requires a short-range scanning LIDAR oriented along the Z-X plane to measure ranges below, in front, and slightly above the hopper as it traverses down or up the slopes. A short-range scanning LIDAR can be used for navigation to help maintain both a constant range along the surface as well as help detect obstacles ahead.

The figure illustrates how such a sensor, scanning up and down in the direction of traverse, can help detect features and maintain a constant distance from the sloped surface.

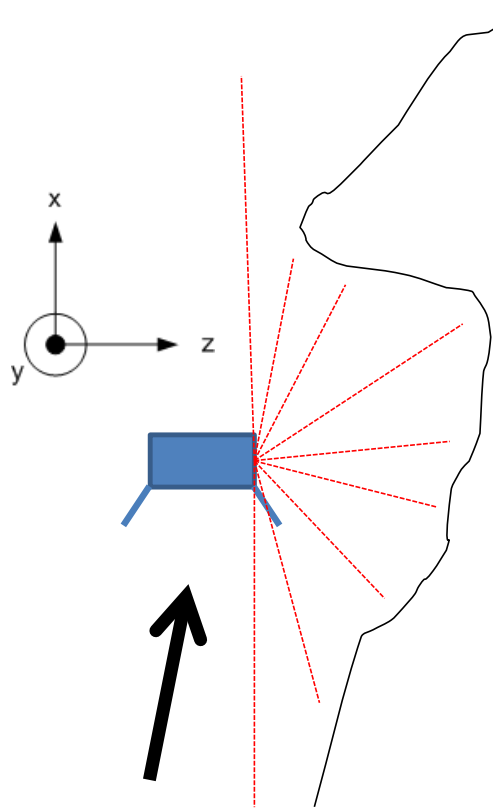


Figure 12 – Concept for navigating steep slopes using a short-range scanning LIDAR

3.3 Crater Exploration

Crater exploration is uniquely enabled by a hopper vehicle. There are several aspects of craters that make it challenging for other vehicles to explore.

First, crater rims can be very steep. Roving vehicles may be able to enter into a crater but may have to drive around the crater to look for a shallow entry point. Rovers run the risk of getting stuck on the crater rim, within the crater, or toppling down a steep slope and flipping over. Hoppers fly so they are able to enter into craters, explore the steep surfaces, detect and possibly land at the flat surfaces on the crater floor.

Once inside a crater, communication back out is more difficult because the local horizon is much higher than before. This limits the link to any communication satellites and can disable communication back to other surface assets. Sunlight within the crater may be limited, making it difficult to use solar energy for recharging batteries and creating very cold thermal environments for the vehicle.

A special mission scenario that has been put forth in recent years is exploring craters at the poles of the Moon. The polar craters have floors that may not have been exposed to sunlight. There are stipulations that they may contain deposits of water ice that have been preserved, and that are possibly even exposed. These areas are very cold and long exposures may be thermally damaging to a vehicle. Hoppers have the unique ability to hop in, perform a mission, and hop back out of a crater to

communicate gathered data, recharge batteries using solar arrays, or enter back into a thermally friendly environment to warm up components.

Understanding the morphology of a crater is useful in being able to navigate within it. The detected slope can help pinpoint the hoppers radial position within the crater. Craters are generally categorized into 3 categories (105):

- 1) Small or simple craters, which may be several kilometers or less in diameter and can be characterized by a depth-to-width ratio of 0.2 (i.e., the maximum depth is 1/5 the diameter of the crater).
- 2) Large or complex craters, which have flat floors and possibly a central peak. These craters may be few tens to hundreds of kilometers in diameter.
- 3) Multi-ring basins, which are very large craters that span a significant portion of the planetary body and can be categorized by very complex levels of cratering.

For the Moon, the cutoff diameter between simple and complex craters is about 18km (105). This cutoff is a function of gravity on each planetary body.

Figure 13 shows an illustration of a simple crater and complex crater. Understanding the general morphology of these craters, a hopper can use a short-range LIDAR to scan the surface and estimate slope. This will provide the hopper with an estimate of its radial position within the crater.

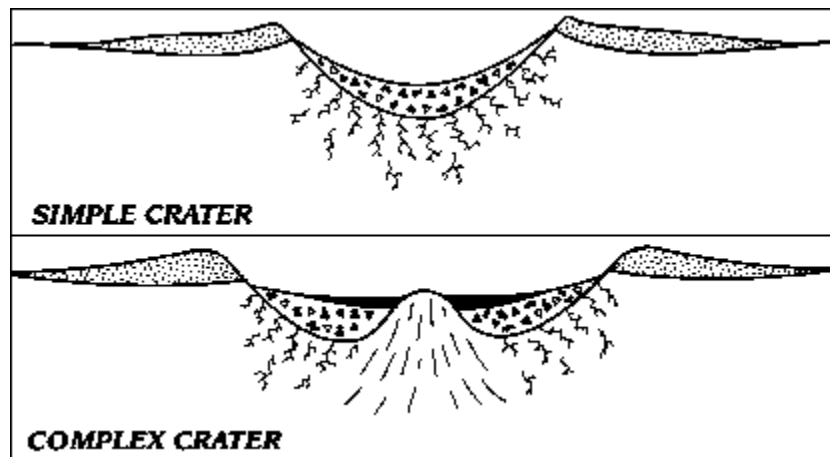


Figure 13 – Simple and Complex crater morphology (106)

Figure 14 shows a lunar crater. The shadow can be seen to cast a very distinct boundary. Knowing the location of the sun, the crater shadow line can be estimated and used to track the azimuth position of the hopper while inside the crater. As the hopper flies around, a passive optical camera can be used to calculate the angle of the shadow line. This can be then used to determine the hopper's radial and azimuthal location within the crater.



Figure 14 – Crater with prominent shadow. For most atmosphere-less, rocky planetary bodies, craters will cast shadows that have very distinct black/white boundaries (107).

3.4 Chapter 3 Summary

Chapter 3 described several hopper mission scenarios and the sensing concepts that can be used to help safely navigate over, across, or into complex regions for science and exploration missions.

Methods were described to provide localization of the vehicle once safely on the surface and during a hop traverse.

There are several missions enabled by a traverse across the surface of a planetary body. Landing through multiple hops enables very precise placement of hoppers at a globally desirable target of interest on a planetary surface. Science may be uniquely enabled by low altitude, rapid, level traverse across the surface for measuring surface, or near-surface, phenomena. Hoppers can also be used to assess hazardous or unknown areas of interest before future hops or missions enter the region.

Hoppers uniquely enable the ability to explore steep slopes and within craters. A short-range LIDAR can be used to navigate slopes while passive optical imagery can be used to maintain attitude within a crater. Measuring a crater before entering it and using the morphology as a method to understand radial location within a crater enables exploration across the entire width of a crater.

To further enable these missions, methods have been developed further in this thesis that enables the safe traverse of a hopper from one landing location to another.

The following chapters expand on the operational concept of site selection and hazard detection. A long range, shallow path angle and passive optical method provides the capability of eliminating the most hazardous landing areas from consideration. A more precise method using a short-range LIDAR is then used near the end of the hop traverse to detect surface slope and roughness in order to determine a final landing point.

4 Landing Area Selection

As described in previous sections, hazard detection research is currently looking at ways to more precisely identify individual slopes, rocks, and craters. These techniques, though capable of working under any lighting condition (in the case of using active sensors such as LIDARs) and of identifying all hazards, are inadequate for small hoppers. The mass, power, and computational resources required to house these sensors onboard a spacecraft are costly. Any mass on a hopper that is used for navigation or hazard detection limits the amount of fuel that can be carried to perform longer traverses. Large, active sensors are also range and path angle limited. Hoppers traverse rapidly over the surface and can approach landing sites at shallow path angles. A rapid method for Landing Area (LA) selection that uses smaller sensors and faster algorithms and operates at long ranges and shallow path angles is needed.

This chapter describes a new method for using shadows and lit features to rapidly assess areas where crippling hazards are more likely to exist. The basis for this new technique is taken from the analogy of a human doing site selection out of the window of a lander. Humans visually inspect the surface for clues that one area is safer than another. Bright features highlight areas of high slope, while dark features (shadows) highlight craters and rocks. This can be automated onboard and is very beneficial as a low mass, low power, low computational processing optical technique for traversing surface vehicles such as a hopper. The Apollo astronauts used visual cues to detect features like large boulders and craters (51)(52)(80). These same visual cues can be used by a sensor system to autonomously analyze safe landing area locations and redirect a hopper during a traverse from one location to another on a planetary surface.

Similar to limitations put upon the crews of the Apollo lander, this technique is limited by lighting conditions. Nonetheless, the strength of the method is that it enables rapid landing area selection to occur at high traverse speeds, over long ranges and at low path angles to the landing zone. This is key for hoppers and other rapid-traverse vehicles. Instead of identifying individual hazards, this technique defines relative safety by using both the size and density of shadows and lit features. This technique only works under certain lighting conditions, which are analyzed in this thesis. This technique does not provide absolute safety, but is coupled with a complimentary technique (described in Chapter 5) which does. The hypothesis is that, statistically, the safest areas to land in are areas that have both a low number of features (relatively low cumulative feature counts) and have a small maximum feature size. This technique guides the hopper to a safe area and the technique described in Chapter 5 is used to assess absolute safety and select a safe landing point. Together, they provide a powerful method for safe landing at a much smaller cost.

Table 4 shows how maximum feature size and number of features is used to prioritize relative safety. Priority is given to areas with lower numbers of features and smallest maximum feature size. Preference is given to having many smaller features as opposed to only a few large features. A landing vehicle will be designed to withstand certain hazard sizes. Many small features may infer many small hazards that can be overcome. The converse is that there may only be a few, large hazards in a given region, but any of these hazards may cripple the vehicle upon landing.

Table 4 – Relative Statistically Safety for Landing Area Selection

	Small Features	Large Features
Fewer Features	1. Statistically fewer and smaller hazards. This area should be statistically safer to land in.	3. Few features in the area, but the maximum size of the existing feature is large, implying a large hazard in the area. Possibilities exist, but this area should be avoided.
More Features	2. Possibly many features, but if maximum feature size is small, still relatively safe because lander can endure some level of small hazardous features.	4. Statistically unsafe. Higher chance that vehicle will be disabled upon landing by either having lots of hazards in area and/or large hazards in area.

This technique also has another distinct advantage over techniques that attempt to directly image hazards: it is able to detect hazards at shallow angles to the surface. Hoppers traverse at low altitudes, skimming the planetary surface they are traveling over (20)(27)(54). Looking at the horizon and detecting hazards thus occurs at shallow angles, where craters and rocks are seen in a profile view, as opposed to from above. This creates interesting challenges for detecting individual hazards and lends itself to a more statistical approach using features to discern areas of high feature density and/or large features.

Since the technique looks for relative safety between landing areas, it is useful when doing landing area selection at low path angles. Where other techniques incur degraded performance and are unable to directly detect hazards in the field of view, this technique is looking for relative safety by counting features of different sizes. Hazards are distinct bright/dark features that can be detected quickly and at low path angles all the way out to the horizon. As a traversing vehicle nears the desired landing location, either by achieving the desired range or by identifying of a point of interest, the possible landing areas can be continuously reassessed for safety and the solution of the landing target can be updated as information improves.

4.1 Landing Area Selection Operational Concept for Traversing Spacecraft

As illustrated in Figure 2 and Figure 5, a hopper mission consists of several modes, the most unique of which is the traverse. From a fixed point on a planetary surface, the vehicle ascends and begins to traverse to a new landing site. The traverse is a form of rapid, close-to-the-surface mobility and can be used as the means to perform science and exploration along the path or to deliver a science payload to a new location on the surface. Cunio (20) and Lanford (27) describe several mission concepts uniquely enabled by hopping, and more precisely, fixed-attitude/fixed-altitude (“hover-hop”) trajectories. A hover-hop trajectory enables a stable platform for scientific observation and surface relative sensing for navigation and site selection during traverse.

Middleton studied hopper trajectories, ranging from ballistic to hover-hop trajectories (49)(54). He showed that the delta-V penalty for hover hop trajectories was relatively low compared to ballistic

trajectories and that hover-hop trajectories have the added benefit of requiring lower T/W ratios (which directly equates to smaller actuators). Morrow (33) studied and developed techniques that could be used for propulsive control of hoppers during ascent, traverse, and descent for different hopper architectures. Regardless of the trajectory, a hopper will be approaching landing area at varying path angles and velocities. Moreover, a landing site may only come into view over the horizon with relatively short time available to make an assessment and act upon it by performing a divert

For any traverse, a hopper needs to assess landing locations along its trajectory. These sites may not have been pre-surveyed. They may lie within view of the horizon or be located over the horizon and come into view late in the traverse phase. A rapid method for detecting hazards and providing relative safety of landing areas is useful to increase the probability that a hopper will land safely upon reaching its desired landing location. This improves survivability of the vehicle, so it can be used for future hops or as a platform for stationary observations after landing.

Section 3.1.1 gives a high-level overview of the operational concept used for landing area and landing aim point selection. To expand upon this concept, Figure 15 illustrates the relative size and scale of the field of view that can be expected to be seen by a hopper's onboard camera, the size and scale of a landing area within that field of view, and the size and scale of a landing aim point within a landing area.

The Size Density Method (SDM) aims to find landing areas within the field of view that are relatively safer and provide the best probability of finding a safe landing aim point. In the field of view, there may be dozens of possible landing areas, and thousands of possible landing aim points. Landing areas are defined to be a certain size based on the mission planner's risk tolerances, understanding of the vehicle's navigation and control authority and any a priori knowledge of the terrain that is being flown into.

For this thesis, a lunar surface is used as an example. The typical field of view encompasses on the order of $\sim 1 \text{ km}^2$ of area. Landing areas were defined as $\sim 100^2 \text{ m}^2$ areas (giving ~ 100 landing areas within a field of view). Landing aim point sizes were defined to be $\sim 1 \text{ m}^2$ (giving $\sim 10,000$ LAPs per LA, and $\sim 1,000,000$ LAPs within the field of view).

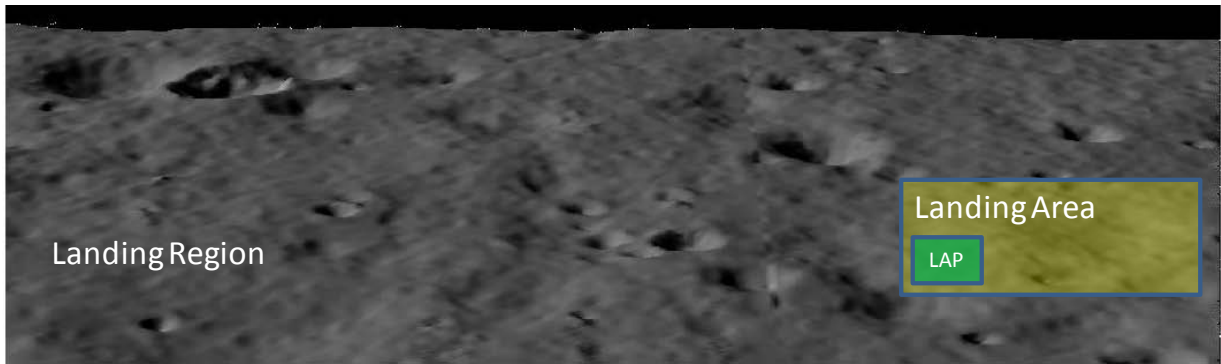
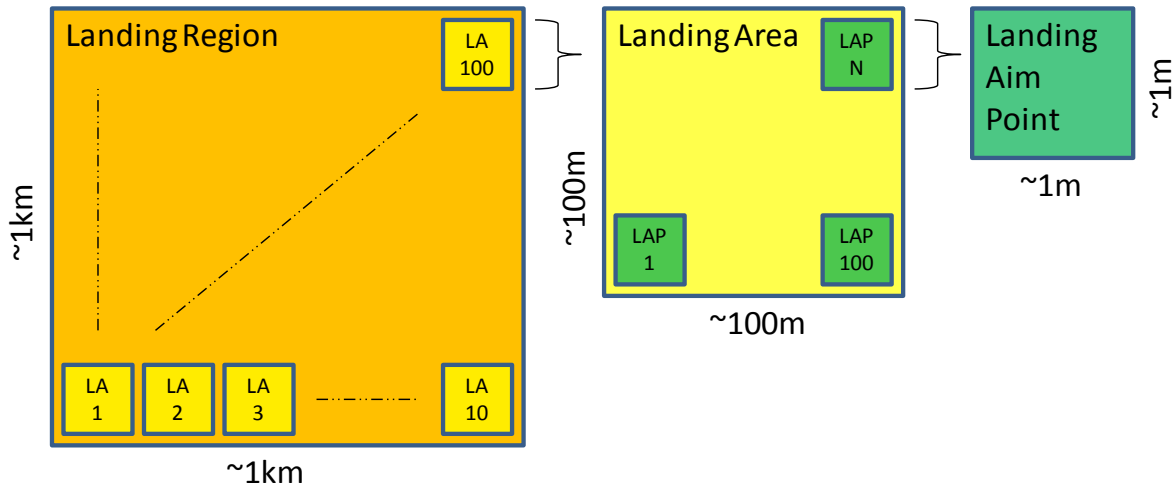


Figure 15 – Field of View, Landing Area, and Landing Aim Point. The image illustrates the field of view that may be seen from a hopper during traverse. Within the field of view there are many Landing Areas. Within a Landing Area, there are many Landing Aim Points.

The method described in this chapter develops a technique for rapidly detecting safe landing areas during a traverse. This enables a shallow path angle approach to a landing site, over-the-horizon hopper trajectories and constant reassessment of landing areas during the traverse. The analysis in this chapter shows that this method provides the ability to detect safe landing areas at shallow path angles and varying lighting conditions. The analysis also shows that this technique has computational speed advantages over higher fidelity methods while maintaining comparable performance. The use of this algorithm is also predicated on using a passive optical sensor, which has been demonstrated in space on several missions. It is a relatively low mass, low cost sensor system that can provide information for both landing area selection and surface relative navigation. Computational efficiency in a small package provides the basis for carrying this sensor onboard a small hopper and, with the use of this algorithm, enables continuous landing area selection updates throughout the traverse.

This method is constrained by lighting conditions. Lighting conditions at the desired planetary body need to be assessed as part of the mission design for a hopper mission using this method to traverse safely from one landing location to another. During a mission, the lighting conditions can be taken into account to properly plan for effective hopping from one location to another on a planetary surface.

4.2 Size Density Method

The algorithm consists of identifying the size and density of features in a given region that are on the order of the size of a lander footprint. The size and density are assessed using a grid placed over the field of view of an optical sensor pointing along the path of traverse (looking ahead). The different grid cells are possible landing area locations and are compared against each other to determine which landing area is safest by looking for the area with a low number of features and a small maximum feature size.

This technique's strength is detecting landing areas during a traverse at long ranges and shallow path angles. Other techniques rely on very precise identification of rocks and craters. This technique does not attempt to identify individual hazards, but instead looks to statistically qualify areas that are safer than others by assuming that the number and size of features correlates with the number and size of hazards in a given area. This method, coupled with a short-range, active method of direct hazard detection (described in the following chapter) provides an efficient operational concept for constant assessment of safe sites during a hopper traverse.

This chapter describes the methodology and uses several illustrative examples to demonstrate how the algorithm works. The algorithm is validated in simulation using lunar surface digital elevation maps. The landing area selection algorithm is compared against a more precise technique derived from a DEM-based approach to detecting and avoiding hazards (56). The landing area selection problem will be studied for static, overhead views, as well as dynamic traversing, low path angle trajectories.

4.2.1 Illustrative Example

Figure 16 shows an overhead illustration of the algorithm. In the left pane is a grayscale overhead image of a sample lunar surface. This image contains rocks, craters, and slopes. This image is used to illustrate the basic statistics used to determine the relative safety of landing areas in the image.

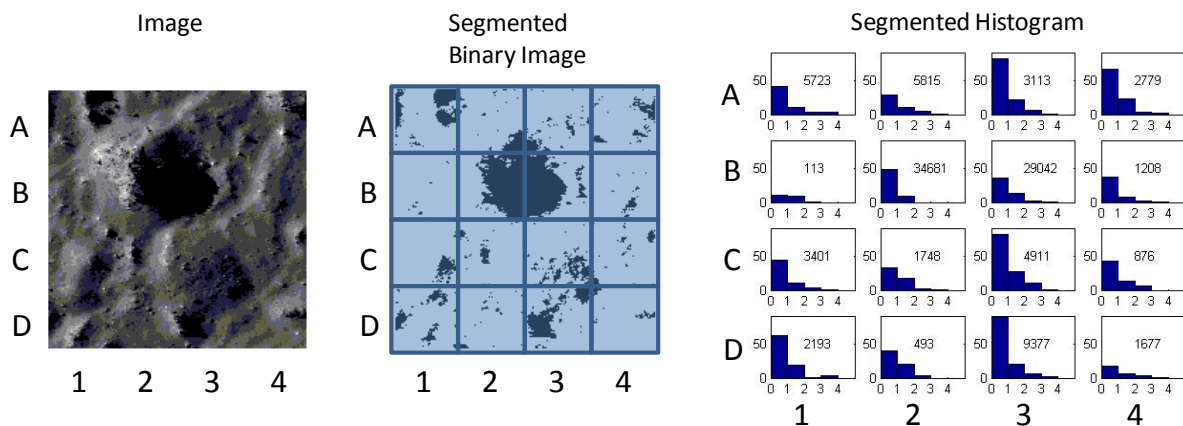


Figure 16 – Size Density Method illustration. Left: overhead image of the lunar surface. Middle: Image has been turned into a black/white image and a grid has been created. Right: each histogram plot corresponds to a grid in the center image. The size density of the features is tallied as number of features (y-axis) vs. size of features in pixels (x-axis, log scale), and the maximum feature size in pixels is reported as a standalone number in each grid cell.

The middle pane is a binary rendering of the left pane. A threshold value is chosen in the grayscale spectrum and used as a cutoff point to select between pixels that become non-features versus features

(white versus black). For simplicity in this example only the shadows (and not the bright features) are used to demonstrate hazardous features.

The literature describes various methods for determining optimal threshold values for feature detection (61)(108)(109). The thresholding algorithm used in this thesis is described in detail below.

The binary image is gridded on the order of the lander footprint to be used for counting features. For illustration purposes, Figure 16 is not drawn to scale and grid cells do not correspond to any specific lander size. The figure is being used to describe the statistical method used for landing area selection in an illustration.

The right pane represents the distributions of features of different sizes. The histograms in the right image correspond to the grid cells in the middle image. Individual features are counted by clustering connected components. In the binary image, dark pixels that are in adjacent cells are clustered together and counted as a single feature. The feature has a size recorded in pixels. Features range from 1 pixel in size to covering an entire grid cell.

Figure 17 isolates a single grid cell and defines the histogram values for the x-axis, y-axis, and the number that illustrates maximum feature size.

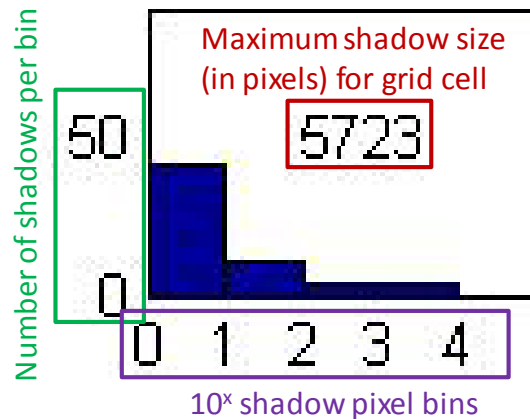


Figure 17 – Grid cell definition. The x-axis defines bins representing different feature sizes as a function of 10^x pixels. The y-axis defines how many separate features of a given size are in each bin. The number inside the grid cell identifies the largest feature size, in number of pixels, in that given grid cell.

The x-axis for the histogram is logarithmic bins corresponding to the number of features of a given size. For example, the first bin contains the small features: 10^0 (1) pixel features. The other bins show the number of features that have a size of 10^1 , 10^2 , ... pixels in size. The pixel cluster size correlates to the feature size (represented by connected clusters of pixels). The y-axis is a linear count of the number of features in each bin. Each bin is the count of the features that are on the order of the number of pixels at that bin point along the x-axis. The maximum feature size is the number at the top of each individual histogram. For example, in the illustration in Figure 16, the top left grid box (A1) has about 50 features that are 1 pixel, and about 75 features total. The maximum feature size is on the order of 10^3 pixels, but there is a relatively low count of big features in that grid cell.

With this information, the grid cells that have more or larger features can be identified. The biggest feature in the entire grid can also be found. This information can be used to provide the measure of relative safety between the different grid cells. Using this information and looking at the illustration in Figure 16, some observations can be made about the example lunar surface image in the figure:

1. Cell B-1 has the smallest maximum feature size (116 connected pixels), and inspection of the histograms demonstrates that it also has a very small number of features. It is a good candidate for containing a safe site location.
2. Cell D-2 has a small largest feature (493 connected pixels), but inspection of the area under the curve in the histograms shows that there are many small features. It is a possible candidate for safe sites.
3. Cells C-3 and D-3 have medium-sized largest features (at 9,377 and 4,911 connected pixels). But these cells have a large number of features, as can be seen by visually inspecting the area under the curve in the histogram. These areas may have safe landing locations, but should be avoided if a better solution exists.
4. Cell B-2 has the largest connected feature at 34,681 pixels. Looking at the image, it can be seen that this is the left half of the big crater located in the image. Cell B-3 has the second largest connected feature at 29,042, which is the right half of the big crater located in the image. These cells are statistically the least safe areas to visit because the presence of a large feature infers danger.

This data suggests that Cell B-1 appears safe, and would be the relatively safest location to target for landing. However, B-1 is next to grid cell B-2, which is considered unsafe. This is also weighed into the solution. It is important to not only look for the safest landing area, but to also address redirection to nearby alternatives during the approach phase.

As the vehicle continues to approach the landing area, these estimates can be refined until a safe location is found in preparation for landing. This illustration provided a high-level overview of the Size Density Method. A more detailed description is provided below.

4.3 Size Density Method Algorithm Description

4.3.1 Algorithm Flow Diagram

The Size Density Method takes in as inputs an image of the surface and the lander footprint size. The algorithm returns a ranked list of safe landing area locations. The returned landing areas are based on relative safety of one landing area over any other landing area in the field of view.

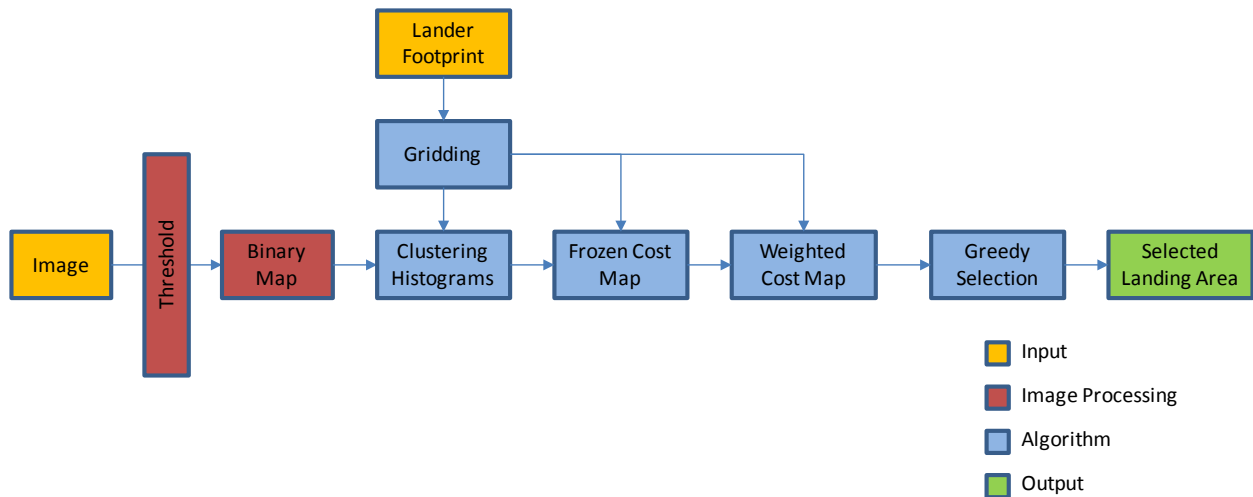


Figure 18 – Size Density Method Algorithm Flow Diagram

4.3.2 Thresholding, Gridding, and Clustering

The image of the surface enters into the algorithm and a threshold is applied to create a binary image. There are several techniques for applying dynamic threshold values to an image (108)(109). Features are not only shadows, but also bright areas. Shadows and bright areas occur because of a difference in relative slope compared to the flat surface Mare. The binary map that is created accentuates the features in the image of the planetary surface, both shadows and bright features, so two thresholds are needed: one to accentuate shadows, and another to accentuate bright features.

First, an image intensity histogram determines the spectrum of grayscale colors in the image. A mean and standard deviation are computed and used to set the light and dark threshold values. Figure 19 shows a sample lunar surface (left) and its corresponding image intensity histogram (right).

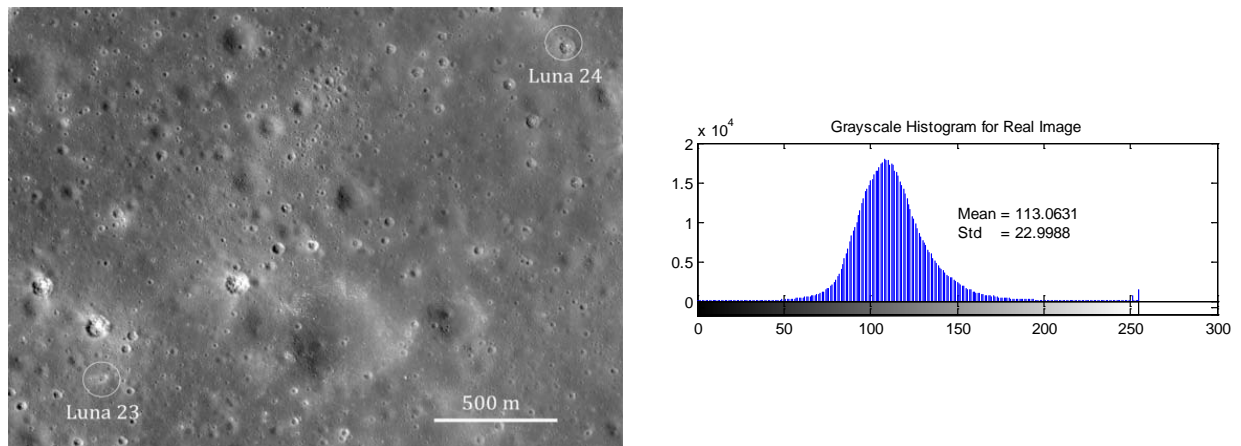


Figure 19 – Lunar image and corresponding image intensity histogram (Luna 23/24 region). Left: sample lunar surface image. Right: corresponding image intensity histogram.

The thresholds are used to create a binary map where values outside $[\text{mean}-2\sigma, \text{mean}+2\sigma]$ are considered to be features. Figure 20 shows the thresholding applied to the above image. The bright and dark identified and combined to create a binary feature map.

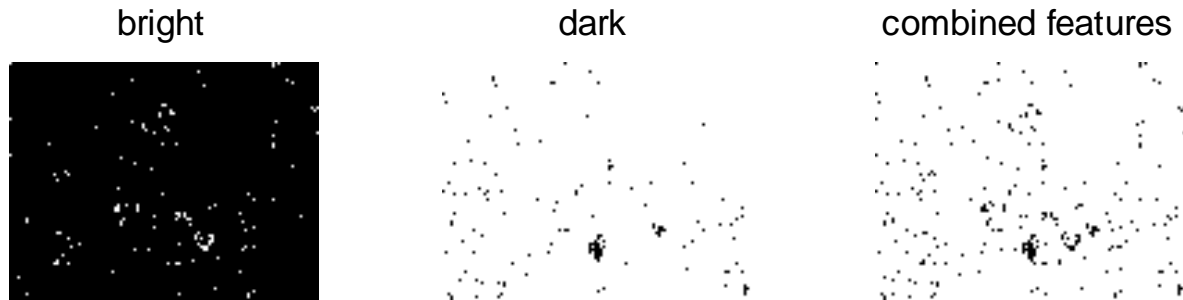


Figure 20 – Binary feature map (Luna 23/24 photograph). Bright features are identified in white (left), dark features in black (middle), and combined to show all features in black (right).

Once the thresholds are determined and a binary image created, the image is gridded. The grid spacing (110) is a function of:

- desired landing area size (from mission planners)
- lander footprint
- sensor FOV
- camera pointing angle (which is a function of spacecraft attitude and camera mounting angle)
- estimated altitude
- radius of the planetary body

Mission planners will determine a desired landing area that is acceptable for the given hopper mission. Some missions may have a need to land in a very small region to meet the science or exploration requirements. Others may have more flexibility in their final landing location and may just need to achieve a long range traverse and land safely.

Figure 21 shows the Vehicle Footprint Dispersion Ellipse (VFDE) (79). The VFDE is the lander footprint plus the expected dispersion errors at landing. The vehicle navigation and actuators will have expected errors and, as a vehicle descends to the surface for landing, it is inevitable that it will not land perfectly. The VFDE is an effective landing footprint used to conservatively pick a landing aim point (the lander is expected to land within this area given the expected vehicle dispersions derived from pre-flight simulations). The better the navigation solution and actuators, the less the expected dispersions will be.

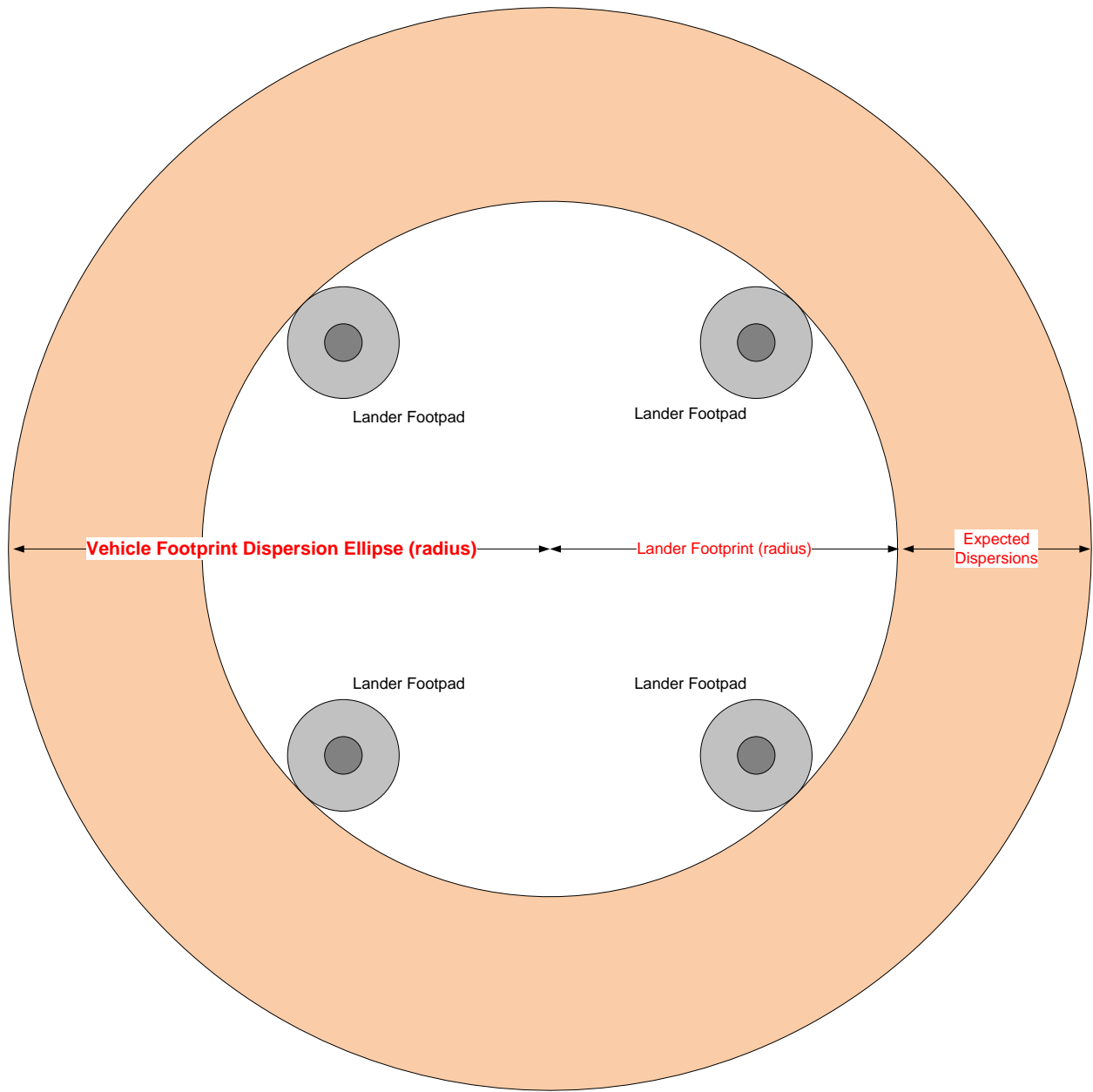


Figure 21 – Vehicle Footprint Dispersion Ellipse (VFDE). The VFDE is the lander footprint plus any expected dispersion error at landing.

The sensor FOV, camera pointing angle, hopper altitude, and planetary radius determine the geometry of what will be observed by the passive optical sensor during a traverse. Figure 22 shows the gridding geometry parameters. These parameters are used to determine the grid spacing in the equations below. Figure 23 shows the angles used to determine what portion of the surface is located in the field of view for gridding.

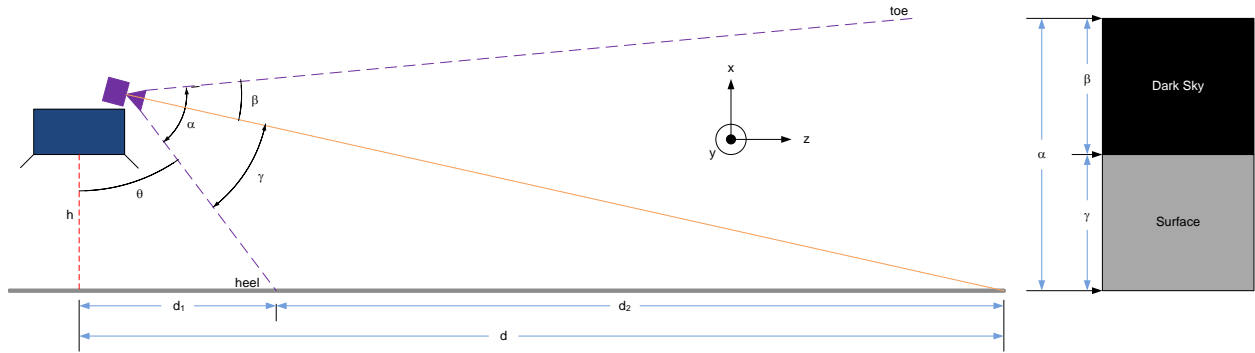


Figure 22 – Gridding Geometry Parameter Diagram

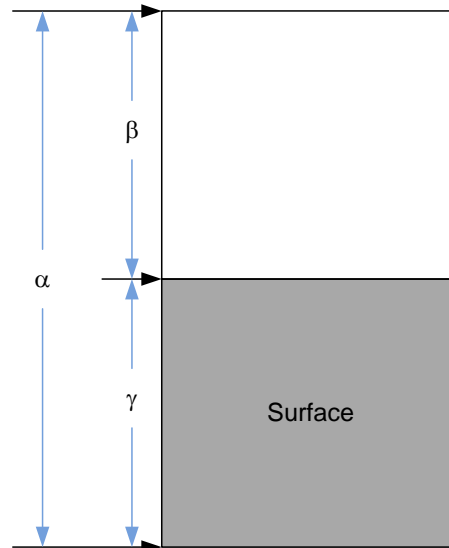


Figure 23 – Field of View Angle Geometry

First, the planetary radius and the altitude estimate are used to define the distance to the true horizon given by:

Equation 1
$$d = \sqrt{2rh + h^2}$$

where:

- d** = distance to the horizon
- r** = radius of planetary body
- h** = estimated altitude above mean surface

The distance of the surface that is visible is given by:

Equation 2
$$d_2 = d - h \tan \theta$$

where:

- d_2 = surface distance that is visible
- d = distance to the horizon
- h = estimated altitude
- θ = angle between nadir and the heel of the FOV

Figure 24 shows an illustrative example of gridding for a forward-looking image of a lunar surface. As can be seen, the grid does not include the sky. Methods for robust detection and removal of the horizon have been studied in the literature (111)(112). For this analysis, the horizon was removed by searching down each column in the binary black and white image until a non-black pixel was found. The horizon curve is found across the image in this way. The lowest elevation on the horizon curve is used as the defining point of the horizon and a straight line is drawn across the image going through that lowest point.

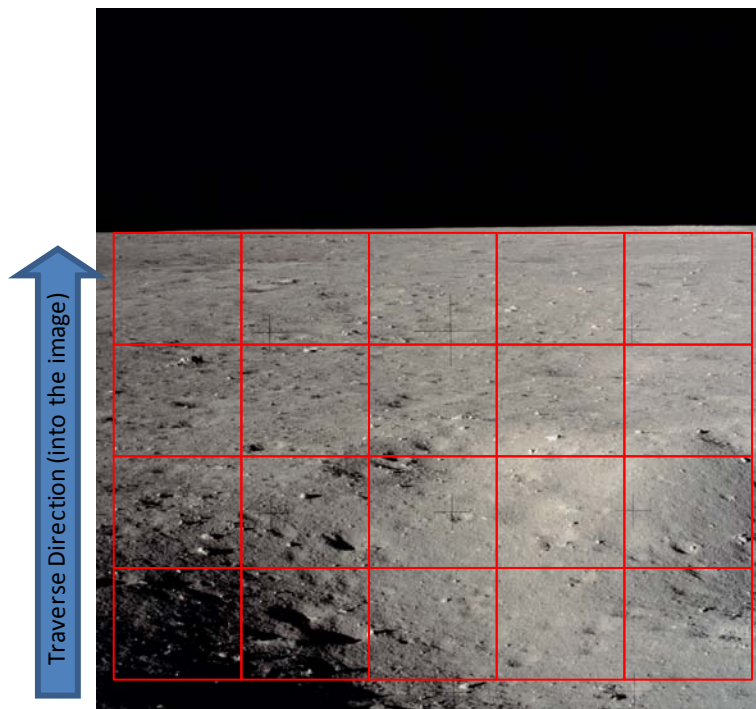


Figure 24 – Gridding Illustration. The traverse direction (direction of travel) is into the image towards the horizon.

The number of pixels per grid cell along the traverse direction can be computed from the number of pixels in the traverse direction of the camera being used multiplied by the ratio of γ to α .

Equation 3
$$pixels_{chopped} = \frac{\gamma}{\alpha} pixels_{total}$$

where:

- $pixels_{chopped}$ = pixels remaining in the traverse direction with horizon removed
- γ = angle between the heel and center of the FOV

α = FOV of the camera
 $pixels_{total}$ = pixels in the traverse direction of the full image

$pixels_{chopped}$ is the number of pixels corresponding to the distance, d_2 . An average ground sample distance (distance per pixel), GSD , can be computed by:

Equation 4
$$GSD = \frac{d_2}{pixels_{chopped}}$$

A slightly more complex solution can be used by determining the angle to each row of pixels in the image and scaling the GSD as a function of angle from nadir. This has not been used in the formulation in this thesis. Instead the average GSD is used as described above. An alternative formulation is to scale the cost of each grid cell as the distance downrange. Grid cells further downrange are less resolved, so have more uncertainty in the detection of features. These cells are given relatively higher weights, in terms of safety, in the algorithm. Since the algorithm is designed to assess landing areas rapidly, the entire technique can be run throughout a traverse. If the objective of the hop is to achieve a desired range from the initial takeoff point, the corresponding grid cells (e.g., the row of cells) that match the estimated downrange distance can be isolated and assessed for safe landing areas.

To have proper statistics in the histograms used for the Size Density Method (SDM), there needs to be a proper balance of the number of pixels per grid cell and the number of grid cells over the entire image. A theoretical minimum value would be to set the nominal grid cell length greater than or equal to the VFDE. A theoretical maximum value would be to set the nominal grid cell size less than or equal to half the FOV (so there are at least 2 distinct areas to assess). Another method, which is used for this thesis, is to estimate a landing area size that will statistically provide enough non-overlapping landing aim points in the landing area to statistically ensure that a safe landing aim point exists in the landing area. For example, a 1m diameter lander would only have 4 distinct landing aim points in a 2m x 2m landing area, while the same lander would have 10,000 distinct landing aim points in a 100m x 100m landing area. This tradeoff has both computational and performance effects on choosing a landing area. The calculations for choosing the grid spacing are given below. These considerations need to be taken into account by mission planners when choosing a landing area size.

Given the GSD , $VFDE$, number of pixels in the traverse direction and number of landing aim points desired per landing area, the grid size and number of grid cells can be computed:

Equation 5
$$\#GridCells = \frac{(\#Pixels)(GSD)}{(VFDE)(\sqrt{\#LAPs})}$$

where:

#GridCells = total number of grid cells in a given direction (either downrange or crosstrack)
#Pixels = number of pixels in the image in a given direction
VFDE = VFDE diameter in meters
GSD = GSD in meters
#LAPs = number of landing aim points desired per landing area

Equation 5 calculates the number of grid cells in a given direction. This thesis assumes that the number of grid cells per side is equal in the downrange and crosstrack direction and uses Equation 5 in the downrange direction. This does not have to be the case, and can be easily altered. For a given distribution of grid cells, the size in pixels of each side of a grid cell can be calculated by:

$$\text{Equation 6} \quad \#Pixels_{GridCell} = \frac{\#Pixels}{\#GridCells}$$

where:

- #Pixels_{GridCell}** = number of pixels for a given side of the grid cell
- #GridCells** = total number of grid cells in a given direction (either downrange or crosstrack)
- #Pixels** = number of pixels in the image in a given direction

Once the number and size of grid cells are determined, the number and size of features per grid cell can be computed. The binary feature image is first created and a clustering algorithm is then run to connect components (neighboring feature pixels) and to identify individual features in the image (111)(113). Each connected cluster is a feature and has an associated size (in pixels). Each feature is binned into a grid cell (features can be chopped up between several grid cells, as described above).

4.3.3 Histograms, and Weighted Cost Map

In the previous section, features were identified by clustering neighboring pixels. Knowing the grid cell spacing, and having defined all the features in the image, features are then binned as described in Figure 17. The number and size of features per grid cell are recorded for each grid cell to be used in the calculation of the weighted cost metric. A fast algorithm utilizing both the size and density of features is used to create a weighted cost map of the featured surface that identifies not only which individual landing areas are relatively safe, but also weights multiple landing areas of low cost together to create large regions that are safe. This landing area selection method is more robust because it points the vehicle towards a larger area with more possibilities in case a late divert is needed.

The cost of each grid cell is given by the dot product of the bin sizes with the vector of feature counts, for each grid cell (i.e., landing area):

$$\text{Equation 7} \quad Cost_{i,j} = binSizes^N \cdot \#_{i,j}^{features}$$

where:

- Cost_{i,j}** = cost of each grid cell
- binSizes** = vector defining the feature size bins
- N** = weighting factor between size and number of features
- #_{i,j}^{features}** = vector of feature counts, binned by size, for each grid cell

BinSize is the different sizes of bins for counting features, the x-axis in Figure 17. For the analysis in this thesis, these values are logarithmically increasing (i.e. 1, 10, 100, 100, 10000 pixel features). The vector

of feature counts, $\#^{features}$, is the number of features of a given **binSize** in the given grid cell, described above in Figure 17 as the y-axis. The value **N** is used to weight size versus number of features. If **N** is greater than 1, then feature size is weighted higher, if **N** is less than 1, then feature number is weighted higher.

The metric in Equation 7 was chosen as the tradeoff between size and density of features. Versions of the metric were tested using other parameters: maximum shadow size as a constraint, linear (as opposed to logarithmic) scaling for **binSizes**, a linear weighting factor (as opposed to a power law weighting), and the use of only shadows as features (excluding bright features). The implementation in Equation 7 provides a good trade of speed and performance. Maximum shadow size as a constraint and linear scaling for **binSizes** did not produce improved results, while slowing down the performance of the SDM. A power law weighting factor allowed scaling between size and density easier than a linear weighting factor (**N** multiplied by the other terms in Equation 7). The inclusion of bright features into the SDM doubled the computation time required, but greatly improved the detection of large features, such as craters. The inclusion of bright features was incorporated into the algorithm, whereas the original just used shadows as a surrogate for hazard detection.

These values are normalized so that the cost map contains a coarse grid with values between 0 (low cost) and 1 (high cost). This initial cost map is referred to as the “Frozen Cost Map.” The Frozen Cost Map contains the individual costs of each landing area relative to all others (normalized between 0 and 1). This metric can determine the safest grid cells described in Table 4.

This is also where a scaling parameter based on distance can be applied to the grid cells. Cells that are further (i.e., higher in the image) can be penalized as more risky because the features in those cells are not as well resolved as the ones that are closer (i.e. lower in the image).

The Frozen Cost Map has no dependence on neighboring cells. It is used to create a smoothed-out Weighted Cost Map to determine the safest large-scale regions in the landing region. This directs the solution towards a region of multiple landing areas with low cost. The SDM is used to determine the relative safety between all landing areas in the landing region. The weighted cost map will have a global minimum and global maximum. The global minimum value is set to 0 (safest relative landing area) and the global maximum is set to 1 (most dangerous relative landing area).

The cost metric is not a measure of absolute safety, but a measure of relative safety. A traversing hopper may not have knowledge of what hazards lie in the landing region, but will still need to land. The purpose of the SDM is to point the hopper at the landing area in the landing region that has the highest probability of containing the most safe landing aim points.

To develop the Weighted Cost Map from the Frozen Cost Map, the algorithm uses a 2-dimensional Gaussian filter to smooth the discrete values in the Frozen Cost Map by performing a 2D convolution between the Gaussian and frozen cost map. This generates a Weighted Cost Map with a global minimum. The weighted cost map blends landing areas with low cost together and those with high cost together. This produces solutions where the safest landing areas are not only safe themselves, but have

safe neighbors. This also takes safe areas that may be in the middle of a large hazardous region and devalues them as a high-ranking choice for landing area selection.

Equation 8 *Frozen Cost Map* \otimes *2D Gaussian* = *Weighted Cost Map*

This two-dimensional weighted cost map is used to find the global minimum, and a number of other solutions with increasing cost, based on the number of landing areas desired. A greedy selection algorithm described in Cohanin & Collins (59) is used to select the LA with the lowest cost. It then selects successive points based on a “spread” parameter that ensures overlap of landing area locations does not occur. This provides diversity in landing regions that have been identified as safe.

Figure 25 shows a flow diagram of how areas are selected. Landing areas are rank ordered by the value in the weighted cost map and greedily selected. As long as landing areas do not overlap each other, based on the “spread” parameter, and they are next in the order, they are recorded until the desired number of landing areas is recorded. Greedy selection, picking the globally best solutions, is one method of gathering landing aim points. Alternatively, solutions can be chosen by finding and rank ordering all the local minima in the cost map. This operation is more computational expensive, but is a viable alternative.

Cohanin & Collins (59) describes how the greedy selection can be used with other cost maps to weigh the importance of avoiding hazards against other factors. One possible factor that would counteract the effects of landing near hazards may be the desire to land in a certain area or near certain identified features (which may be hazardous). This metric is known as Distance to Nearest Point of Interest (DTNPOI). Another cost function may be used to minimize fuel usage. The method is capable of including and weighting different cost maps, as described in the paper. For this thesis, the sole objective is hazard avoidance.

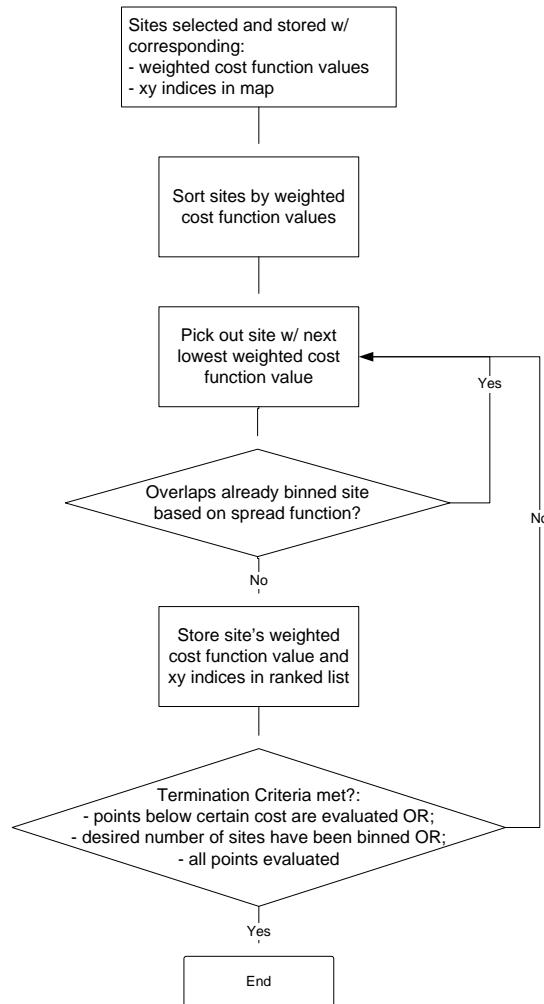


Figure 25 – Greedy Selection Flow Diagram. Landing areas are sorted by cost. The first in the list is picked and placed into the bin for storing landing area locations and cost values. The remaining landing areas in the sorted list are progressively assessed: if the landing area overlaps with another within the spread function, it is passed, otherwise it is kept. The algorithm continues until the desired number of landing areas is identified.

Figure 26 shows how the “spread” parameter works. Based on the value for “spread”, selected landing areas may overlap, touch but not overlap, or have additional spacing. The most practical scenario is to have the “spread” parameter be equal to or greater than the **VFDE**. This creates more diversity in the possible solutions presented.

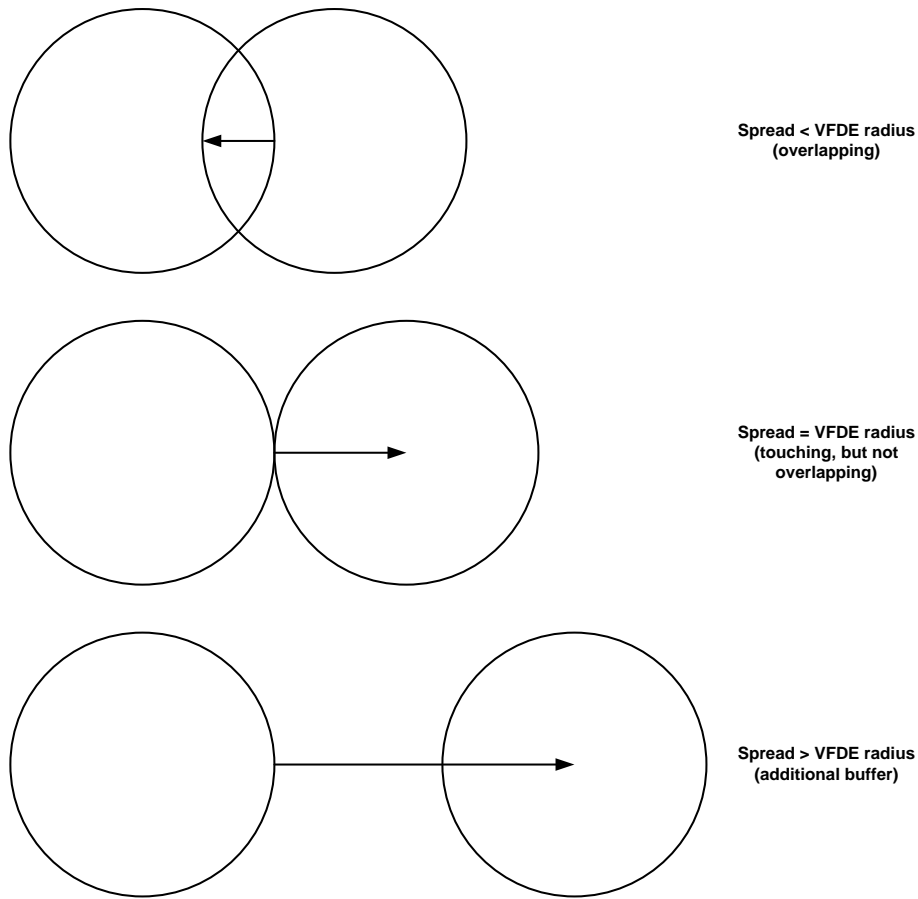


Figure 26 – “Spread” Parameter. If “spread” is less than the VFDE, solutions overlap. If “spread” is equal to the VFDE, then solutions touch, but do not overlap. If “spread” is greater than the VFDE, then there is additional buffer between solutions. This can be useful to create diversity in the solutions picked.

4.4 Size Density Method Simulations and Results

To show the utility of this algorithm, this section will study the following aspects, which are judged to be important in understanding its performance and limitations:

- Lighting conditions
- Viewing angles

The algorithm is also compared to a DEM-based Hazard Detection Method (56) to compare performance and computational speed.

To analyze the method, DEMs from LRO are used to render the surface (114). Lighting and surface shading are provided to simulate different views and shadow lengths. The sun’s elevation, the perspective of the vehicle (vehicle elevation angle) and the relative angle between the sun and the viewer (the viewer-to-sun azimuth) are all studied to determine the effects of lighting on the algorithm. Figure 27 shows an illustration of these angles. Appendix A describes the details of the surface rendering method used in this thesis to create surface images that are properly lit and displayed based on sun and view angles.

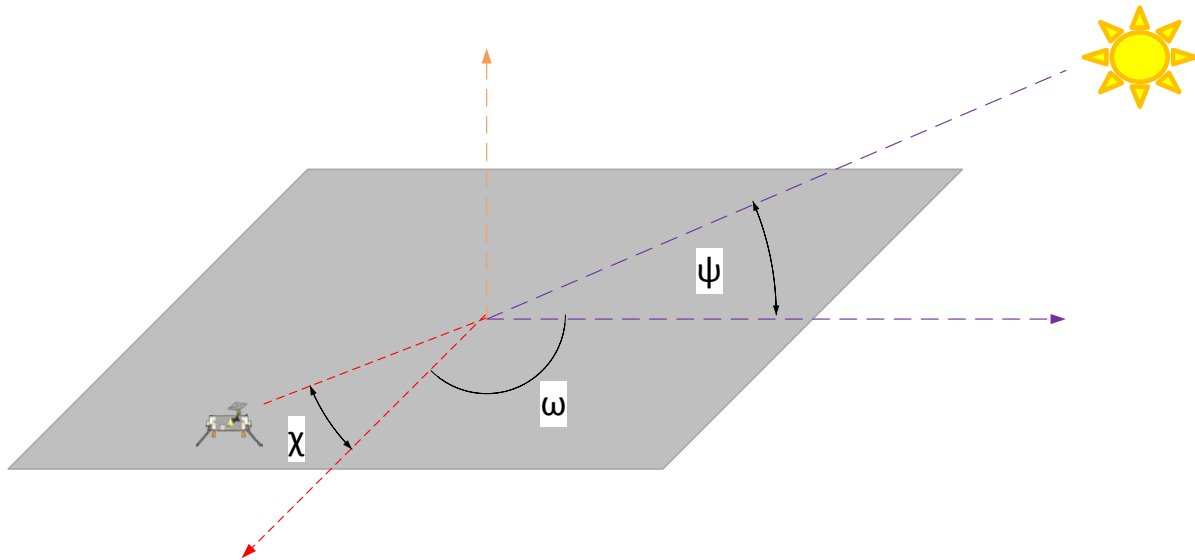


Figure 27 – Angles for applying lighting conditions to DEMs. Sun elevation (ψ), view elevation (χ), and view-to-sun azimuth (ω)

4.4.1 Simulation Environment for Comparison of Techniques

A very precise way to detect hazards is to directly assess a topographic map that is created through active sensing, such as a LIDAR. This technique uses a ranging sensor to detect the 2½ dimensional² topography of the surface. This method is precise, but can require significant computational resources, and is limited by both range and path angle. Stereographic images can also be used to create topographic maps of surfaces, but are limited in precision by the baseline of the stereo camera, and require another measurement to provide scale to the images. Maps created in this fashion are referred to as digital elevation maps (DEM).

The method described in this thesis, the Size Density Method, attempts to maintain a high level of performance in aiding in landing area selection at long ranges and shallow path angles, while doing this for a relatively low computational effort. This technique is limited by lighting conditions.

A simulation environment was created for comparing the performance of the Size Density Method to the DEM-based technique described in Johnson et al (56). A flow diagram of the simulation environment is provided in Figure 28.

The simulation environment generates a rendering of a digital elevation map to be used for all techniques (Appendix A). The DEM is then run through an algorithm to properly shade and shadow the surface to make it look lunar-like. The proper lighting conditions are applied for detecting shadows and bright features.

The DEM-based technique uses the DEM to determine rocks, craters, and slopes that are on the landscape. The Size Density Method uses the rendered image to detect hazards.

² 2½ dimensionality refers to the inability of a sensor to “look through” surfaces, which means that surface features located behind others in the line of sight of the sensor are not detected.

The methods are compared using the DEM-based method as the “truth” for SDM to be compared against. Safe landing area locations are compared between the DEM-based method and SDM to validate the SDM’s performance. The simulation environment also records the processor time required to run each algorithm. These times are recorded and averaged over many simulations.

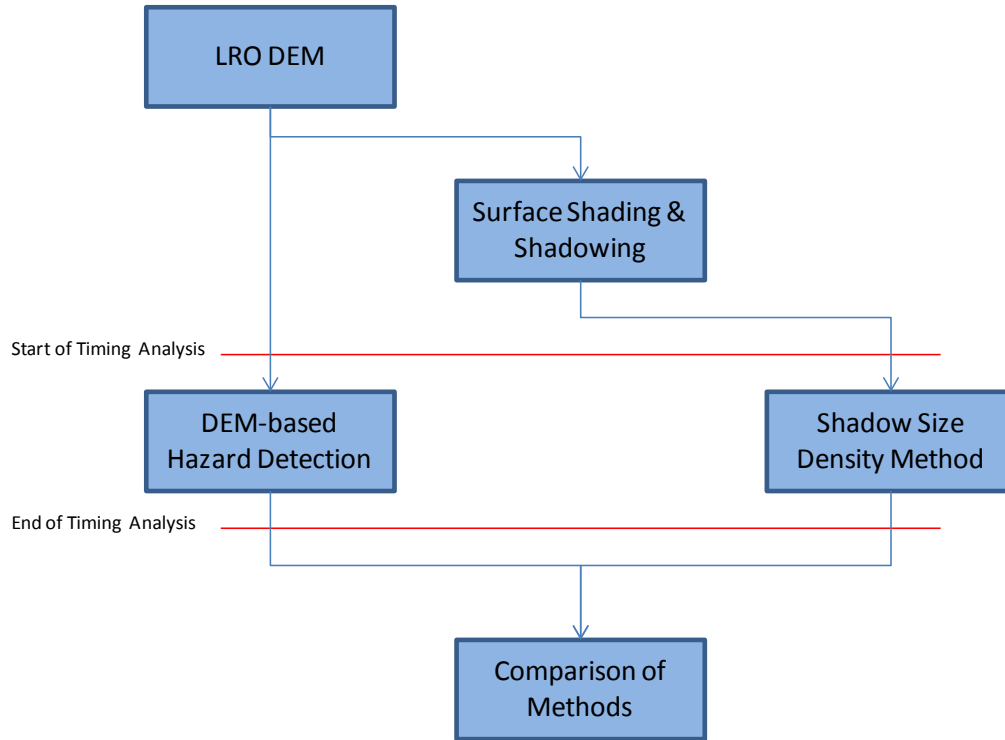


Figure 28 – Flow Diagram of Simulation Environment

4.4.2 Analysis Overview

The Size Density Method was run through several tests to better understand its performance:

- 1) Comparison to a more precise DEM-based technique for both speed and performance
 - a. Relative cost comparison
 - b. Comparison of SDM to an absolute metric
 - c. Timing between the DEM-based technique and SDM
- 2) Weighting between number and size of features in SDM
- 3) Sun and view angle study of SDM on rendered images

The computational efficiency and detection performance are compared between the Size Density Method and a more precise hazard detection method based on a method by Johnson et al. (56)(57) that detects slope and roughness for a filled DEM.

To address some of the limitations of the algorithm, simulations were performed with varying lighting conditions. Similar to the lighting conditions faced by the Apollo astronauts during landing, the ideal lighting conditions varied between 10 to 40 degrees sun elevation angle (51)(52)(80). Landscapes with

sun elevation angles below 5 degrees were washed out in shadows, while landscapes with sun elevation angles above 45 degrees cast small shadows (mainly only for craters).

Sun azimuth for feature detection comes into play as a function of view elevation angle. As the azimuth shifts from directly behind, to the side, to directly in front, rock shadows become more detectable as their shadows come more into view. As the sun moves from directly behind, to the side, to the front, crater shadows become more detectable. The simulation did not model the specular reflectance of the sun and its effects on optics when it is directly in the camera field of view so it was assumed that the sun directly in front is a viable sun azimuth for simulation. In reality, the sun can be blinding (for both humans and sensor optics).

To demonstrate the power and robustness of the Size Density Method, several static simulations are presented with varying view angles to show that the relative safety of solutions is maintained while path angles are lowered to very shallow path angles.

4.4.3 Modified DEM-based Hazard Detection Method (MDM)

The Modified DEM-based Hazard Detection Method is adapted from Johnson et al. (56). Figure 29 shows a simple flow diagram of the technique from Johnson et al (56). The method works from the development of a DEM, through the identification of hazards, to the selection of safe landing locations. Using techniques developed previously for hazard detection using DEMs (56)(57)(58)(59), the mean surface is computed along with deviations from that surface, which correspond to hazards (rocks, slopes, and craters).

Identified hazards are marked as no-landing zones and are enlarged by the lander footprint radius to ensure the lander does not overlap the hazard. The safety metric is to maximize the Distance-to-Nearest-Hazard (DTNH). The algorithm described in Johnson et al. (56) and Cohanin & Collins (58)(59) uses metrics, like DTNH, to select a set of non-overlapping safe landing aim points using a greedy search algorithm of the cost function map.

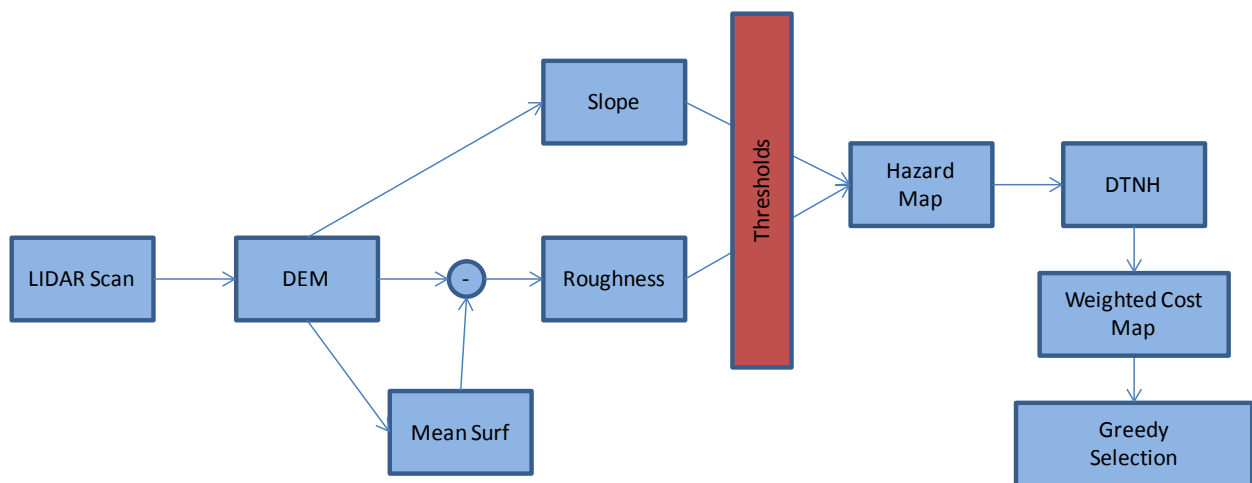


Figure 29 – Flow diagram of DEM-based Hazard Detection Method

This thesis uses a modified form of the algorithm described by Johnson et al. (56). Instead of using thresholds as a binary gate, values below the threshold have a linearly decreasing cost associated with them. This improves the hazard detection method by weighting cost values very close to the threshold. Instead of using DTNH, a gridded frozen cost map is created and a 2D Gaussian is used to add the dependence on cost of neighboring cells. This method is treated as “truth” to compare against SDM, so DEM generation is considered perfect.

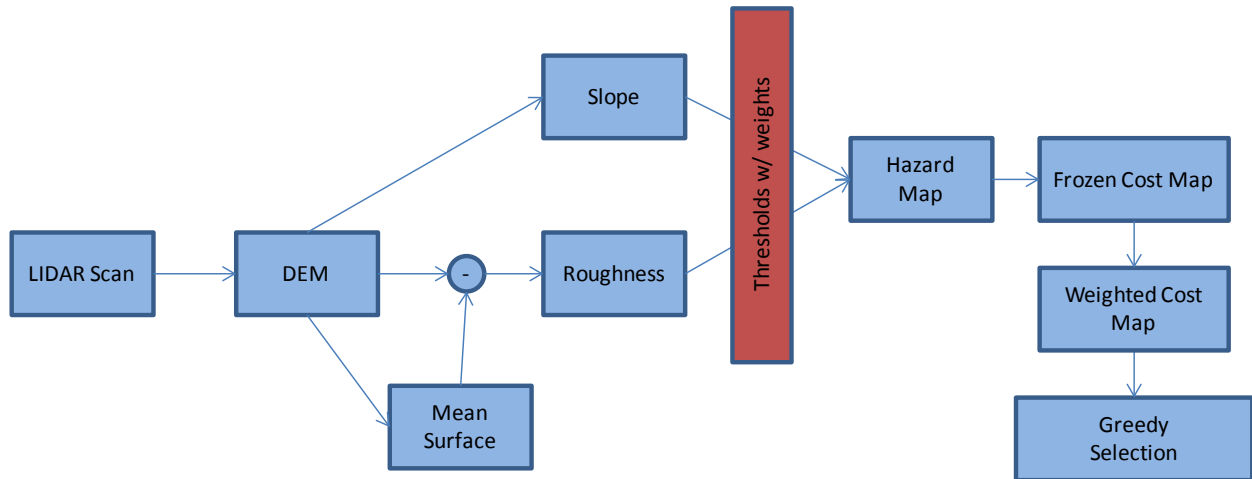


Figure 30 – Flow diagram of Modified DEM-based Hazard Detection Method

The Modified DEM-based Hazard Detection Method (MDM) has relative and absolute safety metric incorporated into it. For the relative metric, hazards are still detected based on a threshold, but weighted. For the absolute metric, hazards have binary costs (good or bad) and LAs are judged by the fraction of safe versus hazardous LAPs within the LA. Both DEM-based maps are gridded in the same manner as the SDM to provide an apples-to-apples comparison of the costs between landing areas.

The Luna 23/24 photograph is approximately a 2km x 2.5km area of the Moon. The corresponding LRO DEM of the same location is given below in Figure 31. The DEM is 941 x 1231 pixels where each pixel is at a 2 meter posting. The elevation resolution is 1 meter, and is denoted from the mean surface elevation of the Moon. The color bar in the image represents the altitudes, with -3705m being the lowest elevation, and -3655m being the highest (50 meter elevation change over the range of this lunar surface location).

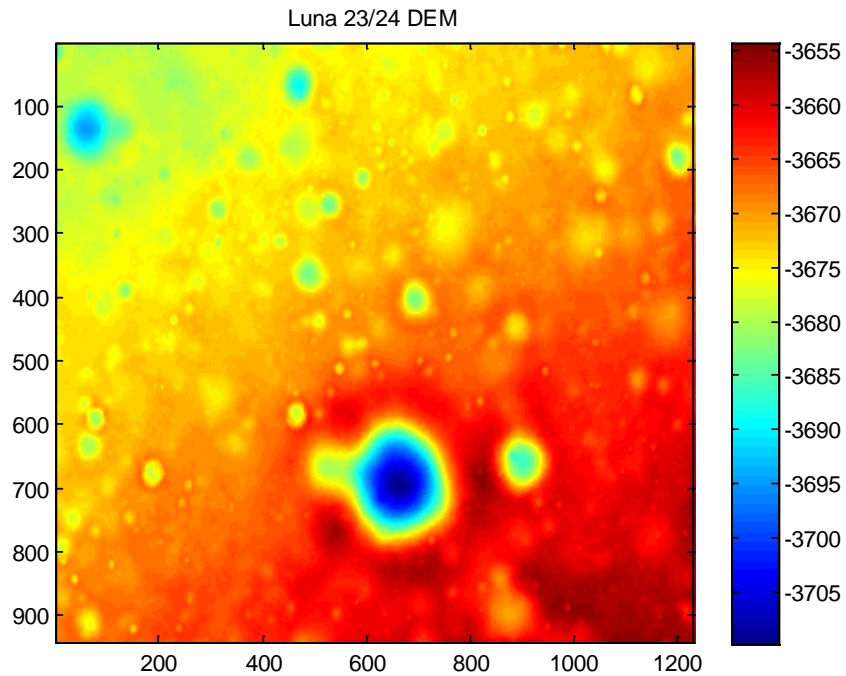


Figure 31 – Luna 23/24 DEM

At this resolution, small rocks and craters smaller than a typical small lander/hopper cannot be detected, but since SDM is performing gross hazard detection, the main hazards will be very large features: craters, large boulders (>2m in diameter), and steep slopes. The MDM can be applied to the DEM to understand the large scale crater, slope, and rock hazards in the map to compare against the SDM.

From the DEM, the mean surface and slope value at each point is calculated. The mean surface is subtracted from the original DEM to get a sense of large-scale roughness in the map. The slope and roughness metrics can be used to create a cost map to compare against SDM.

For this analysis, it is assumed that a slope above 10 degrees and any detected roughness over 30 centimeters are considered hazardous. Figure 32 shows the slope map of the Luna23/24 surface.

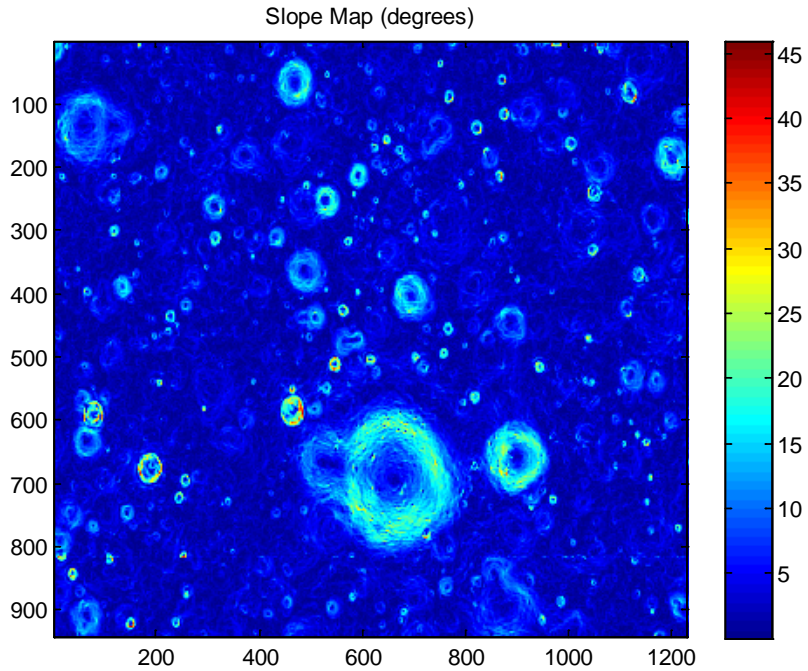


Figure 32 – Luna 23/24 slope map

Figure 33 shows the roughness map for the Luna 23/24 surface. Since the vertical resolution of the DEM is only 1 meter, the roughness map is weighted less in the generation of the overall hazard map.

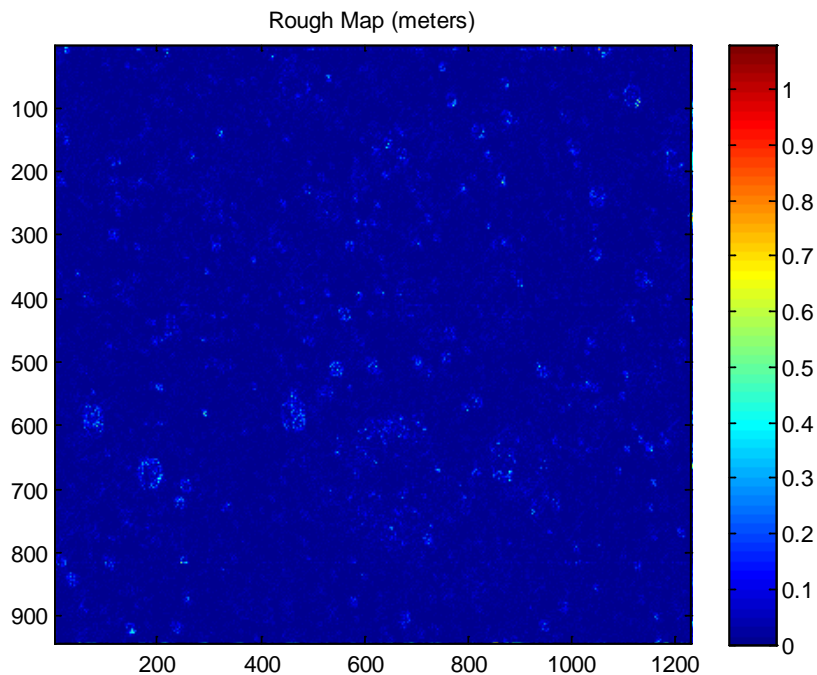


Figure 33 – Luna 23/24 roughness map

Figure 34 shows the hazard map which is a blend of the roughness and slope maps with a linear cost applied for slopes and roughness below the threshold. A cost of 1 is an area that violates either the

slope or roughness hazard tolerance. A cost of 2 violates both constraints. All other costs are a gradation of slope and roughness costs.

In the DEM-based method, DTNH was applied at this point. In the modified DEM-based method, the hazard costs are summed up in a given landing area. To match the SDM, the same landing area sizes are used and the hazard costs are summed up within each landing area.

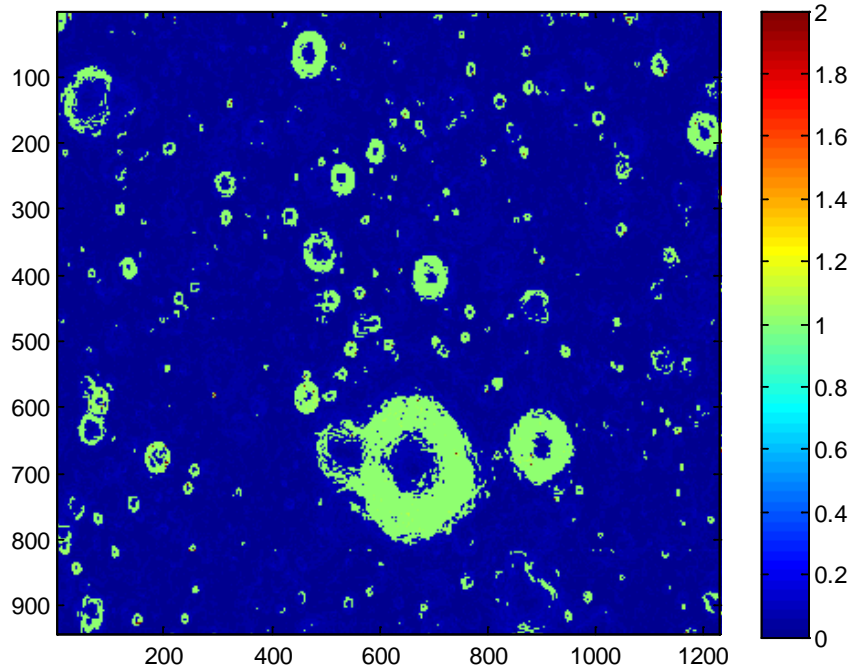


Figure 34 – Luna 23/24 blended hazard map

Figure 35 shows the frozen cost map given the hazard map. The areas of red have the highest summed costs, while the areas of blue have the lowest. The frozen cost map shown here is normalized to differentiate between the lowest cost landing area (cost of 0) and the highest cost area (cost of 1).

The area has been split into 32 x 32 landing areas (1024 landing areas). Each landing area is approximately 60m x 75m. This will also be the landing area size used on the rendered images that have SDM applied to them.

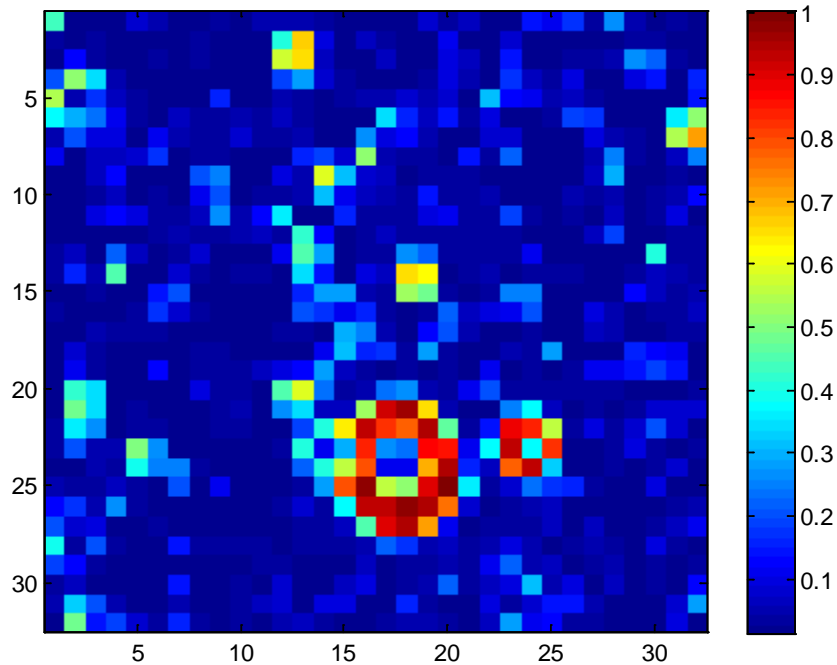


Figure 35 – Luna 23/24 MDM Frozen Cost Map

The frozen cost map captures the relative cost of each landing area. However, as can be seen, there are landing areas of very low cost next to landing areas of high cost. For example, the large crater theoretically has a flat, featureless bottom, but that does not mean that a hopper targeting that area will have a high probability of safely landing. If for any reason the hopper is forced to divert downrange, then there will not be many relatively safe LAs nearby.

During the hopper traverse, landing area selection can be used from a long distance to judge if the possibility of many landing aim points will be available at the time/location of landing. To increase the probability of finding a safe landing aim point, the frozen cost map is blended with a 2D Gaussian to find landing areas that are safe and have neighboring safe landing areas. This greatly increases the probability that the hopper will be able to find a suitable landing aim point at the time of landing.

Figure 36 shows the weighted cost map for Luna 23/24 using the MDM. This map is also normalized from 0 (highest probability of finding a safe landing aim point) to 1 (lowest probability of finding a safe landing aim point). This map correctly treats the large craters in the image as a large portion of the landing region that should be avoided and emphasizes the portions of the landing region that have many relatively safe landing areas close together.

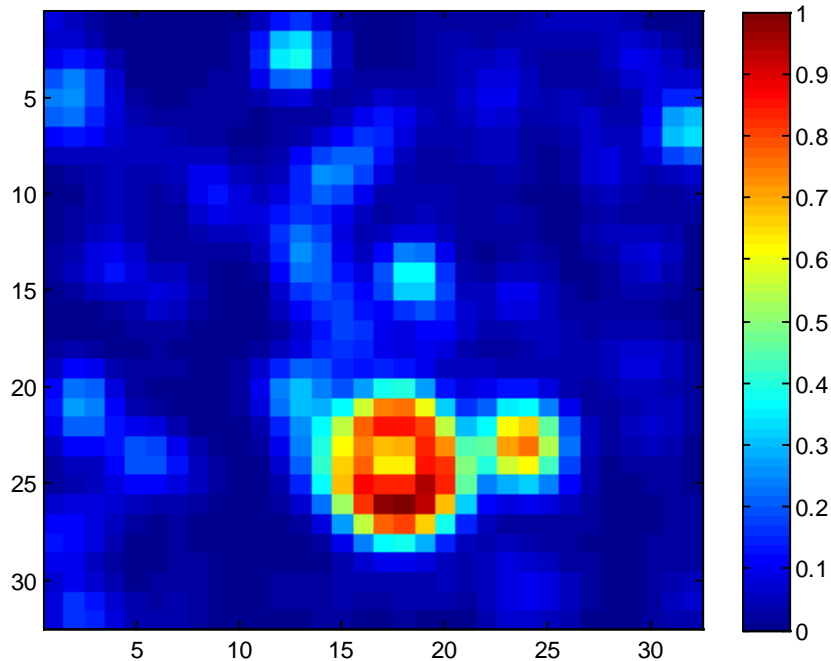


Figure 36 – Luna 23/24 MDM Weighted Cost Map

The frozen and weighted cost maps from the DEM-based method will be used to compare to the SDM weighted cost map to understand the SDM’s ability to select landing areas that are relatively safe and to also understand how that compares to the absolute safety of each landing area.

4.4.4 Size Density Method

As described, the SDM receives the rendered surface image from the surface and shading algorithm and uses that to produce a Weighted Cost Map which gives the relative costs between landing areas.

To study the SDM, lighting and view angles need to be controlled very precisely. There is not a comprehensive true image set of all lighting and view angles for any given planetary location (e.g., the Moon), so rendering is used to create representative planetary surfaces to study the SDM. Appendix A presents a detailed analysis of the comparison between the Luna 23/24 photograph and rendered image and justifies the use of rendered images for the remainder of the analysis in this thesis.

Figure 37 is a rendered image for the Luna23/24 region. This rendered image is created directly from the DEM. This image was created to directly compare against an actual photograph of the Luna 23/24 landing region given in Figure 19. The comparison results are presented in Appendix A and show that rendering is a good surrogate for studying the problem with controlled lighting and view angle conditions.



Figure 37 – Rendered image of the Luna 23/24 Landing Site

To detect features, the image histogram is created and high and low intensity thresholds are applied to create a binary image that outlines the features in the image. Figure 38 shows the bright features (left pane in white), dark features (middle pane in black), and combined features (right pane in black). The sun in this image is coming in from the bottom-left corner.

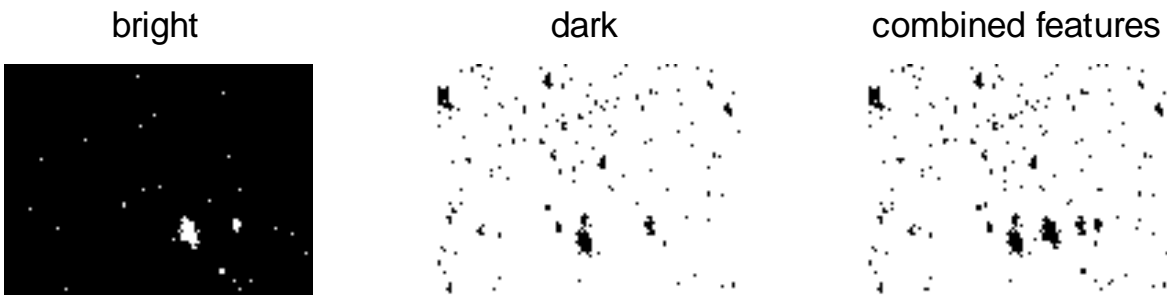


Figure 38 – Binary feature map (Luna 23/24 rendered image). Bright features are identified in white (left), dark features in black (middle), and combined to show all features in black (right).

As can be seen in Figure 38, the bright and dark features of the big craters capture the east/west extent of the crater well, but not the north/south extent. Since it is not known if the features are rocks or craters, hazards are not grown in any given direction. This is a limitation with the SDM but, since SDM is a gross, long range hazard detection method, precise size and location characterization of hazards is not critical. The weighted cost map smoothing is specifically developed to address this limitation by blending highly hazardous and highly safe regions to create the proper relative costs between safe and hazardous areas.

SDM uses the binary feature map to combine clustered features and bins them per landing area. The cost of each landing area is given by the formula in Equation 7. For the analysis shown here, the landing region is gridded into 32 x 32 landing areas (1024 total landing areas). The weighting between number and size (N) is equal to 1. The effect of N on the solution is studied further in the analysis presented later in the chapter.

Figure 39 shows the frozen cost map for the Luna 23/24 rendered image using the SDM given the parameters stated above. This landing area costs are normalized between 0 and 1. As can be seen in the frozen cost map, much of the cost is going towards the large features that identify the large craters in the image.

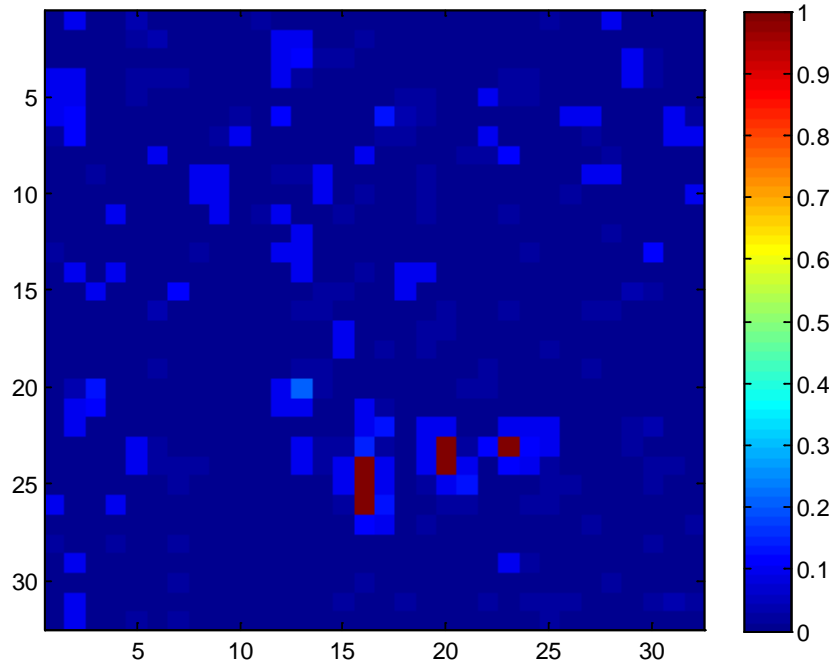


Figure 39 – Luna 23/24 SDM Frozen Cost Map (for rendered image)

A key difference between the cost map of the Size Density Method and Modified DEM Method is that hazards are not enlarged by the size of the lander footprint. The DEM-based hazard detection method detects hazards directly. These are enlarged by the radius of the lander footprint so as to assure that the lander does not overlap a hazard when landing. The SDM is concerned about relative safety and does not treat every feature as a hazard. Instead, it balances the amount and sizes of features in a given landing area to determine if one landing area has a better probability of being safer than another. To do this, the frozen cost map is blended with a 2D Gaussian to associate large portions of the landing area that are safe together, and large portions that are hazardous together. The Sparse Slope & Roughness Detection, described in the following chapter, does direct hazard detection within the landing area selected by SDM and is used to complement SDM to find safe landing aim points using an absolute hazard detection method.

Figure 40 shows the weighted cost map for the rendered image using the SDM. As can be seen, the area around the large craters is given the highest relative costs. Detailed analyses of both the relative and absolute costs given by SDM compared to MDM are given in the next section.

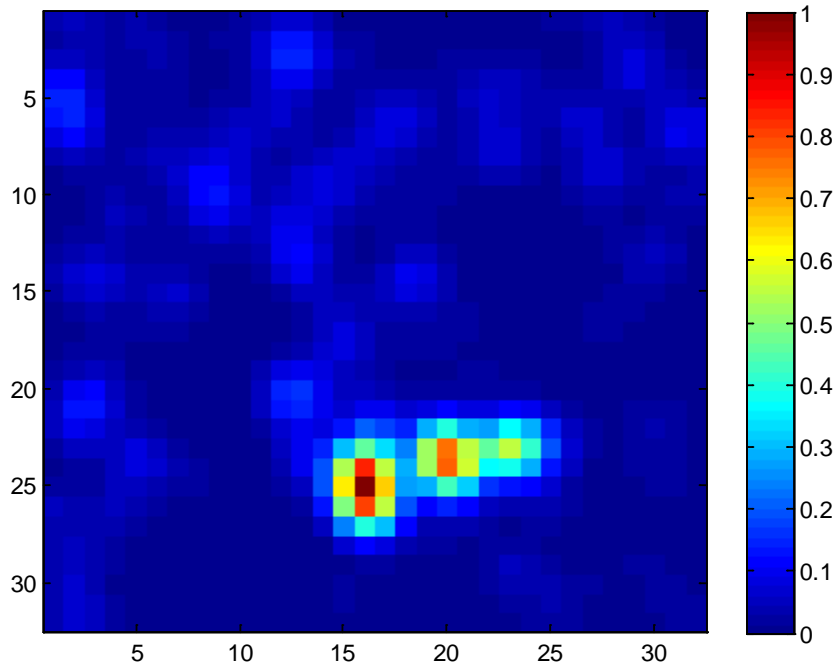


Figure 40 – Luna 23/24 SDM Weighted Cost Map (for rendered image)

4.4.5 MDM to SDM Relative Comparison

Figure 41 shows the weighted cost maps for the MDM (left) versus the Size Density Method (right). Figure 42 shows the absolute difference (left) and signed difference (right) between the maps. The absolute difference map overlays the two weighted cost maps and reports the absolute value of the difference between the maps on a scale from 0 (no difference) to 1 (completely different). The signed difference map overlays the two weighted cost maps and reports the signed difference between the maps. The color bar shows values from 0.5 (where MDM is reporting a higher cost) to -0.5 (where SDM is reporting a higher cost). A value of zero means there is no difference.

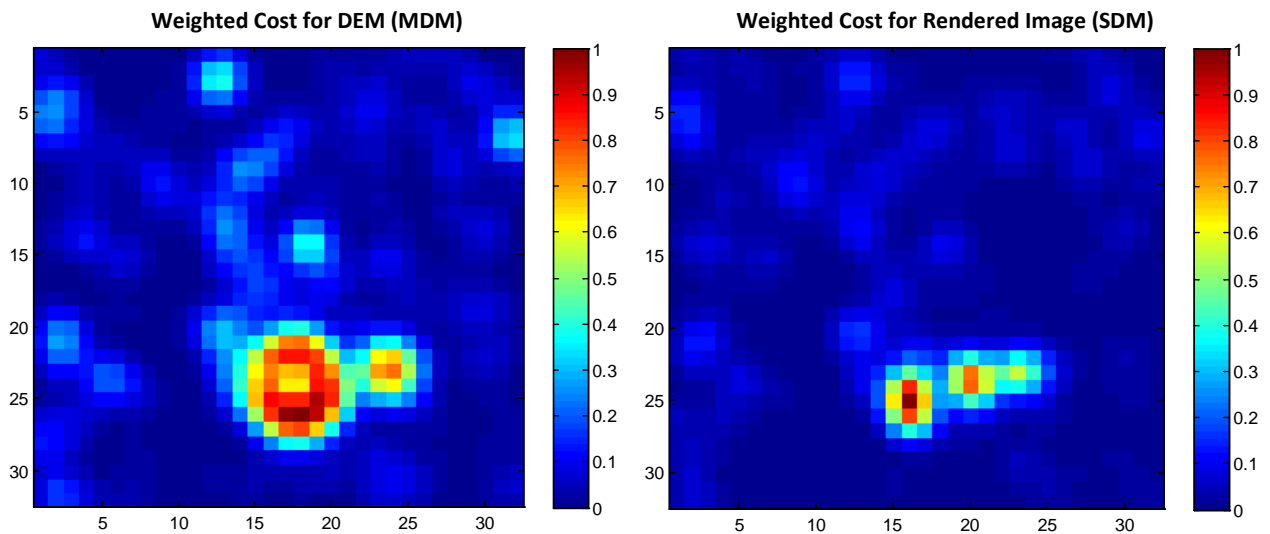


Figure 41 – MDM vs. SDM Weighted Cost Maps

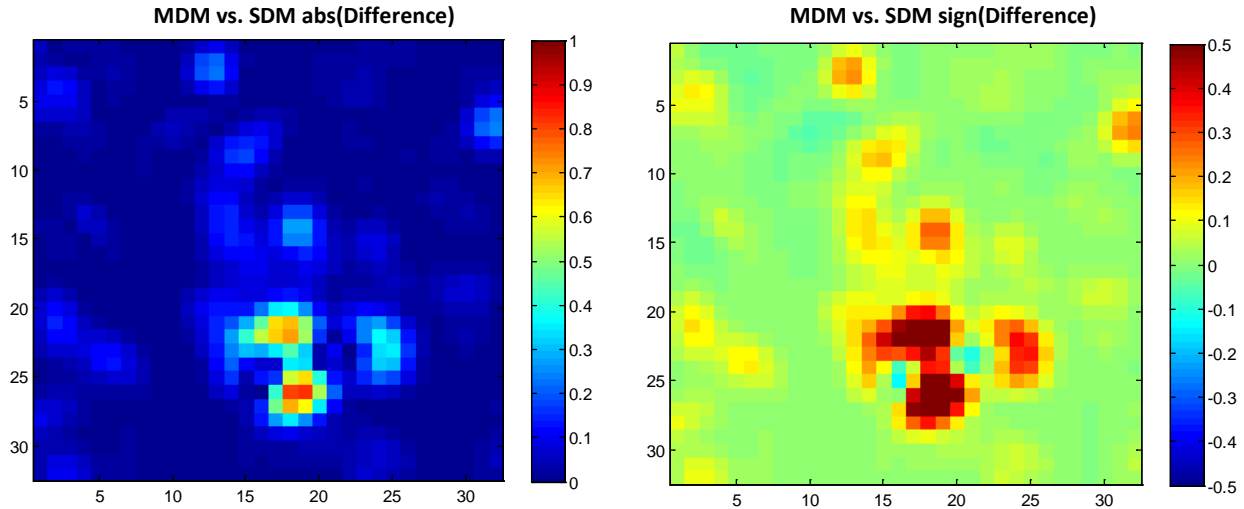


Figure 42 – MDM vs. SDM Weighted Cost Map differences

As can be seen, the areas of low and high costs are comparable. The area that has the most difference is around the large crater. The MDM method highlights a larger area as dangerous. But these are relative costs normalized within the construction method for each map. The 2D Gaussian and gridding parameters that have been used are the same for MDM and SDM, to allow for the most direct comparison. If the 2D Gaussian for SDM were allowed to be wider, the weighted cost map between the two methods would be closer. Since this is not known a-priori, the simulation maintains the same parameter sets for both MDM and SDM. To better understand the relative costs of landing areas, the landing area costs can be sorted and plotted against each other to understand the deviations on a LA-by-LA basis.

Figure 43 shows the weighted cost maps compared and displayed against each other, LA-by-LA. There are 1024 landing areas in the landing region. These landing areas are numbered and sorted by the SDM costs for the rendered image. The x-axis is then sorted by the landing area cost from the SDM. Thus, the blue dots in the plot are monotonically increasing. The MDM landing area costs are sorted by the SDM landing area costs and are represented by the red dots. Each red dot is the MDM landing area cost and is plotted against the same landing area location from SDM (in the y-axis). Thus, each LA location weighted cost is being compared directly between the two methods.

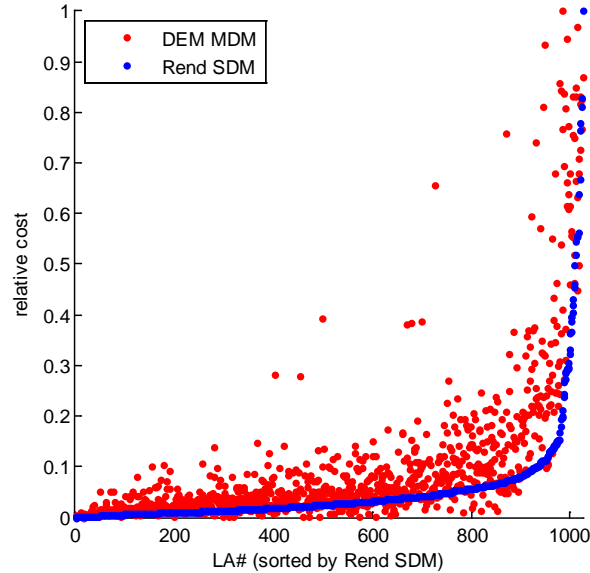


Figure 43 – Comparison of weighted cost maps for the SDM vs. MDM Luna 23/24 site

As can be seen from the plot, the relative costs track well. The MDM costs track very closely to the SDM relative cost. There are few outliers, and those that exist do not show up in the low cost values. Large outliers would be MDM costs (red dots) that appear in the upper-left hand portion of the plot (in the first 10% of landing areas, i.e.: LAs of 1 to 100). If any points appeared in the top-left of this plot, SDM would be reporting estimated safe landing areas that do not correspond to the same level of relative safety from MDM and SDM would be misrepresenting the relative safety of its chosen landing areas. These points do not appear which shows that the method performs well at giving safe landing areas a low cost and ranking them high in the selection process.

Furthermore, the high cost points align well between MDM and SDM. In the highest cost portion of the plot (LAs ranked above 900), there are very few points reported with the low relative costs from MDM. The fact that there are no points in the bottom-right corner of this plot shows that SDM is not reporting relatively low cost landing areas where MDM does. This shows that SDM performs well at reporting relatively dangerous sites as dangerous.

The portions of the comparison that are key are the lowest cost points and the highest cost points. Table 5 shows the mean, standard deviation, and maximum absolute errors for all of the data, the best 10% of points, and the worst 10% of the points. The mean and standard deviation are close throughout the data. The maximum absolute error is low for the best 10% (the landing locations that would be chosen) and the worst 10% (the landing locations that need to be avoided).

The best 10% have a low mean, standard deviation and maximum absolute error. The worst 10% have a worse mean and standard deviation. The maximum absolute error in this region comes from high cost points from the MDM method that aren't highlighted in the SDM. This is the same area as that of the big crater that is highlighted as hazardous in the MDM area. However, these areas are still ranked very low and have very little chance of being selected as a relatively safe landing area during the selection process.

Table 5 – Cost Comparison for SDM vs. MDM

	All Data	Best 10%	Worst 10%
Mean Abs Error	0.051	0.0022	0.25
Std Abs Error	0.077	0.00085	0.081
Max Abs Error	0.38	0.0036	0.38

It should be noted that the parameters used for generating the two weighted cost maps were the same (the same number and size of landing areas and the same 2D Gaussian blending parameters). The Gaussian filter applied to the SDM method can be scaled to increase the cost of the points in the area around large hazardous regions to improve the alignment between the two algorithms. This was not done so as to enable a more “apples-to-apples” comparison to be made between the two methods.

Comparing the relative costs between MDM and SDM shows that SDM has good performance. The following sections compare SDM to an absolute metric and analyze the computational speed of SDM versus MDM.

4.4.6 SDM Comparison to Absolute Safety Metric

To compare SDM to an absolute safety metric, MDM will be used in a different mode. Instead of applying a linear cost to slope and roughness hazards, the slope and roughness tolerances are used as an absolute cutoff. LAPs that have a slope or roughness above the threshold are considered hazardous, while those below the threshold are considered safe (more akin to the original method presented by Johnson et al (56)). For the LRO DEMs being used in this analysis, the pixel resolution is 2m. To keep this analysis simple, a VFDE diameter of 2m is also chosen, so that each pixel in the DEM corresponds to a LAP. Thus, there are approximately 4500 LAPs in each LA for the Luna 23/24 DEM.

Figure 44 shows the fraction of LAPs that are hazardous in each LA. This map is similar to, but not exactly the same as, the frozen cost map using the DEM method (Figure 35). This method sums up the number of safe and hazardous LAPs in each landing area and reports the fraction of hazardous LAPs within each landing area. The color bar represents the fraction of safe LAPs within each LA. This map is not blended, so there is no weight given to the absolute LA cost to address the safety of neighboring LAs.

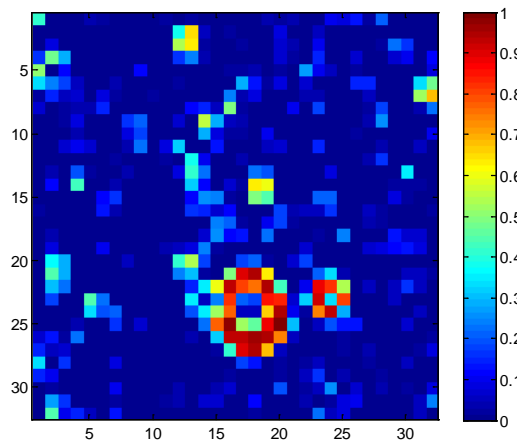


Figure 44 – Fraction of hazardous LAPs for Luna 23/24 Landing Areas

Figure 45 shows the relative costs reported by SDM compared against the absolute metric in Figure 44. SDM is concerned only with the relative costs between landing areas and has a 2D Gaussian applied to blend safe landing areas and hazardous landing areas together to highlight the safest and most hazardous regions in a landing region.

Nonetheless, the comparison does well in showing how, for this DEM, the blended SDM weighted cost map aligns with the absolute costs using the DEM-based hazard detection method. Since the absolute metric is not blended, there are more outliers, especially in the bottom-right portion of the plot. This implies that SDM is being overly conservative and is reporting relatively unsafe landing areas when they are in fact safe. The points that show up in this region reflect the bottom of the craters (which in an absolute sense are safe). In a blended solution, these points would normally be discounted, but they are technically feasible locations for the hopper to land. There are still no points in the upper-left, which shows SDM performs well at ranking safe landing areas high in the selection process.

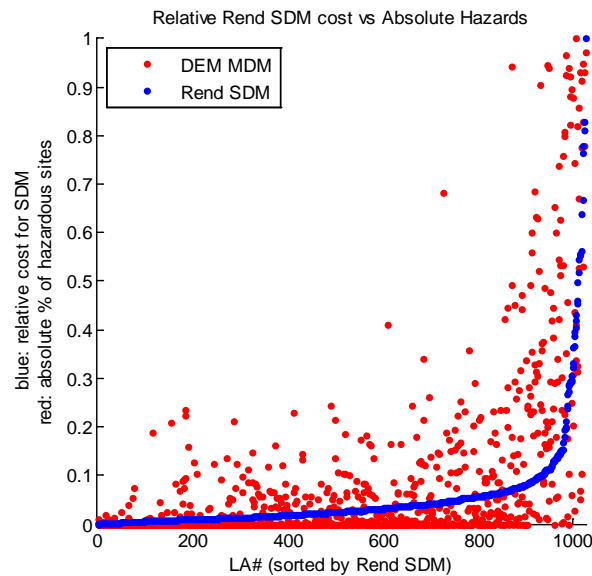


Figure 45 – SDM landing area rankings vs. absolute cost

The Size Density Method matches well in performance to the DEM-based technique, but the main strength of this algorithm comes in improved speed and the use at lower path angles. Timing comparisons between these methods will be analyzed in the next section. The effects of the Sun and viewing angles will be analyzed later in the chapter.

A known deficiency of the Size Density Method is the detection of hazardous slopes. However, the use of both bright and dark features helps identify slopes that are high relative to the rest of the slopes in the landing region. With the current LRO and Mars orbiter data being collected for the Moon and Mars, many large-scale slopes will be identified prior to flight for those planetary bodies. Kumar (95) discusses a system for using altimeter range data to determine the relative slope beneath a landing vehicle and ultimately to detect the slope at the landing aim point. This technique will be expanded upon to provide landing hazard detection for a traversing hopper in Chapter 5.

Combining the ability to assess relative safe landing areas from afar (Size Density Method) with a slope and roughness detection near the end of the landing (described in Chapter 5) creates a powerful operational concept for safe landings from long ranges and shallow path angles using relatively small and low cost sensor solutions. This gives the safety and precision provided by the DEM-based technique, while providing quick solutions at long range and shallow path angles.

4.4.7 Timing and Performance Comparison between MDM and SDM

The algorithms were run on an Intel Pentium Core i5 2.6 GHz processor with 4GB of RAM as part of the same simulation runs. The times for each simulation were recorded using Matlab’s tic toc functionality. Table 6 shows the timing comparison between the methods. Table 6 also shows the dimensions of the map and imaged used. The rendered image used for the SDM has nearly 50% more pixels than the DEM. To give a better comparison between the methods the runtime-per-pixel is used. The SDM is ~30 times faster than the DEM method on a per-pixel processing basis.

The timing for MDM assumes a DEM already exists in memory. MDM is benchmarked from the start of processing to generation of the weighted cost map. The timing for SDM assumes an image has been taken and is in memory. SDM is benchmarked from start of image processing to generation of the weighted cost map. The timing for SDM also includes the time required to take the intensity histogram, create the intensity thresholds, and apply them to the image to create a binary feature map. On a dedicated processor, or a specialized image processor, the SDM algorithm would run even faster. Methods to improve MDM on special purpose processors are also being researched, but are not accounted for in MDM used in this thesis.

Table 6 – Timing analysis between DEM-based and Size Density Methods.

	MDM on DEM	SDM on Rend Image
Dimensions	941x1231	1133x1483
Total Pixels	1158371	1680239
WC Map Pixels	32x32	32x32
Runtime (s)	48.9	2.3
Runtime/pixel (μs)	42.2	1.4

4.4.8 SDM Cost Function

The value **N** in Equation 7 allows mission planners to weight number of hazards versus size of hazards. In the analysis above, this value was set to 1 (a balance in the cost between size and number). If **N** is greater than 1, then feature size is weighted higher, if **N** is less than 1, then feature density is weighted higher.

Figure 46 shows the SDM run for 3 values of N: 0.5 (number of features weighted more), 1 (even weighting), and 1.5 (large features weighted more). Each column shows the frozen cost map (top row), weighted cost map (middle row), and relative comparison to the MDM method (bottom row).

As can be seen, each value of N does a good job of identifying the large craters in the bottom of the image. For $N = 0.5$, there are many more hazardous areas and the relative costs to MDM make SDM overly conservative. The converse is true for $N = 1.5$, where only the large features are accentuated.

Regardless, the major features are still tracked well and the relative cost trends correspond well to MDM. The weighting value of N has been built in to SDM for mission planners. In the remainder of the thesis analysis, the value is set to 1. Future work may study the optimization of N for different environment conditions.

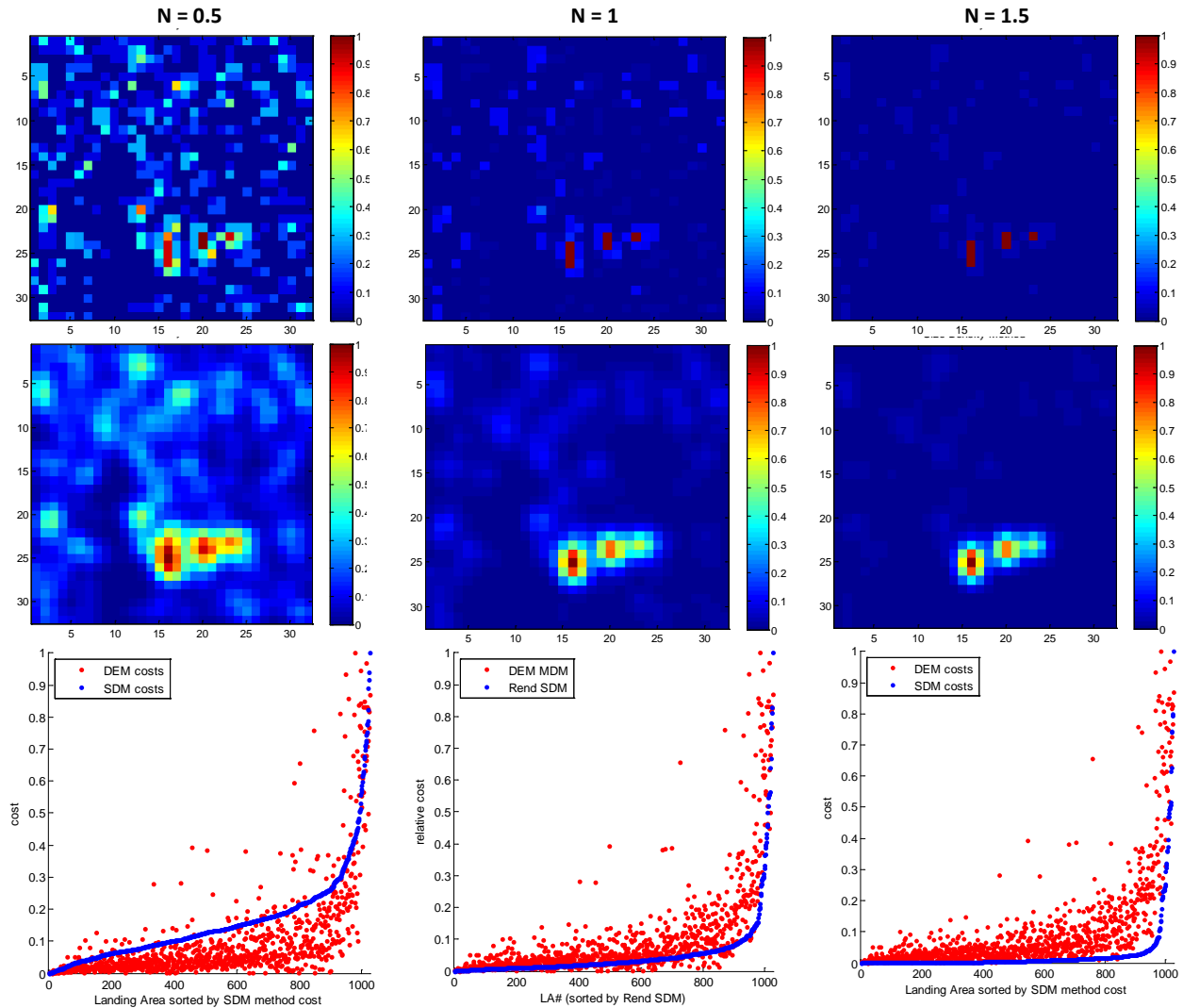


Figure 46 – Varying values of N for SDM

4.4.9 Varying Viewing and Sun Angles

To further study the Size Density Method, several analyses were undertaken to understand the performance of the method under varying view angle and lighting conditions. Table 7 shows the parameter tradespace used to study view and sun angle effects on the SDM.

Table 7 – View and Sun Angle Tradespace

Sun Azimuth Angle (degrees)	Sun Elevation Angle from horizon (degrees)	Viewing Elevation Angle (degrees)
0 (sun from right)	5	10
90 (sun at back)	15	20
180 (sun from left)	25	30
270 (sun in face)	35	90
	45	
	55	

Figure 47 shows a plot of all the points in the tradespace plotted with 95% confidence bounds (2σ standard deviation with dependent sampling). Overall, there are no major outliers in the upper-left corner. The 2σ standard deviation over all points is 0.1 on the relative cost scale. The following sections will isolate the sun elevation, sun azimuth, and view angles and report the bias of the mean and magnitude of the standard deviation for each slice through the data.

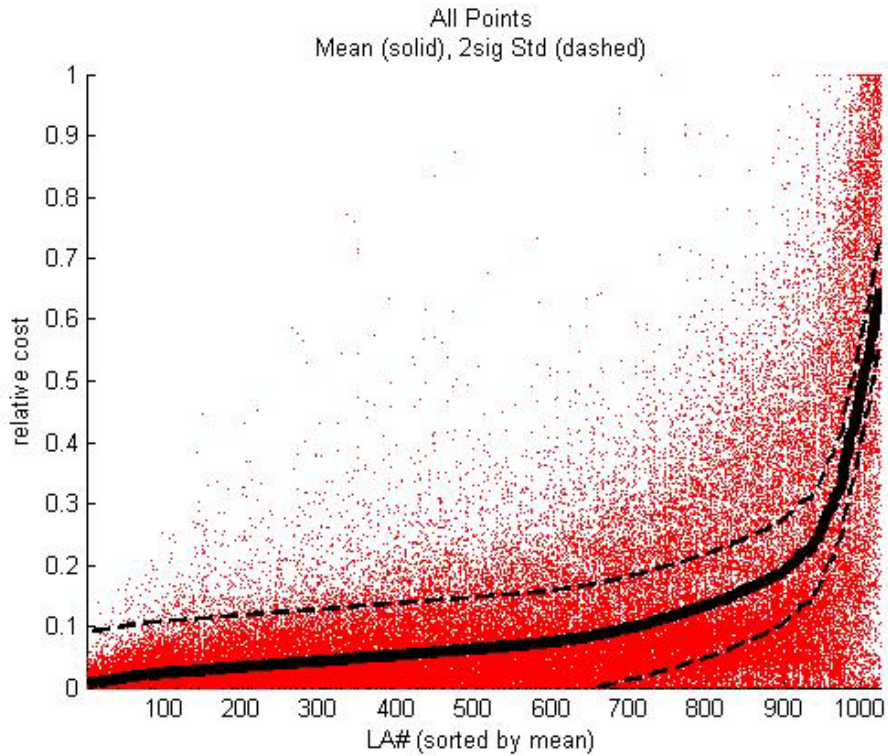


Figure 47 – Landing area comparison for all sun and view angles

4.4.9.1 Sun Elevation Angle

To illustrate the changes in sun elevation angle, Figure 48 shows a slice of the tradespace with varying sun elevation angle. The view elevation angle is 90 degrees (top-down) and the sun azimuth angle is 0 degrees (sun from the right) for these illustrations.

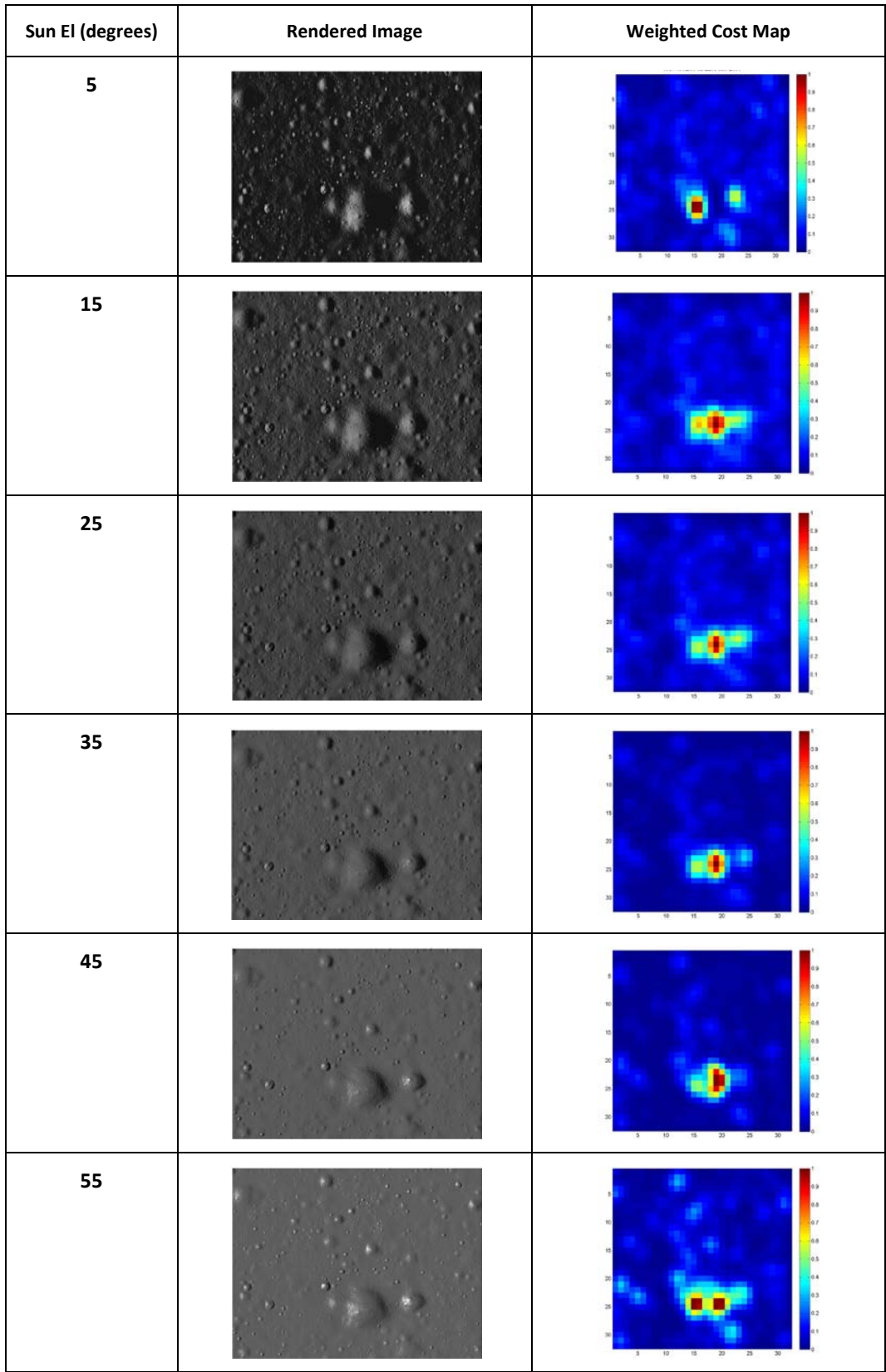


Figure 48 – Sun elevation angle images and weighted cost maps

As can be seen in the figure, there is commonality in the solutions between 15 and 45 degrees. To understand this further, Figure 49 shows all the points in the tradespace plotted with different sun elevation angles differentiated by color:

- 5 deg = magenta
- 15 deg = blue
- 25 deg = cyan
- 35 deg = green
- 45 deg = yellow
- 55 deg = red

The magenta points (5 degree sun elevation angle) carry the majority of the outliers in the solution. SDM does not perform well here because the images taken with a sun elevation angle of 5 degrees tend to have a majority of the surface in shadow, making features hard to discern.

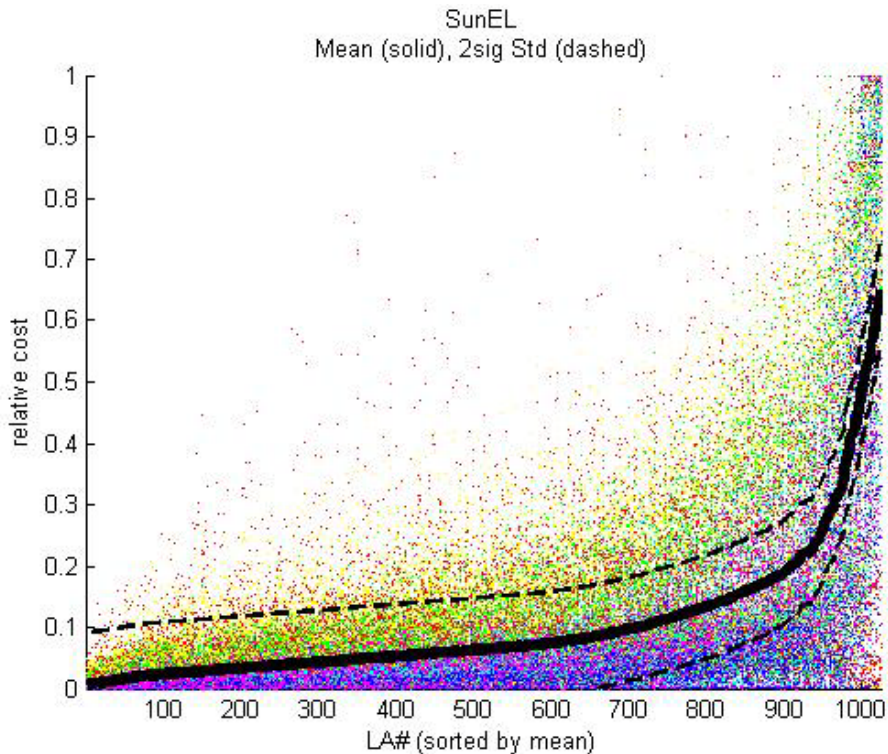


Figure 49 – Landing area comparison for varying sun elevation angles

Figure 50 shows the mean and standard deviation (STD) between all points in the tradespace and different slices of the sun elevation angle through that tradespace. The points with sun elevation of 5 degrees have a large dispersion, while all the other solutions have relatively low standard deviations.

As sun elevation angle increases, the solutions have better standard deviations and become more conservative (curves move lower) until 55 degrees, where the standard deviation begins to grow and the curve begins to move up. Solutions between 15 and 45 degrees provide the most consistent results.

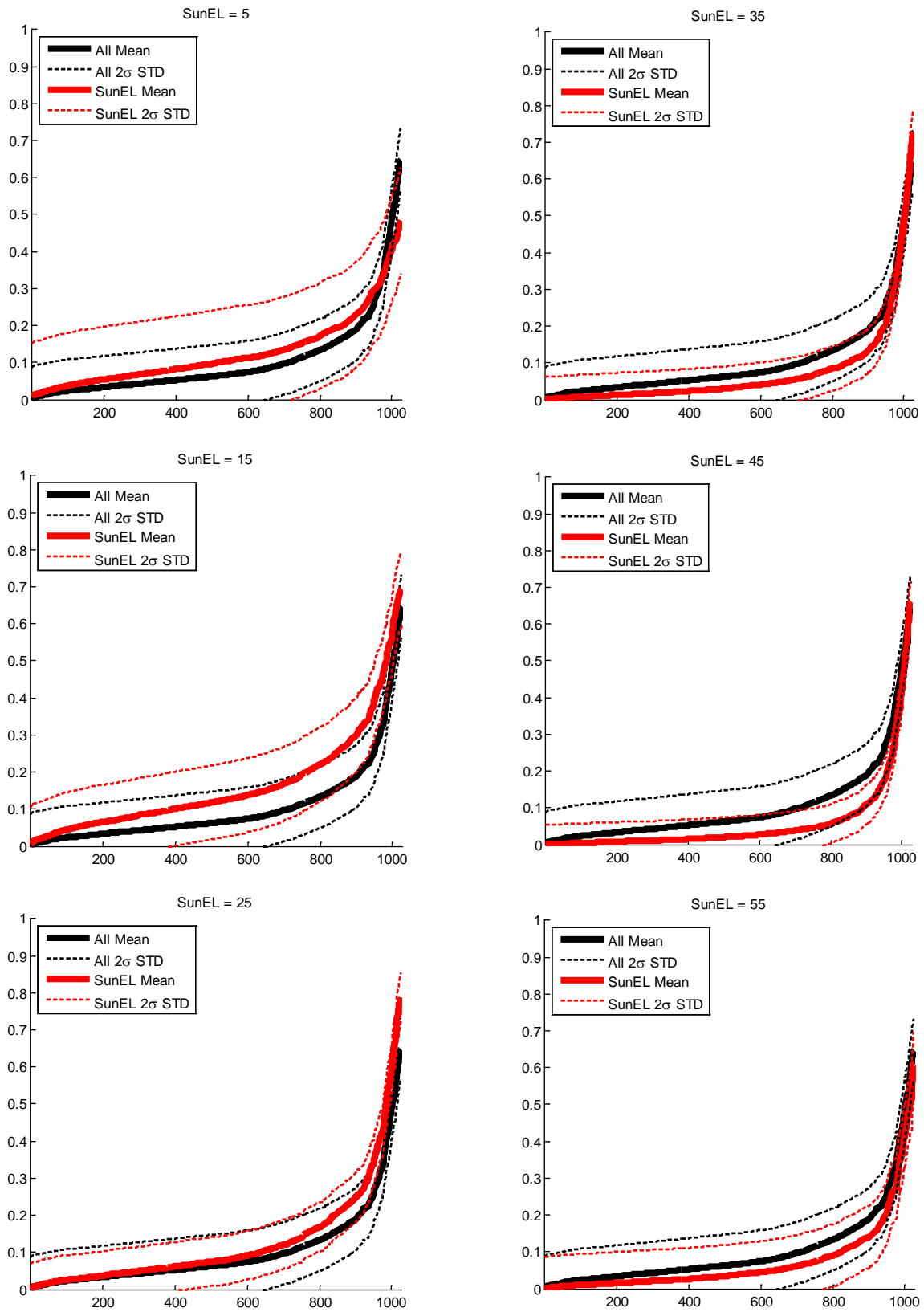


Figure 50 – Comparison of SunEL mean and STD to mean and STD of all points

The Size Density Method works best in sun elevation angles between 15 and 45 degrees. Above 45 degrees, many rock shadows shrink or nearly disappear, exposing only bright features. Above 45 degrees, crater shadows begin to diminish, but can persist up to very high elevation angles. Below 10 degrees, crater shadows are very well defined, but the limbs of craters, hills on the horizon and large boulders flood the scene with shadows. A very good illustration of this can be seen from Kaguya imagery during descent to impact with the lunar surface presented in Brady & Paschall (52)(115). At the North Pole of the Moon, the sun elevation angles are very low and it can be seen that the landscape becomes flooded with shadows.

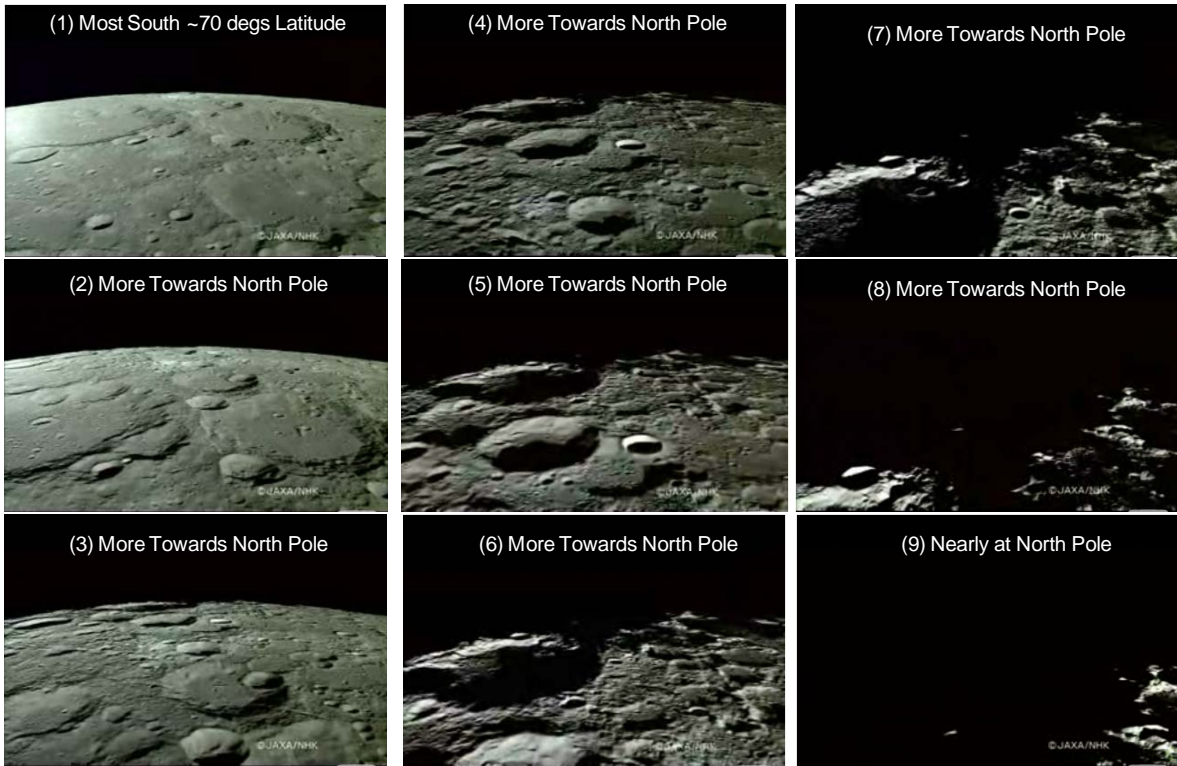


Figure 51 – Kaguya Descent Imagery

4.4.9.2 Sun Azimuth Angles

To illustrate the changes in sun azimuth angle, Figure 52 shows a slice of the tradespace with varying sun azimuth angles. The view elevation angle is 30 degrees and the sun elevation angle is 25 degrees for these illustrations.

When sunlight is coming in from the side, features are detected well because both the lit and dark features portray the extent of large hazards. When the sun elevation is close to the view elevation, which is the case here, the large features are still captured fairly well. When the sun is in front, the shadows are long and nearly the full extent of them is viewed, but there are not many bright features. When the sun is in the back, the slopes are bright and many of the big craters stand out. For the sun-in-back case, there is a coupling between the view elevation and sun elevation angle. If the sun elevation is below the view elevation, then both shadows and bright features are captured. If the sun elevation is above the view elevation, then only bright features persist.


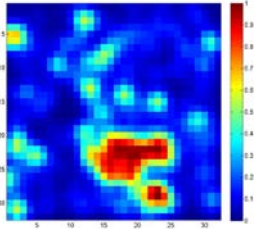
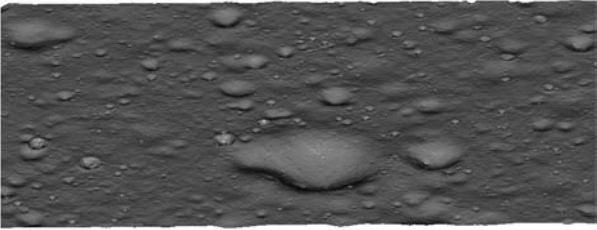
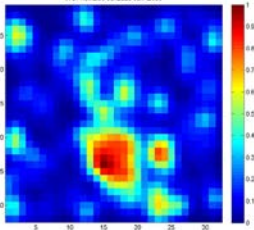
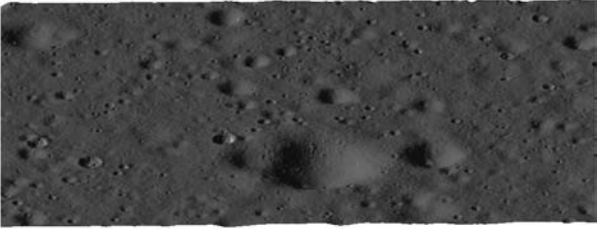
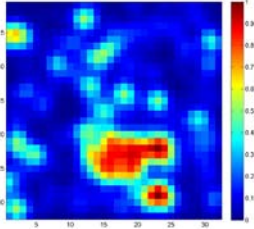
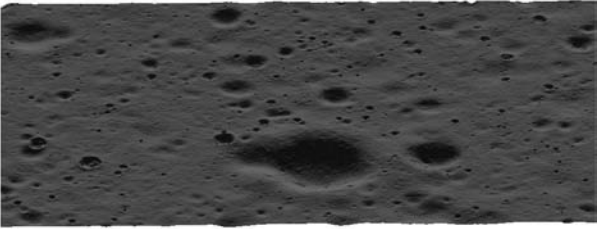
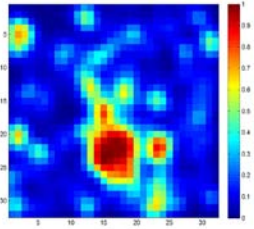
Sun Az (degrees)	Rendered Image	Weighted Cost Map
0 (sun from right)		
90 (sun in back)		
180 (sun from left)		
270 (sun from ahead)		

Figure 52 – Sun azimuth angle images and weighted cost maps

To understand this further, Figure 53 shows all the points plotted with different sun azimuth angles differentiated by color:

- 0 deg (sun from right) = blue
- 90 deg (sun in back) = green
- 180 deg (sun from left) = yellow
- 270 deg (sun from ahead) = red

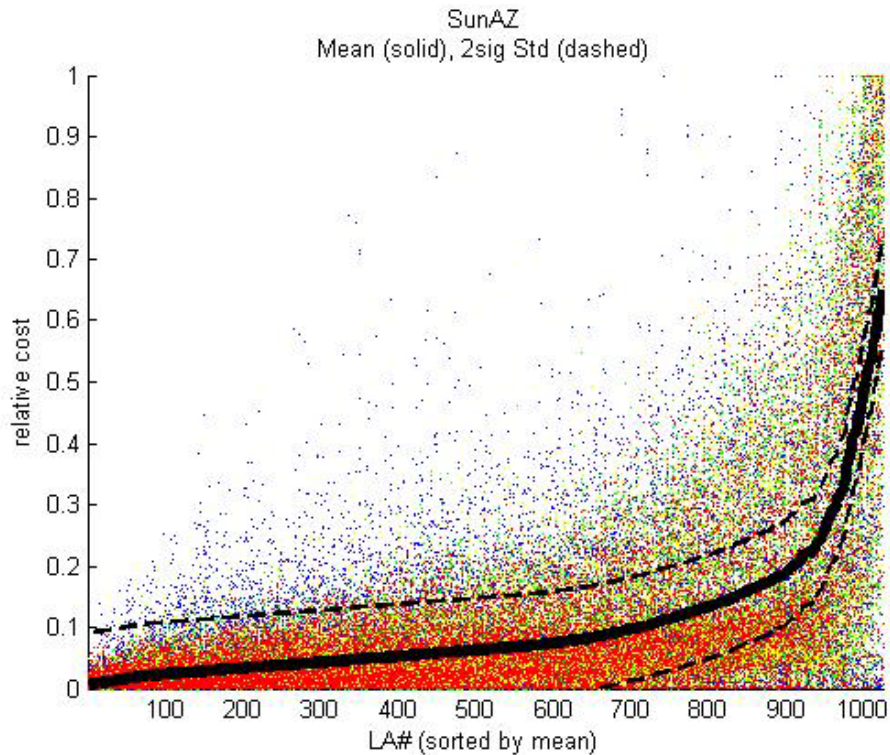


Figure 53 – Landing area comparison for varying sun azimuth angles

Figure 54 shows the mean and standard deviation (STD) between all points in the tradespace and different slices of the sun azimuth through that tradespace. The mean of all four sun azimuth angles corresponds to the mean of the overall population. There is no bias between any of the sun azimuth angles in the formulation of the solutions.

When the sun is in front (sun azimuth = 270 degrees), the standard deviation of the solutions are noticeably greater. This shows that the algorithm performs slightly worse when the sun is in front. This can be attributed to dark features being accentuated, while bright features are not. Brightening of the surface occurs when the sun and view angle vector are aligned but, in the sun-in-front case, that is a rarity. The benefit of having features at both ends of the intensity spectrum is not present in this case.

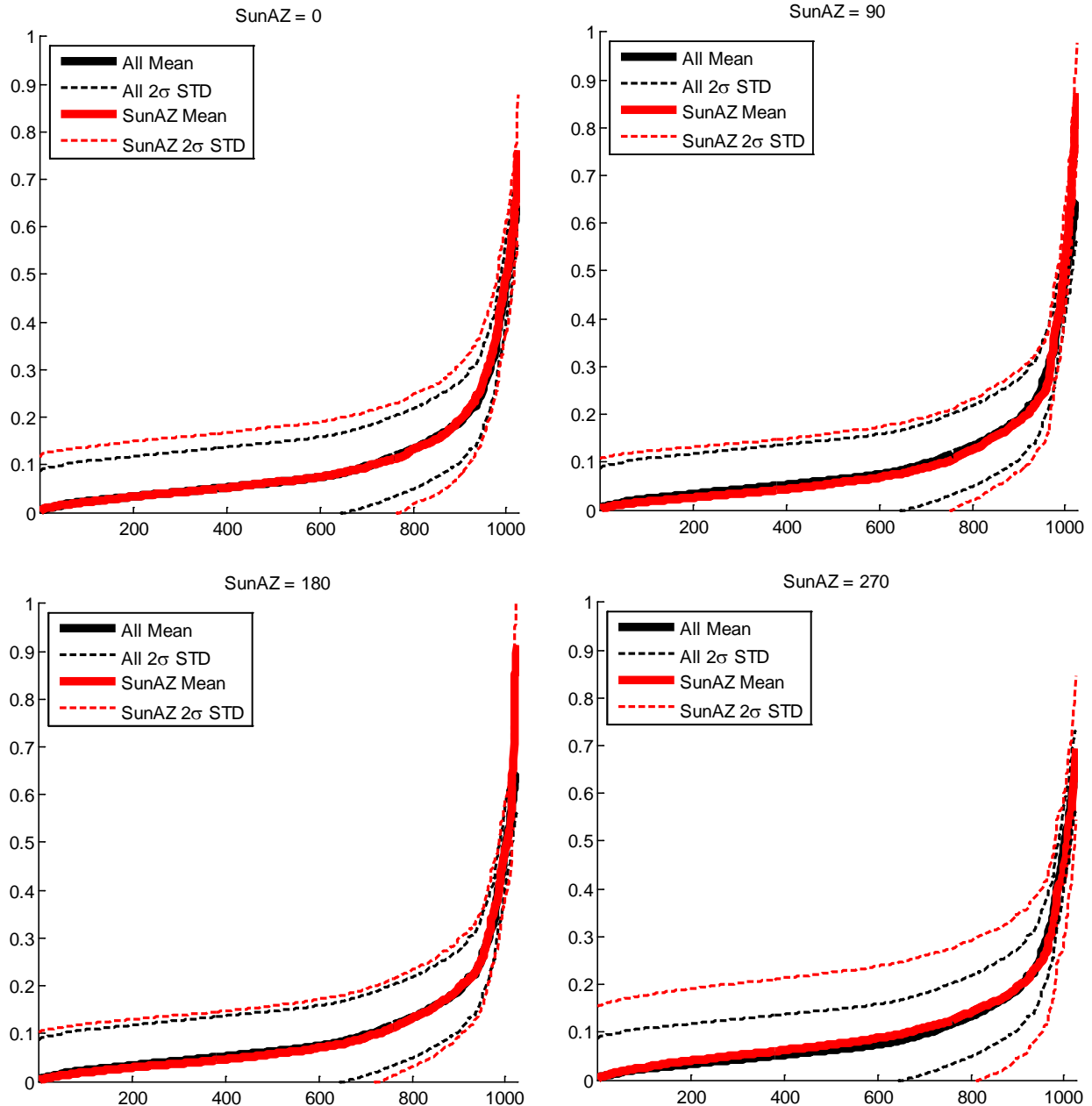


Figure 54 – Comparison of SunAZ mean and STD to mean and STD of all points

4.4.9.3 View Elevation Angles

The Size Density technique of gridding the landing area can be extrapolated to shallow path angles. This is a powerful tool for doing traverse landing area selection at low altitude hover-hop trajectories. An example is given below to help better illustrate the effectiveness of this technique at varying path angles.

To illustrate the changes in view elevation angle, Figure 55 shows a slice of the tradespace with varying view elevation angles. The sun azimuth angle is 0 degrees and the sun elevation angle is 25 degrees for these illustrations.


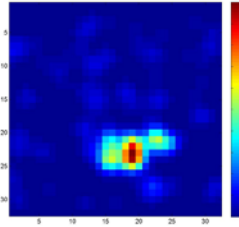

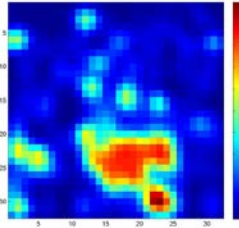

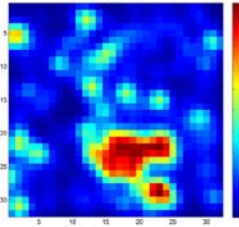
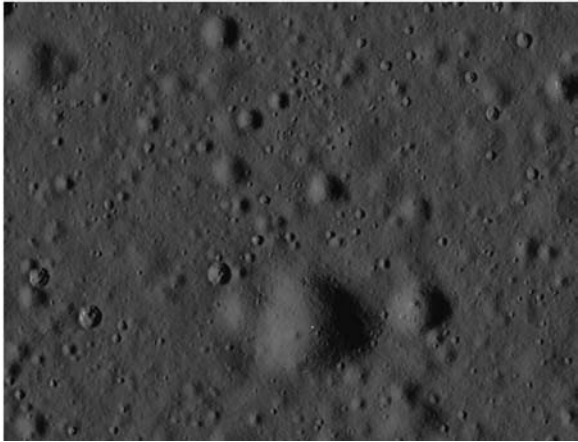
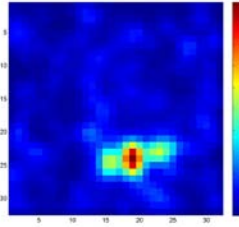
View EL (degrees)	Rendered Image	Weighted Cost Map
10		
20		
30		
90 (overhead)		

Figure 55 – View Elevation angle images and weighted cost maps

To understand this further, Figure 56 shows all the points plotted with different view elevation angles differentiated by color:

- 10 deg = red
- 20 deg = yellow
- 30 deg = green
- 90 deg = blue

The SDM does fairly well at low path angles. The 10 degree and 90 degree solutions accentuate the large craters more. The 20 and 30 degree view elevations are close to the sun elevation angle, which helps to accentuate shadows and bright areas. As the view elevation angle is lowered, there are no major outliers found in the upper-left corner of the plot. This demonstrates that the relatively safe sites are conserved and provides an excellent method for landing area selection for low-altitude traversing hoppers.

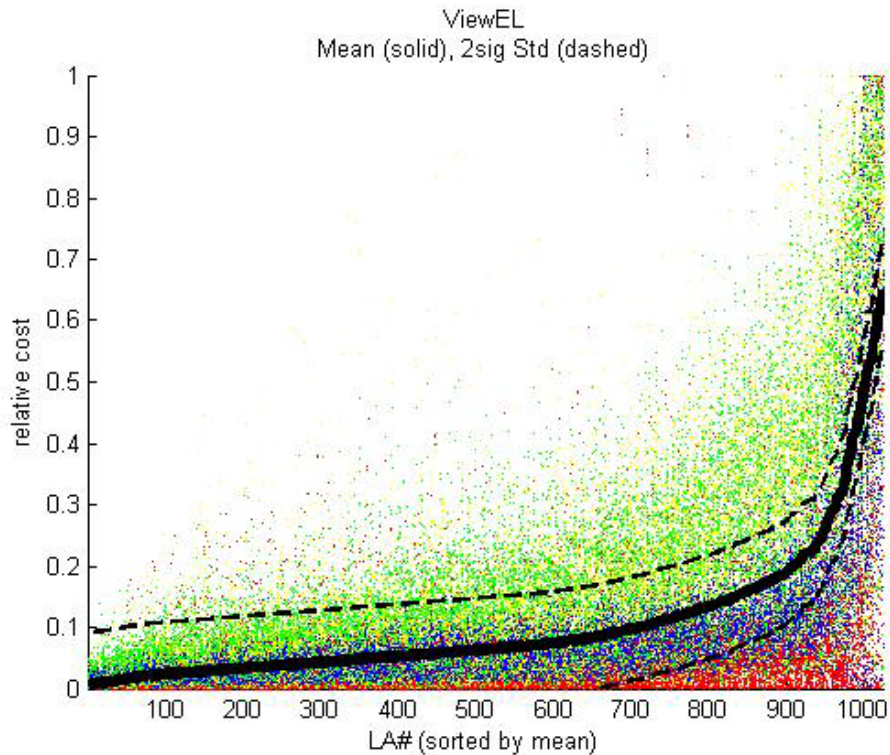


Figure 56 – Landing area comparison for varying view elevation angles

Figure 57 shows the mean and standard deviation (STD) between all points in the tradespace and different slices of the view elevation angles through that tradespace. All the solutions have comparable standard deviations.

At 10 degrees (very low path angle) view elevation angle, the solution is conservative. This is also the case at 90 degrees (straight above). The 10 degree view angle picks up on many of the large features and does well in capturing and isolating those areas. The 90 degree view angle sees all landing areas with the same perspective, and thus has the best chance of making the most unbiased detections.

The 20 and 30 degree solutions show higher costs, especially in the more hazardous region of the map. At the 20 and 30 degree view elevation angles, the features are more pronounced, as can be seen in the weighted cost maps in Figure 55. These are the solutions were the SDM weighted cost map shows heavier costs than MDM.

All solutions are still good in the low and high cost regions of the map, which shows that SDM is capable of detecting large safe and large hazardous regions at shallow path angles. This is a powerful result for SDM and shows that it can be used for hopper traverse landing area selection.

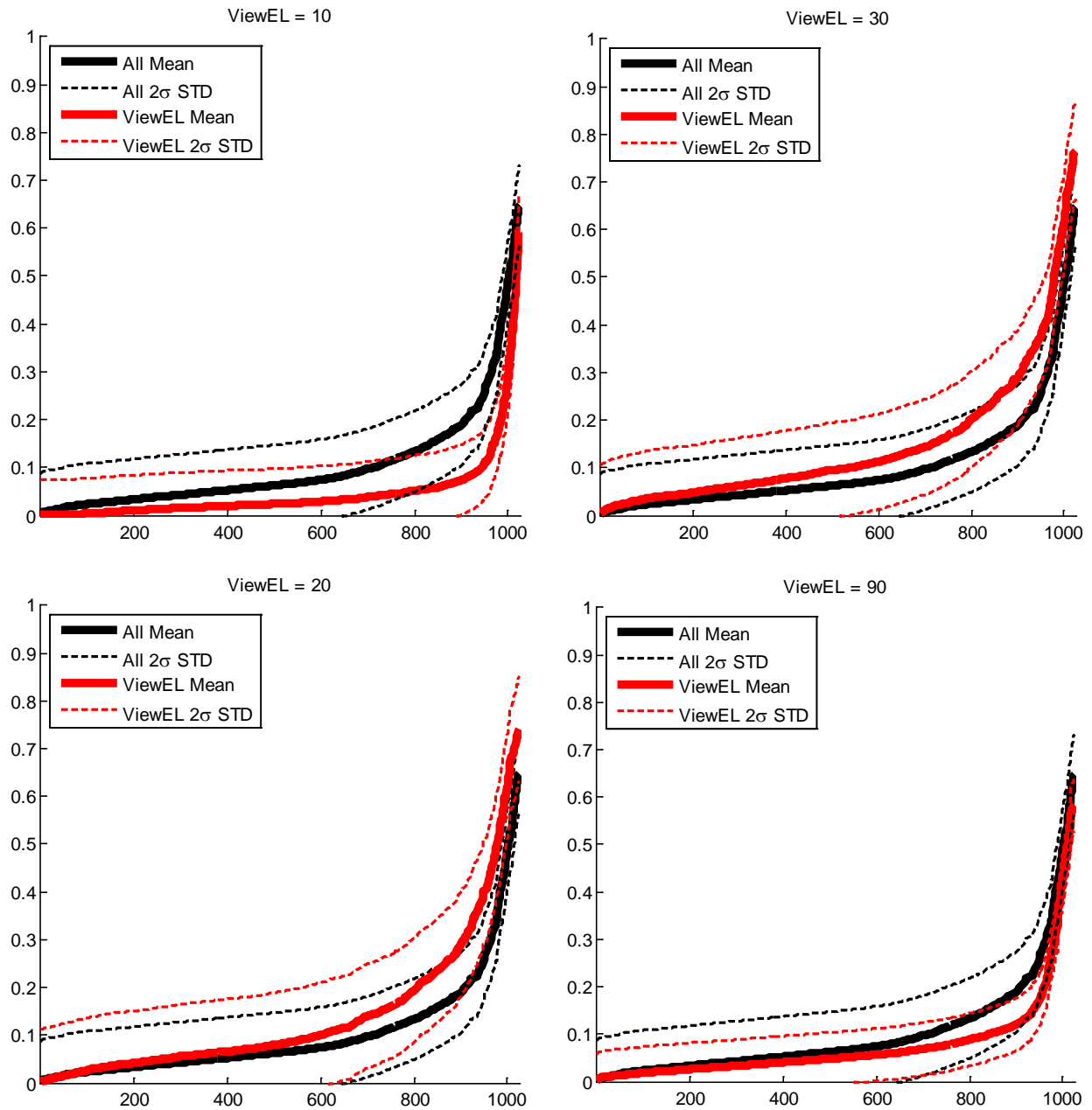


Figure 57 – Comparison of ViewEL mean and STD to mean and STD of all points

4.4.10 Analysis Discussion

4.4.10.1 Sun Azimuth, Sun Elevation, and View Elevation Discussion

The Size Density Method does not use the sun direction to determine the precise location of the hazards. Without discerning structure from the shadows (116), it is difficult to tell if the shadow is being cast from a crater or from a rock. Rocks will cast shadows away from the sun, while craters will cast

shadows into the crater. Figure 58 shows a simple illustration of the expected shadowing caused by a rock versus a crater.

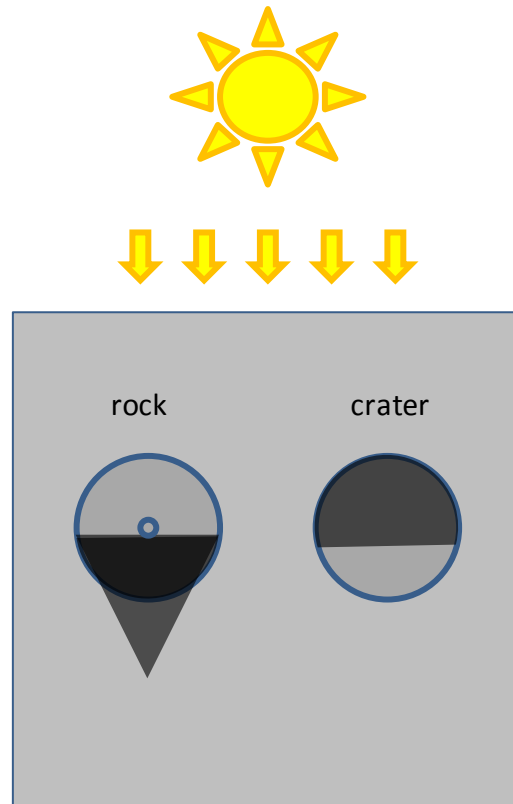


Figure 58 – Illustration of shadows cast by rocks vs. craters

Knowing the sun angle does help constrain the hazard location along the direction of the sun azimuth angle, but this was not used in the method. Since the Size Density Method is used for landing area selection, and not precise hazard detection, the method does not include the additional computations to pick out hazards directly from the shadows.

It is worth noting that even if hazards were separated from their shadows, and solutions were shifted to center of the hazard and not the shadow itself, it would still be undesirable for the vehicle to land in a shadowed area. What lies within a shadow is unknown and the cold thermal conditions may affect the vehicle negatively. Treating the shadows as hazards themselves is a conservative approach. Since each landing area being evaluated will be experiencing the same sun azimuth and elevation, and thus the same shadow angles, the relative safety between landing areas should be the same if only shadows are used or if hazards are directly discerned from their shadows.

These analyses showed the performance and limitations of the Size Density Method as functions of lighting and view angle conditions. The Size Density Method is limited by lighting conditions, but offers consistent performance over varying view angles.

For a hover hop or ballistic hop trajectory, the direction and altitude of traverse can be adjusted to ensure that the desired sun angles are created for creating the best results for performing landing area selection from one hop location to another. The algorithm performs best at sun elevation angles between 15 and 45 degrees. The SDM was able to work at all azimuth and view elevation angles.

The speed of execution and ability of the Size Density Method to work at long ranges and low path angles is a powerful motivation for using this method. This allows any landing or hopping vehicle to constantly assess the landing areas ahead and refine the landing area selection upon approach to the desired range or target condition for landing. Coupled with the Sparse Slope & Roughness Detection Method described in the following chapter, a strong operational concept exists to enable safe hopping using low-cost, low-mass, high-speed solutions.

4.4.10.2 Refinement of landing area throughout approach

During a dynamic flight, where attitude changes are expected, the gridding formulation given in Figure 22 will need to be used to estimate the center of the image and correlate one image to another. The range to the landing area and the percentage of sky in an image may change, but as long as the relative position of the center of the FOV can be estimated from image to image, the Size Density Method can continue to provide results for the desired landing area.

As the hopper approaches the landing area, the algorithm highlights landing area locations near the horizon and, as new landing areas come into view over the horizon, the selection of landing areas may shift from one location to another. To optimize fuel usage, the algorithm has to maintain a proper heading and not switch the landing area location too often or too near the end of the flight (possibly causing an unstable landing).

To limit the constant switching of landing areas (de-bouncing (117)), the algorithm should add a cost function with a threshold based on relative cost to change locations:

- This still allows further locations near the horizon to be considered along the full width of the FOV because making a small heading change costs relatively low fuel.
- Locations in the foreground that are off to the side will require more aggressive maneuvers and will be ruled out.

At some point, if a safe landing area becomes relatively unsafe and another location ensures much safer landing, then the landing area selection will switch based on the cost tradeoff between safety and fuel consumption. This formulation has been saved for future work.

4.5 Chapter 4 Summary

This chapter described the Size Density Method for landing area selection. The method uses feature size and number to compute relative safety upon approach to a landing area. The algorithm is limited by lighting conditions, but under the proper lighting conditions has a comparable performance to higher fidelity methods. The main advantages of the technique are that it gives comparable performance with a faster algorithm and that it has the ability to continue detections at low path angles and over long ranges (key for low flying, rapid traverse vehicles, such as hoppers).

The method was validated against a higher fidelity DEM-based Hazard Detection method for both relative and absolute costs. It was shown that the Size Density Method has comparable performance to the DEM-based method, but can be run at much faster speeds.

Lighting conditions and view angles were used to study the performance envelope of the Size Density Method. The Size Density Method works for overhead, as well as shallow path angles to the landing zone. The method uses passive lighting techniques and is not restricted in range, but it is restricted by the sun elevation angle at the landing region.

This technique, coupled with Sparse Slope & Roughness Detection (described in following chapter), is a powerful tool for autonomously perceiving and acting on hazard information upon approach to a landing area.

5 Landing Aim Point Selection

As a complement to the Size Density Method, active sensing of the surface can be used to precisely measure the slope and roughness hazards on a planetary surface near landing. While the Size Density Method is capable of statistically determining safety at shallow path angles and from long distances, it is unable to detect slope and precisely detect roughness.

A short range LIDAR that scans out in front of the hopper during traverse provides active sensing of the surface for relatively low mass and power. Current LIDAR sensors available for space exploration are precise (97), but increase in mass and power as a function of range.

Table 8 – Laser Range Sensors. Altimeters flown on space missions are shown in gray: MOLA(118)(119), LOLA (120)(121), MLA (122)(123), NLR (124). Examples of two terrestrial lasers are given in brown: Velodyne HDL-32E (125) and Acuity 3000 (126).

	MOLA	LOLA	MLA	NLR	Velodyne HDL-32E	Acuity 3000
Mass (kg)	25.85	15.3	7.4	5	2	0.85
Power (average, W)	34.2	39.6	16.4	16.5	12	12
Rate (Hz)	10	28	8	8	10	100
Range (km)	786	70	1500	50	0.07	0.2
Range precision (cm)	37.5	10	30	31	2	2

Small sensors are commercially available with much shorter range for lower mass and power. It is conceivable that terrestrial sensor technology and specifications can be developed for space-based applications. These sensors still provide enough range and range precision to be able to detect slope and roughness on the order of the size of the lander footprint for hopper traverse missions.

This chapter describes the methodology for detecting slope and roughness that can be used to complement the Size Density Method, near the end of the hopper traverse, thus improving landing safety. The flow diagram for detecting slope and roughness using a short-range LIDAR is outlined in Figure 59.

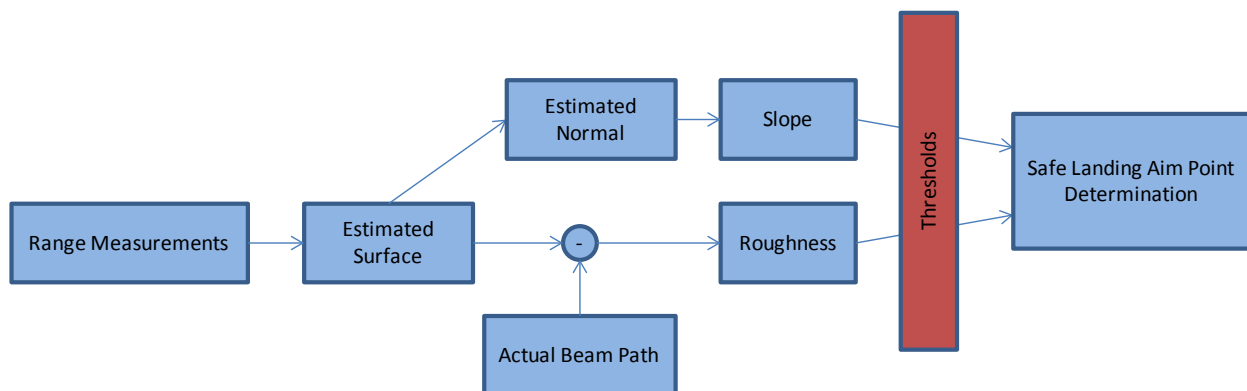


Figure 59 – Slope & Roughness Flow Diagram

As the hopper traverses over the planetary surface, the onboard navigation filter will have an estimate of the hopper’s surface relative altitude (based on an expected smooth, mean surface), attitude, and velocity. The range measurements to the surface compared against the current navigation filter state

estimate can be used to understand the surface relative slope with respect to the vehicle and the gravity vector. Deviations, or altitude differences, in the measurement can be used to estimate the roughness of the surface. Roughness denotes the statistical deviations, or “bumpiness,” of the surface. The lander will be designed to withstand a certain size of hazard, and understanding and measuring the roughness of the surface can be used to pick an area that is within the expected roughness threshold of the landing legs of the vehicle.

The range sensor would be fixed on the hopper frame and have a known transformation to the navigation center of the hopper. Attitude and range precision errors would be characterized before any mission flies to identify the effect of these parameters on the overall solution. Figure 60 shows an illustration of a hopper taking measurements out in front of the direction of travel, interrogating the surface that it will be flying over soon.

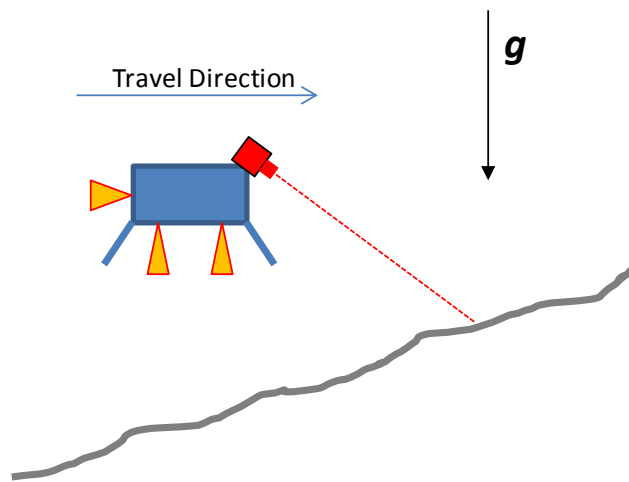


Figure 60 – Illustration of Hopper Slope & Roughness Detection using a Range Sensor

5.1 Sparse Slope & Roughness Operational Concept

Once the hopper has chosen a relatively safe landing area (LA) upon approach (from the Size Density Method) and is preparing to land, it can switch to using a short-range LIDAR that actively interrogates the surface in front of the hopper as it traverses downrange. Different possible triggers can be used for switching from the landing area selection to landing aim point selection phase: the LA border has been reached and/or the vehicle altitude is low enough that the LIDAR can begin to directly interrogate the surface.

Once landing aim point selection has begun, landing area selection does not need to continue. The vehicle is low enough to the ground that direct interrogation of the surface can occur. If a certain mission type is assessing future landing areas for multiple hops, landing area selection may continue in an open-loop fashion to plan for the next hop.

The range measurements from the short-range LIDAR are used to determine the slope and roughness at landing locations that are just ahead of the vehicle. Hoppers, and landers in general, need to land on surfaces that have relatively low slope compared to the gravity vector. This reduces the probability that

the vehicle will tip upon landing if one leg touches down before another, or if there is any significant lateral velocity at touchdown. Roughness is a measure of the deviation of the surface from being perfectly smooth. Small rocks and pits can cripple the landing legs of the vehicle, causing them to break or tip the vehicle. Lander legs are built to withstand some level of roughness but, the lower the surface roughness, the more likely the lander will be able to touchdown safely.

The range sensor may be fixed to the vehicle, or it may have a steering mirror or gimbal to allow the beam to be actuated separately from the vehicle motion. The forward motion of the hopper during traverse will provide downrange observability of the surface slope. However the sensor is mounted, crossrange observability will either occur from the vehicle's side-to-side motion, from having a line-beam LIDAR that is oriented horizontally, or from the beam being directly actuated by a steering mirror or gimbal. Without crossrange observability, the crossrange portion of the surface slope will be poorly estimated.

Figure 61 shows an illustration of the operational concept over time. The image is an overhead illustration showing the vehicle flight path over the surface (dashed blue line denotes vehicle path and blue star denotes current vehicle location at the given time step), the beam track traced out in front of the vehicle (dashed red sinusoid), and a box on the order of the size of the **VFDE** (black dashed box) that is the current Window of Regard (WoR) where the slope and roughness detection is occurring.

The illustration shows 3 tracks at successive time steps, with the vehicle flying in a straight line downrange and the beam track tracing a sinusoid along the surface.

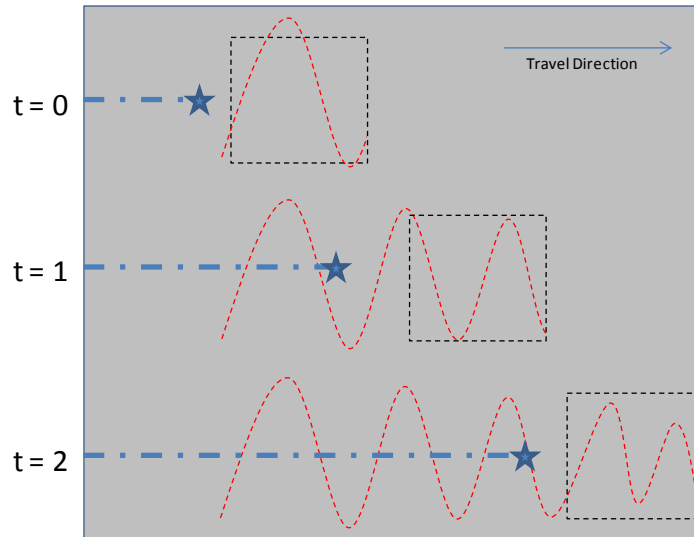


Figure 61 – Illustration of Window of Regard for Slope & Roughness Detection. Subsequent tracks show a progression of the vehicle flight path, beam pattern, and Window of Regard over time. The blue star denotes the location of the vehicle over the surface at the given time step. The blue dashed line shows the vehicle flight path over time. The dashed red sinusoid denotes the range sensor beam pattern over the ground out ahead of the vehicle. The dashed black box denotes the current Window of Regard where slope and roughness are being detected out in front of the vehicle.

5.1.1 Downrange Beam Pointing

As the vehicle traverses downrange, the beam will be pointed forward and down at an angle that keeps the WoR a certain amount of time ahead of the vehicle, i.e.: the vehicle will be directly over the WoR at τ seconds in the future. Figure 62 shows the pointing geometry parameters that can be used to compute the value for the beam's pointing angle up from nadir, α .

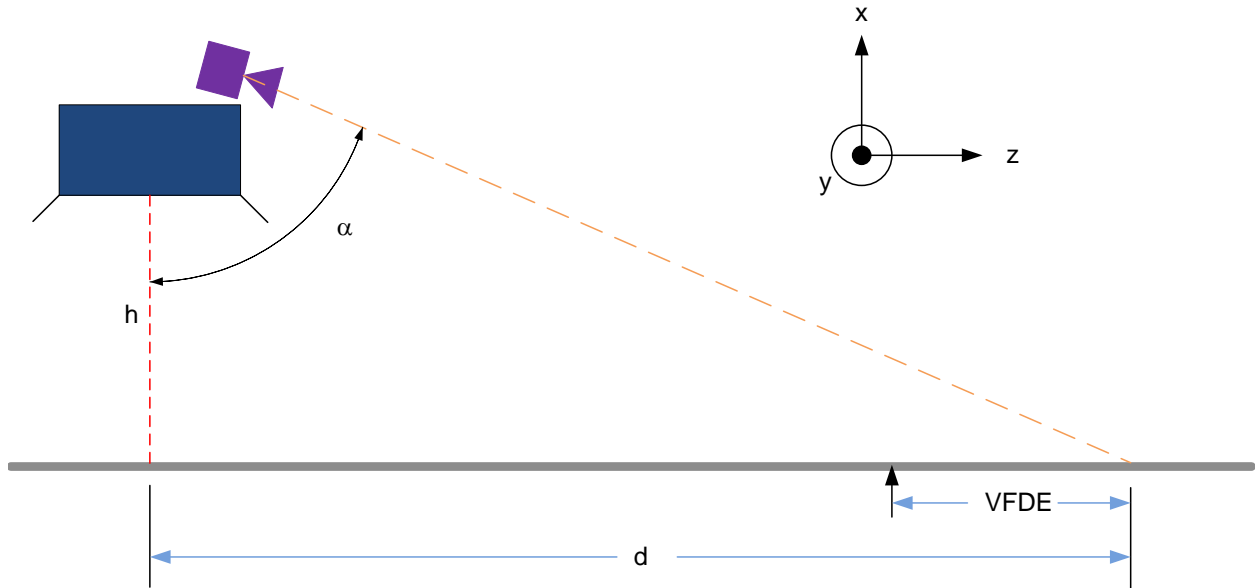


Figure 62 – Pointing geometry for slope and roughness range sensor. “h” is the altitude of the vehicle above the surface. “d” is the distance downrange that the beam intersects the mean surface. “ α ” is the angle of the beam pointing up from nadir.

The distance downrange, d , that denotes the toe of the WoR, can be estimated by knowing or estimating what the horizontal relative velocity will be at the end of the range, d distance away from the lander and knowing how much time, τ , is desired for decision making and control actuation to arrest the forward horizontal relative velocity, v , without major overshoot. τ would be a function of horizontal control authority and computational rate of the guidance algorithm (typically the limiting computation in the GNC loop).

The **VFDE** must also be taken into account, as the lander would need to be centered over the landing aim point (LAP). Equation 9 shows the simple relationship between the toe distance of the range sensor beam with horizontal relative velocity, time-to-aim-point, and **VFDE** diameter.

Equation 9
$$d = v\tau + \frac{VFDE}{2}$$

Given this simple geometry, the beam path angle up from nadir, α , can be set:

Equation 10

$$\alpha = \tan^{-1} \frac{d}{h}$$

With these relationships, the range sensor sizing and vehicle placement can be determined pre-flight for the hopper traverse mission design desired. The details of how slope and roughness are calculated are given below.

5.2 Sparse Slope & Roughness Detection Method Description

Slope and roughness detection using an active sensing technique, one that allows direct range measurements of the surface, creates a sparse digital elevation map that can be used to estimate the mean slope of the surface and compute deviations from that surface as roughness.

Sampled surface points create a sparsely filled 3-dimensional space with X, Y, and Z components on the digital elevation map. The points are captured in a 2-dimensional array with the number of rows equaling the number of points that are sampled. The elements of those rows contain the X, Y, and Z components of the sampled surface points.

Using the points gathered, the surface normal can be computed and compared against the gravity vector to determine the angle between the two vectors.

Once the surface normal is defined, the perfect “un-rough” surface can be computed. This surface can be used to estimate the perfect beam trace (for a smooth surface) and compared against the measurements of the actual beam track. Deviations between the estimated perfect and actual beam track gives a measure of the roughness of the surface.

5.2.1 Slope: Basic Formulation

Surface slope is determined by estimating the normal vector, \mathbf{N} , of the surface area of interest and comparing it against the estimated gravity vector, g . The angle between these two vectors gives the gravity relative slope of the surface, θ , shown in Figure 63 and determined by Equation 11.

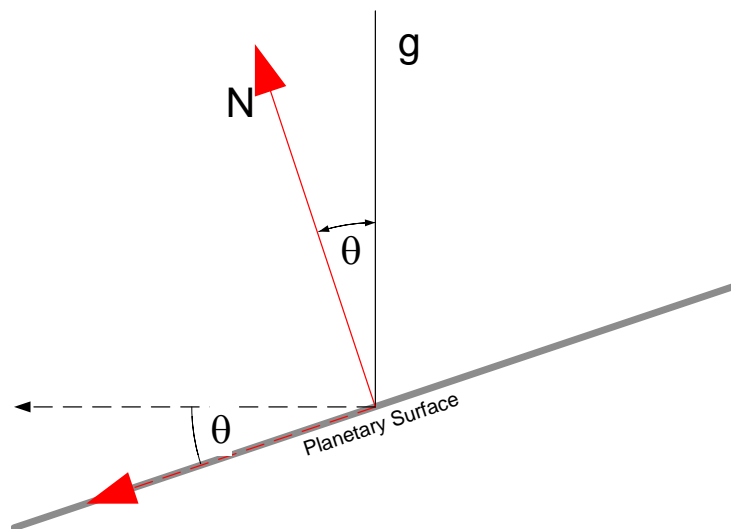


Figure 63 – Slope computed as angle between Normal and gravity vectors

Equation 11

$$\theta = \cos^{-1} \frac{N \cdot g}{\|N\| \|g\|}$$

The basic equation of a plane given by:

Equation 12

$$ax + by + cz + e = 0$$

where:

x, y, z = coordinates of the measured surface points
 a, b, c = are the coefficients of the normal vector: \mathbf{N}
 e = scalar used in determining height of plane

which can be rearranged and placed into matrix form:

Equation 13

$$Au = B$$

where:

$$\mathbf{A} = \begin{bmatrix} x_1 & y_1 & z_1 \\ \vdots & \vdots & \vdots \\ x_n & y_n & z_n \end{bmatrix}, \text{ which is an n-by-3 matrix of the measured } \mathbf{x}, \mathbf{y}, \mathbf{z} \text{ points}$$

$$\mathbf{B} = - \begin{bmatrix} e_1 \\ \vdots \\ e_n \end{bmatrix}, \text{ which is an n-by-1 matrix of the } \mathbf{e} \text{ points}$$

$$\mathbf{u} = \begin{bmatrix} a \\ b \\ c \end{bmatrix}, \text{ which are the three unknown variables of the normal vector}$$

Using the least squares formulation, the best estimate of the \mathbf{u} vector is given by solving Equation 13 for \mathbf{u} .

To solve for $\mathbf{a}, \mathbf{b}, \mathbf{c}$, it is assumed that all values of \mathbf{e} are equal and nonzero for each equation (\mathbf{e} is the height of the plane and is used to make all points estimated co-planar). Since the slope is the desired measured quantity, adjusting the value of \mathbf{e} will just scale the values of $\mathbf{a}, \mathbf{b}, \mathbf{c}$, but will not change their relative magnitudes. A nonzero \mathbf{e} value is needed to provide non-zero estimates of the \mathbf{u} vector.

Solving for the least squares (using the Moore-Penrose pseudo-inverse formulation) estimate of \mathbf{u} gives a best estimate solution for $\mathbf{a}, \mathbf{b}, \mathbf{c}$. The pseudo-inverse formulation is an expensive, but necessary, method for non-square, or singular, \mathbf{A} matrices:

Equation 14

$$\mathbf{u} = (\mathbf{A}^T \mathbf{A})^{-1} \mathbf{A}^T \mathbf{B}$$

Solving for \mathbf{u} gives the normal vector as:

Equation 15

$$N = [a, b, c]$$

5.2.2 Sparse Slope: Alternate Formulation

The above formulation may be ill-conditioned. An alternate formulation with fewer variables can improve both speed and conditioning.

Assuming that $c = 1$ (the coefficient of z) and that e is constant, the solution can be simplified to solve for only two variables: a & b . This formulation removes the need to estimate or know the height of the surface and focuses on determining the local slope (estimated as the slope of a plane). This formulation is also conditioned to work for relatively low angle slopes from horizontal ($[a, b] \ll 1$). Making these assumptions provides a quicker, more reliable way of estimating the surface slopes for hopper landing areas of interest.

The new equation to solve for becomes:

Equation 16
$$ax + by + 1z + const = 0$$

which can be rearranged and placed into a new matrix form:

Equation 17
$$A'u' = B'$$

where:

$$A' = \begin{bmatrix} x_1 & y_1 & const \\ \vdots & \vdots & \vdots \\ x_n & y_n & const \end{bmatrix}, \text{ which is an n-by-3 matrix of the } \mathbf{x} \text{ and } \mathbf{y} \text{ points, with a constant column}$$

$$B' = - \begin{bmatrix} z_1 \\ \vdots \\ z_n \end{bmatrix}, \text{ which is an n-by-1 matrix of the } \mathbf{z} \text{ points}$$

$$u' = \begin{bmatrix} a \\ b \\ const \end{bmatrix}, \text{ which are the two unknown variables of the normal vector}$$

Solving for the least squares estimate of u' gives a better conditioned solution for u'

Equation 18
$$u' = (A'^T A')^{-1} A'^T b'$$

which taken with the assumptions given above for $c = 1$ and $e = const$, gives the normal vector as

Equation 19
$$N' = [a', b', const]$$

This solution provides a better-conditioned solution for N' . It also reduces computation by reducing the number of variables and the order of the matrix inversion that needs to be performed.

5.2.3 Roughness Formulation

Given the slope and range to surface, the nominal beam track over a smooth surface can be estimated and compared to the actual measurements (over a rough surface) to understand the residual:

$$\text{Equation 20} \quad \text{roughness} = \max(\text{abs}(\text{Path}_{\text{estimated}} - \text{Path}_{\text{actual}}))$$

where:

$\text{Path}_{\text{estimated}}$ = the least squares estimate of the range sensor beam path on a smooth plane

$\text{Path}_{\text{actual}}$ = the actual range sensor beam in three dimensions

Equation 20 is valid for an ideal range sensor (noiseless), but to get a more accurate measure of roughness, the range precision of the sensor should be addressed. Here, the concern is more on the noise and not the bias of the sensor. The bias will skew the range measurements in a constant direction, whereas the noise will tend to be a discrete Gaussian noise (127). Range sensors use time-of-flight measurements and range precision is a function of signal-to-noise and timing precision of the onboard oscillator. Taking into account the range precision of the sensor gives:

$$\text{Equation 21} \quad \text{roughness} = \max(\text{abs}(\text{Path}_{\text{estimated}} - \text{Path}_{\text{actual}})) - \sigma$$

where

σ = standard deviation of the range precision noise

Using the maximum of the difference between the estimated and actual beam path gives a higher probability that crippling hazards will be detected.

5.2.4 Hazard Detection using Sparse Slope & Roughness

To apply the slope and roughness detections to hazards requires knowledge of the vehicle landing tolerances. The roughness tolerance is a measure of the landing gear endurance while the slope coupled with the vehicle horizontal velocity dispersions affect the tipping moment at landing.

Given the slope and roughness tolerances of the vehicle, simple thresholds can be applied to understand if the area being sensed is a safe landing location for the traversing hopper. Based on horizontal relative velocity and beam angle to the ground, the hopper may only be several seconds from the landing area under regard, thus a quick formulation is beneficial to enable safe landing.

The timing and performance characteristics of this technique to rapidly detect slope and roughness are given below.

5.3 Simulation Environment

A simulation environment was created to test the performance and timing of the Sparse Slope & Roughness Detection Method.

Figure 64 shows the flow diagram for the Sparse Slope & Roughness Detection simulation. First, the simulation environment inputs a DEM. The surface is added above what would be the navigation filter estimated mean surface³. The vehicle and beam pattern are simulated and run over the DEM. The simulation estimates the slope and smooth surface (assuming a smooth plane based on the normal vector computed during the slope calculation). The smooth surface is differenced from the beam pattern to determine the roughness of the surface.

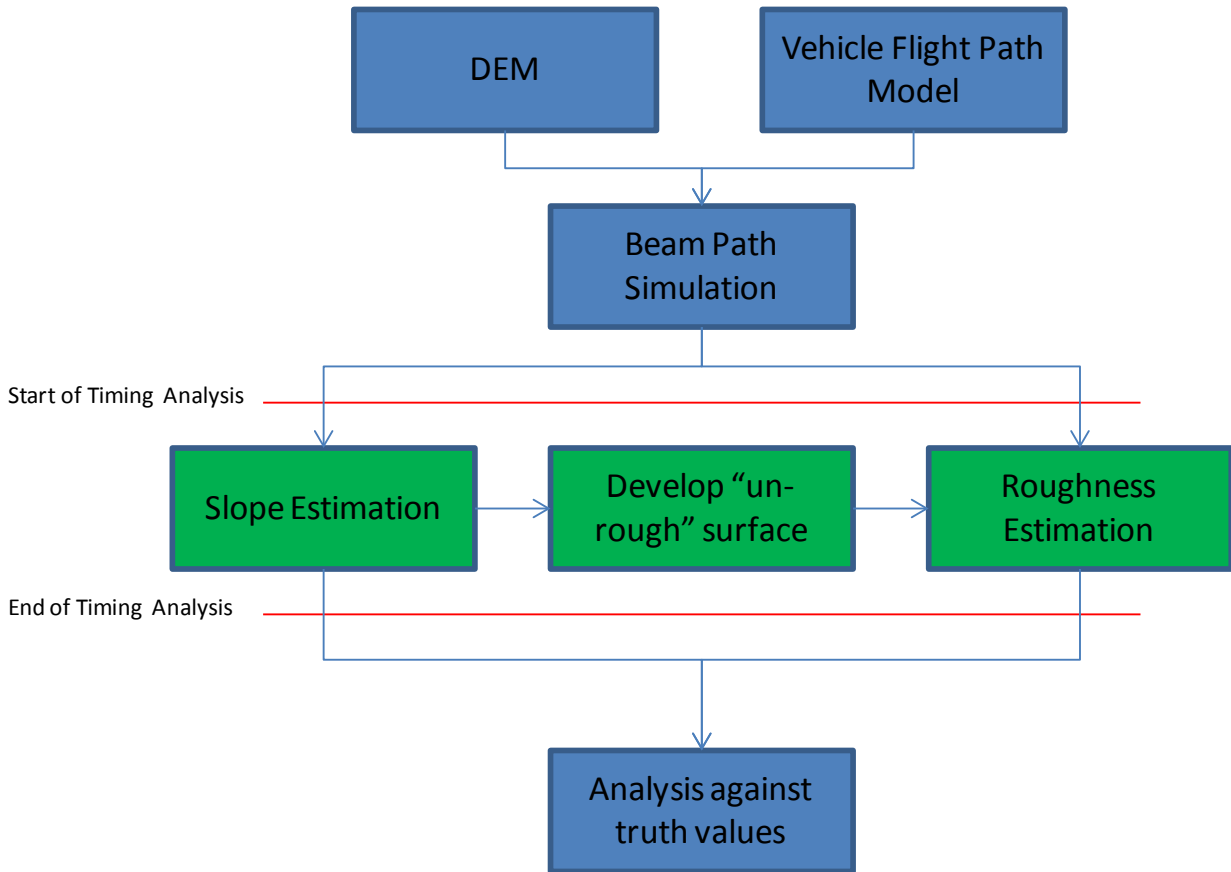


Figure 64 – Slope & Roughness Simulation Environment Flow Diagram

Figure 65 shows a representative sloped surface with no roughness for illustration. The z-axis is accentuated to show the level of slope in the surface. The blue path above the surface is the vehicle flight path. Each star in the vehicle flight path signifies when a measurement was taken. The blue sinusoid traces the beam pattern on the mean surface. The gray plane is the sloped DEM. The red sinusoid is the beam track that intersects the surface.

³ The mean surface of a planetary body is estimated as a smooth ellipsoid.

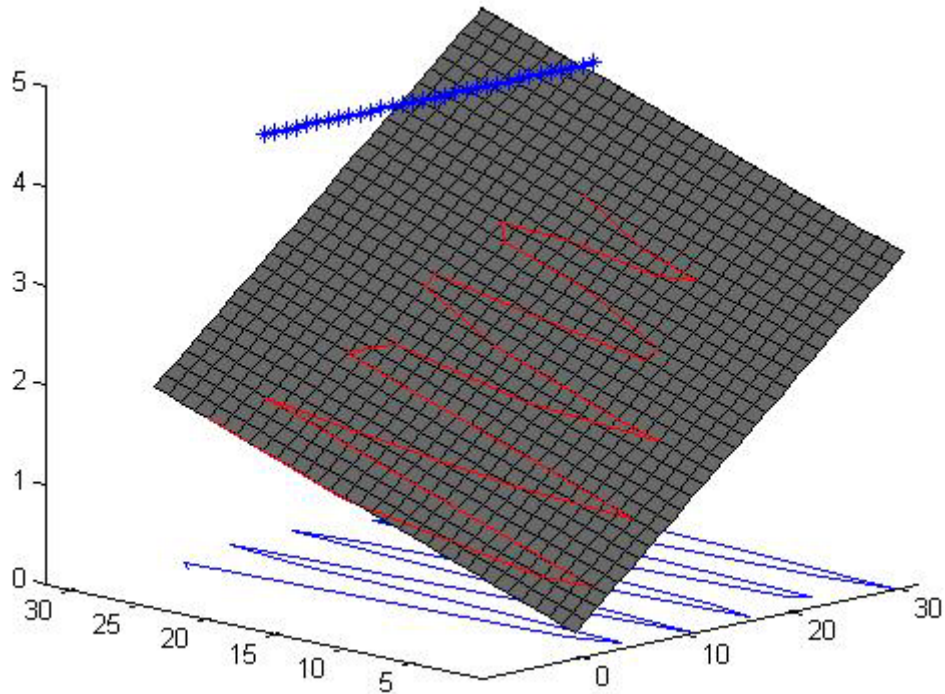


Figure 65 – Slope & Roughness simulation output for timing analysis

The simulation environment scans a box the size of the VFDE over a DEM performing the slope and roughness detection in the box at every point. The tradespace consists of varying the beam pattern frequency (sample density), slope tolerance and roughness tolerance to assess the ability of the algorithm to detect slope and roughness compared to the “truth” algorithm over the entire map (57).

The analysis captures the time for each run, and the detection statistics over an entire DEM. The detection statistics are categorized into four conditions:

- 1) False Positives (FP) – missed detection of a hazard
- 2) False Negatives (FN) – incorrectly detected a hazard when there was not one
- 3) True Negatives (TN) – correctly assessed a dangerous site as dangerous
- 4) True Positives (TP) – correctly assessed a safe LAP as safe

False Positives are the most critical of the four conditions because missed detections of hazards may cripple the vehicle if the missed hazard is large and the vehicle chooses to land at that point. Moreover, most of the missed detections are based on border cases, where the areas are near the slope and roughness tolerances and/or near other large hazards.

5.3.1 Truth Slope and Roughness

To demonstrate the method, the Luna 23/24 LRO DEM is used again. The LRO postings are 2 meters apart and have a precision of 1 meter in altitude (114)(128). The LRO DEMs have been interpolated to create a 0.125m posting DEM. Rocks were added to the model using a power law distribution from Golombek et al (129). Current work is being done to determine the lunar crater size frequency distribution (130)(131), but for this analysis there has been no additional craters added to the DEMs.

The analysis runs for testing the slope and roughness algorithm were run on 1024 landing area DEMs created from the large Luna 23/24 landing region DEM. Figure 66 shows a smooth interpolated LA DEM (without rocks added to it). Interpolated, the DEM is about 450 pixels x 600 pixels. If each LAP is 2m in diameter, than there are 64 pixels per LAP with a pixel resolution of 0.125 meters.

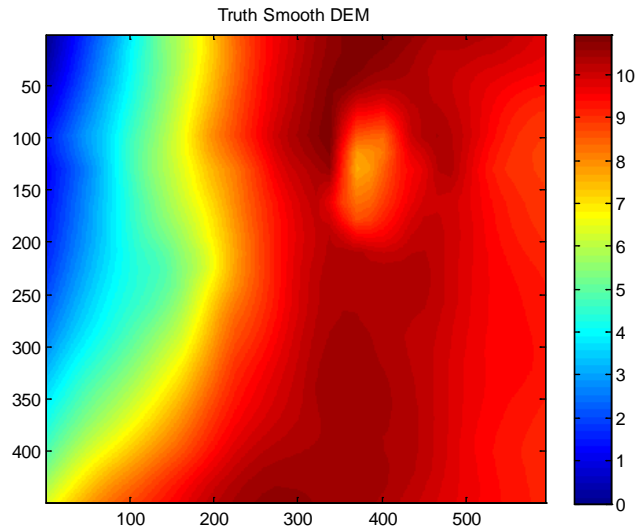


Figure 66 – LA DEM1 from the Luna 23/24 region

To this surface, rocks are added and the slope and roughness of each LAP is calculated using perfect knowledge of the rock locations and least squares estimation of the slope using the full pixels available. Figure 67 shows the slope (left) and roughness (right) maps for DEM1. The color bar represents the slope in degrees and the roughness in meters (values above the roughness threshold are starred).

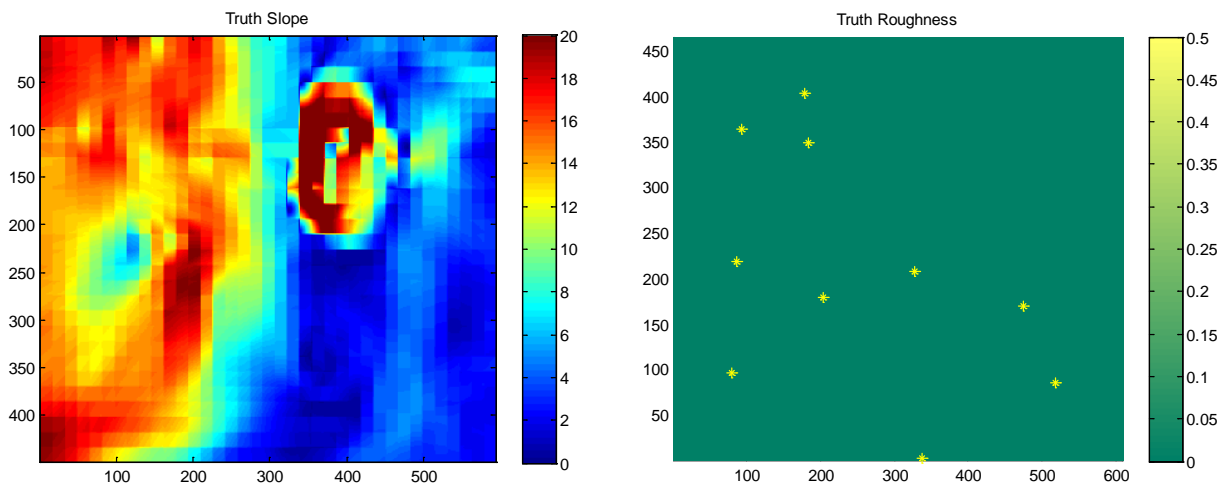


Figure 67 – LA DEM1 truth slope and roughness map

A map is generated of the overall safe and hazardous sites over the entire map using the vehicle thresholds of 10 degrees for slope and 0.3 meters for roughness. Figure 68 shows sites that are identified as hazardous (red) and safe (blue).

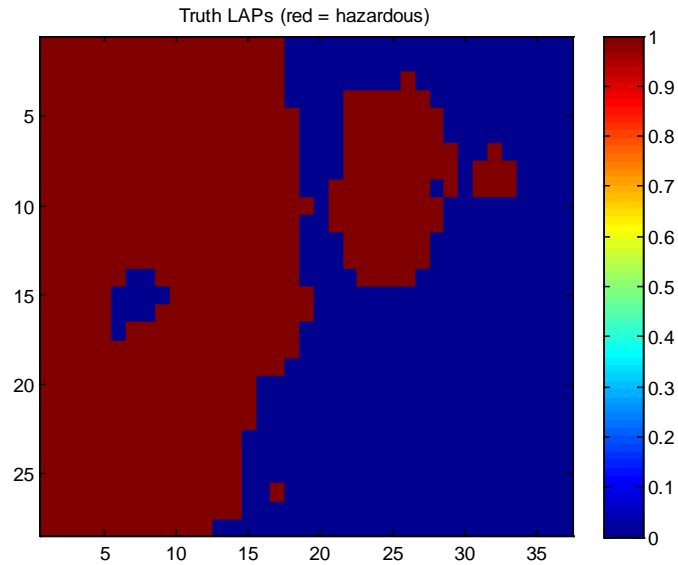


Figure 68 – DEM1 safety map. Safe areas are shown in blue, while hazardous areas are shown in red.

5.3.2 Sparse Slope & Roughness Method

The Sparse Slope & Roughness Method uses the formulation described above to sample surface points and estimate the slope and detect the maximum roughness in a LAP. Figure 69 shows the estimated smooth map using a 10% scan density of the surface.

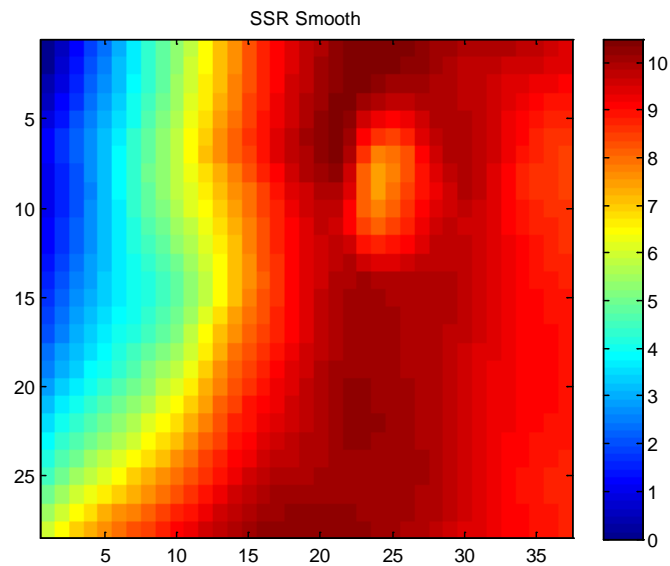


Figure 69 – LA DEM1 SSR smooth map

Figure 70 shows the slope and roughness map from the Sparse Slope & Roughness Method. The slope map is generated during the same calculation as the smooth map. The roughness map is the difference between the actual beam points and the estimated smooth map.

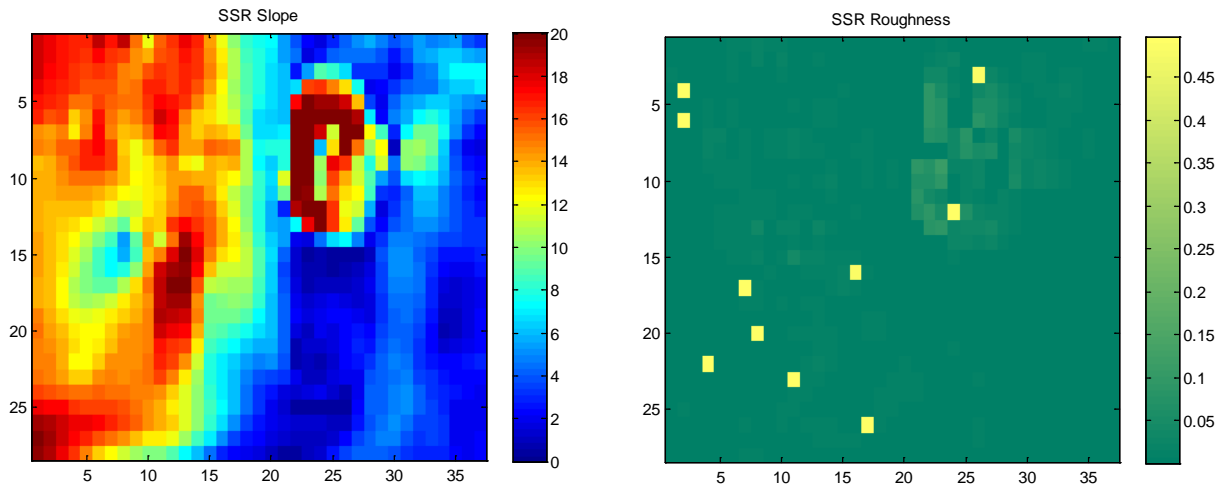


Figure 70 – Estimated slope and roughness map using Sparse Slope & Roughness

The same slope and roughness tolerances are applied to these maps and a map is generated with the safe and hazardous LAPs. Figure 71 shows the safe and hazardous landing aim points using the SSR method.

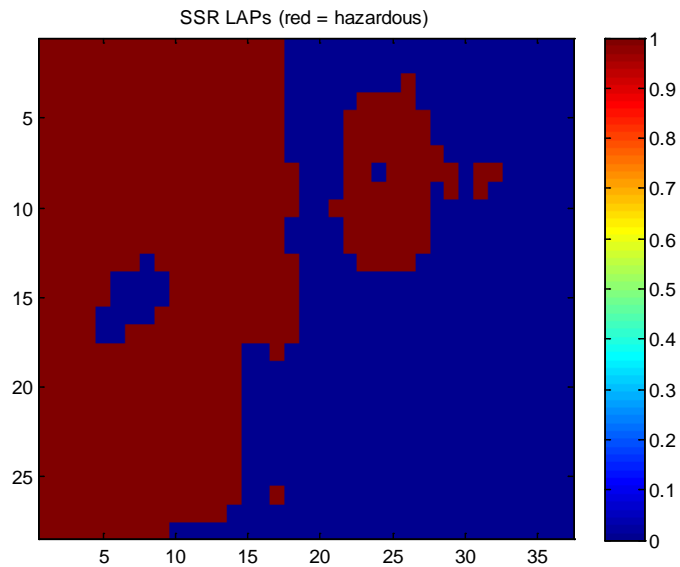


Figure 71 – SSR LAPs

Figure 72 shows the difference between the LAP truth map and the LAP Sparse Slope & Roughness map. Points in red are false positives; points in green represent locations of true negatives and true positives; points in blue are false negatives (none on this map). As can be seen from the plot, there are very few false positives and the majority of the map consists of true negatives and positives (correct detections).

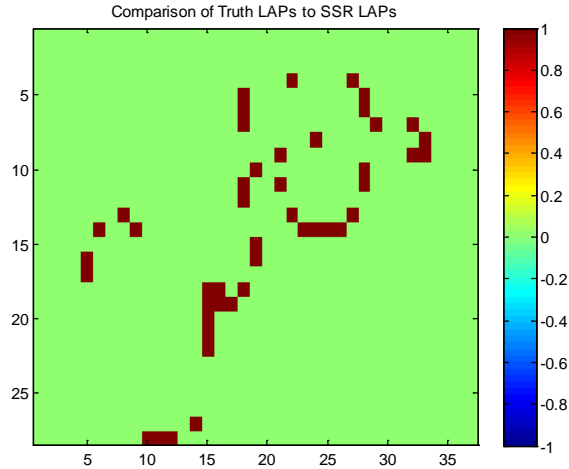


Figure 72 – Comparison of truth LAPs to SSR LAPs

This analysis showed the process for a single DEM. In the following section the full 432 DEMs are analyzed for performance and timing over scan densities from 10% to 100%.

5.4 Performance and Timing Analysis

5.4.1 Performance Analysis

Runs were performed with the slope tolerance set to 10 degrees, and the roughness tolerance set to 0.3 meters. False Positives, False Negatives, True Negatives, and True Positives were gathered over the entire DEM for all 432 landing areas using scan densities from 10% to 100% (in increments of 10%).

Figure 73 shows the mean TP, TN, FP, FN percentages for each scan density over the 432 DEMs. TPs and FNs are divided by the total number of safe LAPs, while TN and FP are divided by the total number of hazardous LAPs. As can be seen, scan densities below 30% only break even in detecting hazards. This implies that a push-broom line beam LIDAR or high frequency scanning point beam LIDAR is needed to produce good results.

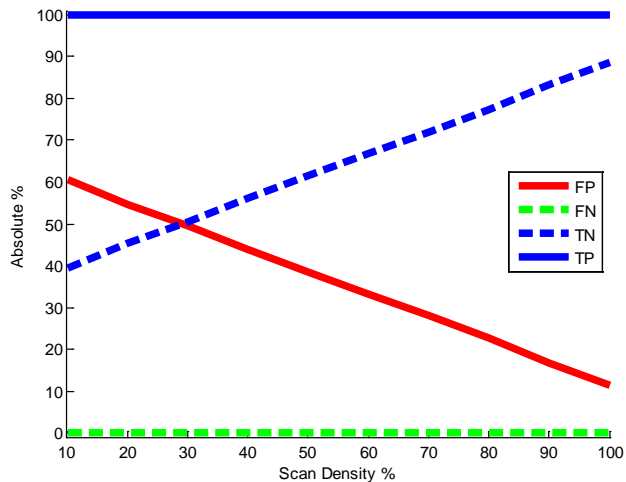


Figure 73 – TP, TN, FN, FP as a function of scan density

Figure 74 shows the mean TP, TN, FP, FN percentages for each scan density over the 432 DEMs, but with the hazard tolerances cut in half. TP detections are sacrificed for FNs, but the percentage of FPs is reduced. This increases the likelihood that a high frequency scanning point beam LIDAR could work to produce good results. In general, a push-broom line beam LIDAR (which can provide high scan densities while the hopper is traversing) would be a good candidate to provide slope and roughness hazard detection aboard a hopper.

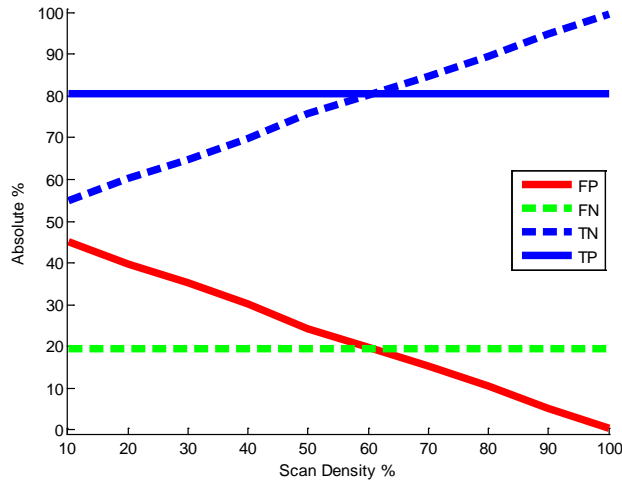


Figure 74 – TP, TN, FN, FP as a function of scan density at half hazard tolerances

5.4.2 Timing Analysis

With each measurement from the range sensor, a new slope & roughness estimate for the WoR at the current time can be made. Since measurements can be made quickly, it is essential that this algorithm also runs quickly to provide timely estimates of the safety of the upcoming landing site. Figure 75 shows the time in seconds over the different scan density values, with 1 million LAP simulation runs per scan density.

The average time for a computation of the slope & roughness increased steadily, but was still very fast (less than 0.13e-4 seconds). The 2σ time standard deviation is plotted in green (uncorrelated 95% confidence). This analysis was performed on a Windows 7 machine with an Intel Core i5 2.6 GHz processor, and 4 GB of RAM. The times for each simulation were recorded using Matlab’s tic toc functionality.

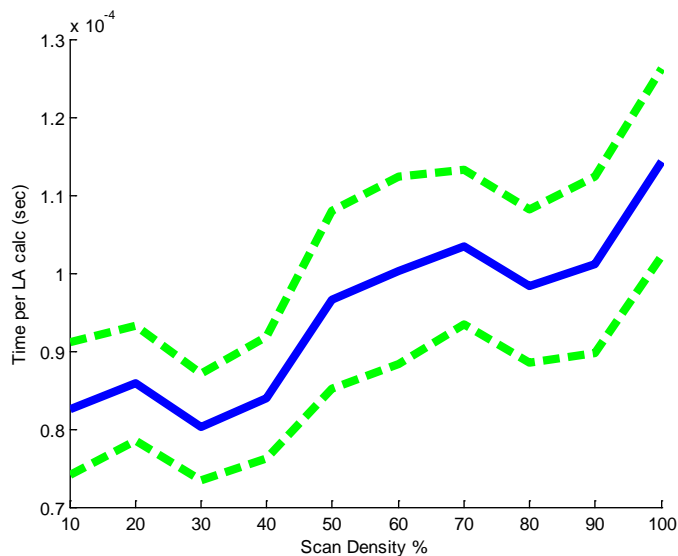


Figure 75 – Spare Slope and Roughness algorithm run times for given scan densities

5.5 Combined SDM and SSR Analysis

In this section, the SDM and SSR are combined into one simulation. The simulation captures final landing aim point selection safety. First, SDM is run on a given landing region DEM to select the best landing area. Once the landing area is chosen, then SSR is run to determine a safe landing aim point.

The runs were done with twenty-eight 2km x 2km LRO DEMs from the Mare Crisium region of the Moon. Mare Crisium is centered at a latitude of 17° N and is 555 km in diameter. An LRO DTM strip running from North to South was used to extract the 28 landing region DEMs.

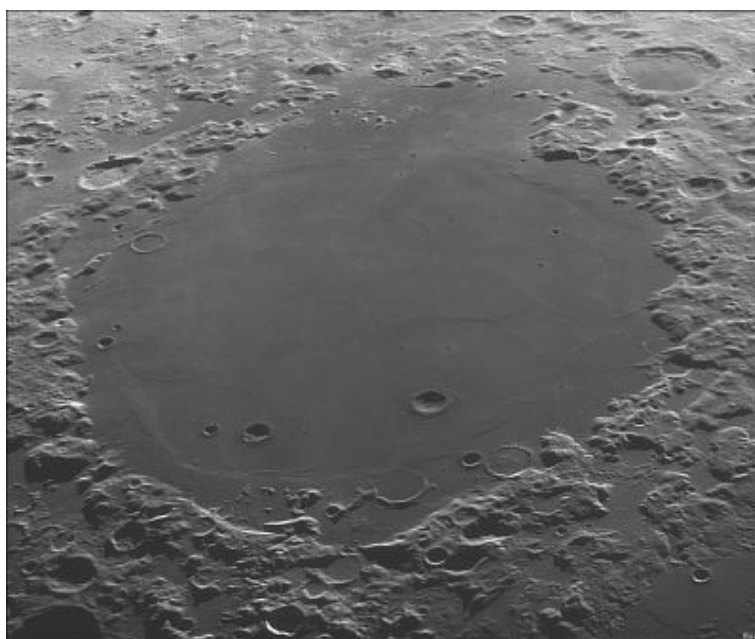


Figure 76 – Mare Crisium basin

Lighting conditions were rendered for the landing area selection tradespace and LA DEMs were created for the top selected Landing Area for each run. The tradespace includes 28 DEMs, 4 view elevation angles (10, 20, 30, 90 degrees), 4 sun azimuth angles (0, 90, 180, 270 degrees), 4 sun elevation angles (15, 25, 35, 45 degrees), 10 scan densities (10% to 100%), 4 short-range LIDAR noise sigmas (noiseless, 0.001m, 0.01m, 0.1m), and 2 tolerance settings (full tolerance settings, which are 0.3 meters for roughness and 10 degrees for slope; and half tolerance settings, which are 0.15 meters for roughness and 5 degrees for slope). This combines to 143,360 distinct landing simulations.

The overall simulation across all landings had a 99% success rate. This is a powerful result that shows the SDM with SSR concept of operations is very capable of providing safe landing locations across a wide tradespace of parameters. SDM does a good job of selecting landing areas that are relatively safe (thus reducing the risk of going to a landing area that is hazardous) and the SSR method is able to detect safe landing aim points.

Table 9 shows the percentage of safe landing aim points at different stages in the mission and relates the results back to landing safety percentage for blind landings. This table shows results broken out by the 28 distinct 2km x 2km Landing Regions from Mare Crisium.

Column 1 shows the landing region number. Each landing region is 2000m x 2000m.

Column 2 (LR Safety % - total) shows the percentage of safe landing aim points within the entire landing region. If the mission did not have any hazard detection or avoidance, this is the percentage of time that the mission would blindly land safely. For the landing regions chosen (the Mare Crisium set), this is a relatively high percentage, but it is important to note that within each landing region there are landing areas that have very few safe landing aim points. Column 3 (LR Safety % - Worst LA) shows the blind landing safety for the worst landing areas in each landing region.

Column 4 (Chosen LA – Safety %) shows the selected landing areas safety percentage. Column 5 (Final Lap Safety) shows the selected landing aim point safety percentage.

Column 6 (Improvement using SDM) shows SDM's chosen LA over the mean safety percentage in the entire landing region. For most LRs, SDM shows good improvement in safe landing percentage. This is a strong result. There are several cases where SDM does not improve landing area safety. For most LR 10 and 24, the regions are already quite safe, and SDM was unable to improve upon the LA safety. For LR 8, SDM did not work well for one sun azimuth angle. Figure 79 shows LR 8 and when the sun azimuth came from the side, SDM mistakenly chose a LA that was near the cliff region and was not safe. The cliff feature is prominent, but was not accentuated by either a shadow or bright feature at this azimuth.

Column 7 (Improvement using SDM and SSR) shows the results after running SSR on the chosen LAs. Column 7 shows how SDM+SSR combine against blind landings. The infusion of noise into the model for SSR reduces the safe landing statistics for several of the cases shown, but the landing percentage is still high across all Landing Regions.

Column 8 (Improvement using SSR) shows the effects of using only SSR. SSR shows minor improvements from SDM only for most LRs. LR 8, where SDM did not perform as well, shows where SSR was able to greatly improve the final LAP safety. Together, SDM and SSR combine to provide a strong method for safe LAP selection.

Table 9 – Full tradespace results, combining SDM with SSR

LR DEM#	Blind Landing Safety		SDM & SSR				Improvement using SSR
	LR Safety (total)	LR Safety (Worst LA)	Chosen LA Safety	Final LAP Safety	Improvement using SDM	Improvement using SDM+SSR	
1	92.3%	2%	96.3%	100.0%	4.4%	8.4%	3.8%
2	90.6%	1%	94.3%	100.0%	4.1%	10.4%	6.0%
3	95.3%	6%	97.6%	98.5%	2.4%	3.3%	0.9%
4	96.2%	39%	99.3%	100.0%	3.3%	4.0%	0.7%
5	89.4%	2%	99.2%	99.2%	10.9%	11.0%	0.0%
6	94.0%	24%	99.0%	100.0%	5.3%	6.3%	1.0%
7	87.6%	11%	97.0%	96.9%	10.6%	10.5%	-0.1%
8	76.4%	1%	74.3%	94.8%	-2.8%	24.0%	27.5%
9	96.6%	28%	99.0%	94.5%	2.5%	-2.1%	-4.5%
10	95.5%	15%	93.8%	97.1%	-1.9%	1.6%	3.5%
11	92.0%	7%	95.6%	98.5%	3.9%	7.0%	3.0%
12	95.4%	27%	98.5%	99.2%	3.2%	3.9%	0.7%
13	94.3%	3%	99.0%	99.2%	5.0%	5.3%	0.2%
14	90.4%	0%	99.0%	98.3%	9.5%	8.7%	-0.8%
15	95.4%	20%	98.7%	100.0%	3.5%	4.8%	1.3%
16	90.8%	3%	97.9%	97.0%	7.9%	6.9%	-0.9%
17	97.2%	45%	99.7%	98.1%	2.6%	1.0%	-1.5%
18	89.2%	1%	98.7%	100.0%	10.7%	12.2%	1.3%
19	96.5%	12%	99.5%	100.0%	3.1%	3.6%	0.5%
20	96.9%	10%	99.9%	100.0%	3.2%	3.2%	0.1%
21	96.5%	36%	99.2%	100.0%	2.8%	3.6%	0.8%
22	93.8%	10%	99.1%	100.0%	5.6%	6.6%	0.9%
23	96.1%	37%	98.4%	99.9%	2.4%	3.9%	1.5%
24	93.0%	8%	92.0%	94.8%	-1.1%	1.9%	3.1%
25	94.1%	24%	98.9%	99.2%	5.0%	5.4%	0.4%
26	94.1%	16%	98.4%	96.9%	4.5%	3.0%	-1.5%
27	90.0%	2%	95.0%	100.0%	5.6%	11.1%	5.3%
28	90.4%	1%	98.5%	99.2%	8.9%	9.8%	0.8%

Table 10 shows slices through the tradespace through all variables: hazard tolerance, scan density, sensor noise, sun azimuth angle, sun elevation angle, and view elevation angle. As can be seen, no one factor stands out above all others, but there are small improvements by increasing view elevation and using the half hazard tolerance values. Sensor noise was infused into the simulation for SSR, with

random drop outs and 1 sigma noise levels of 0.001 to 0.1 meters. In some cases the larger LIDAR noise made the solutions more conservative (more False Negatives and True Negatives).

The simulations performed relatively similar across all scan densities. The coupling of SDM with SSR is represented in the final results. Using the methods together allows for the use of a sparse DEM during SSR. This would allow mission planners to use simpler sensors and still achieve a high landing aim point safety percentage. To ensure better performance out of SSR as a standalone method, Figure 73 and Figure 74 show that a LIDAR with a higher scan density is desired.

Table 10 – Full tradespace results across all variables

Haz Tol	Safe Landings		SunAZ Angle	Safe Landings
Full	98.1%		0 deg	98.0%
Half	99.3%		90 deg	98.5%
			180 deg	99.3%
			270 deg	99.1%
Scan Density	Safe Landings			
10%	98.5%			
20%	98.6%			
30%	98.7%		SunEL Angle	Safe Landings
40%	98.7%		15 deg	98.6%
50%	98.7%		25 deg	98.6%
60%	98.8%		35 deg	99.2%
70%	98.8%		45 deg	98.6%
80%	98.8%			
90%	98.9%			
100%	98.9%			
			ViewEL Angle	Safe Landings
			10 deg	98.0%
Sensor Noise	Safe Landings		20 deg	98.5%
~0 m	98.0%		30 deg	99.3%
0.001 m	98.5%		90 deg	99.1%
0.01 m	99.3%			
0.1 m	99.1%			

To illustrate the full simulation runs, Landing Regions 1 and 8 are expanded upon below. These regions are a good cross section of landing regions that were very safe and the most dangerous.

The LR DEMs, LR images, LA DEMs, and selected LAPs are shown for sun azimuth of 90 degrees, sun elevation of 25 degrees, view elevation of 90 degrees, scan density of 10% with a noiseless sensor, and full slope and roughness hazard tolerances.

Figure 77 and Figure 79 show landing regions 1 and 8, respectively. The top-left image in each image is the DEM, with the corresponding MDM actual cost map in the bottom-left. The rendered image is in the top-right, with the corresponding SDM weighted cost map in the bottom-right. Each image shows the selected landing area with a white box.

Figure 78 and Figure 80 show the selected landing area for regions 1 and 8, respectively. The left image shows the DEM of the landing area. The right image shows the hazard map (with blue as safe and red as dangerous). The white box denotes the selected Landing Aim Point.

These figures show the use of SDM and SSR from start to finish, and how the selected Landing Regions and corresponding Landing Areas appear for two selected cases. As can be seen, SDM selects LAs that are relatively safe, and SSR selects safe LAPs within those LAs.

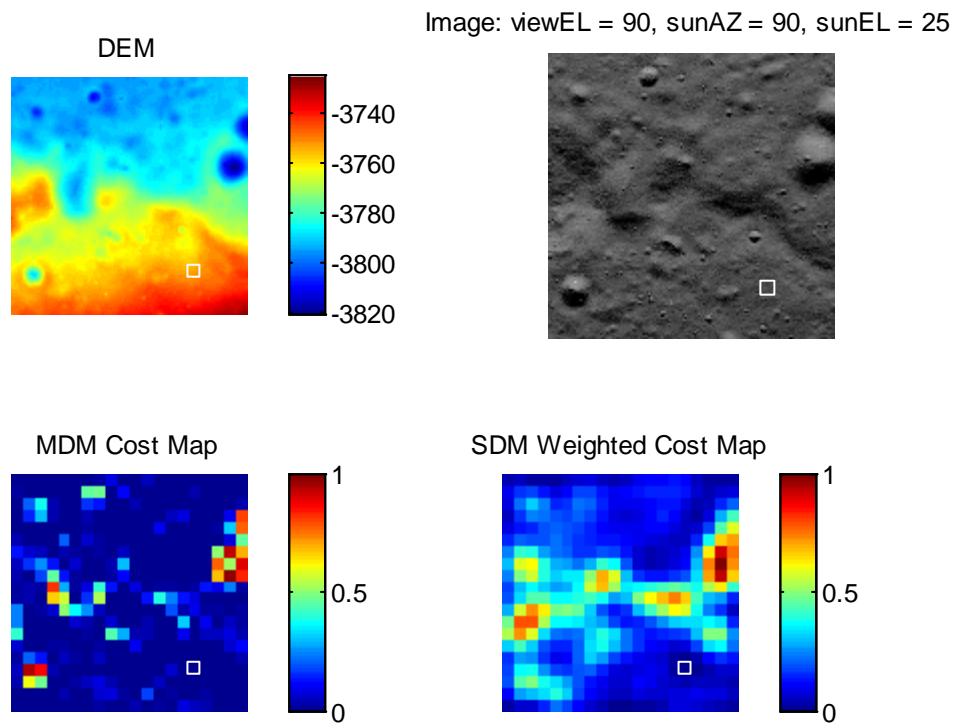


Figure 77 – Landing Region 1. DEM (top-left) with corresponding MDM cost map (bottom-left). Rendered image (top-right) with corresponding SDM cost map (bottom-right). The chosen landing area is given by the white box in each image.

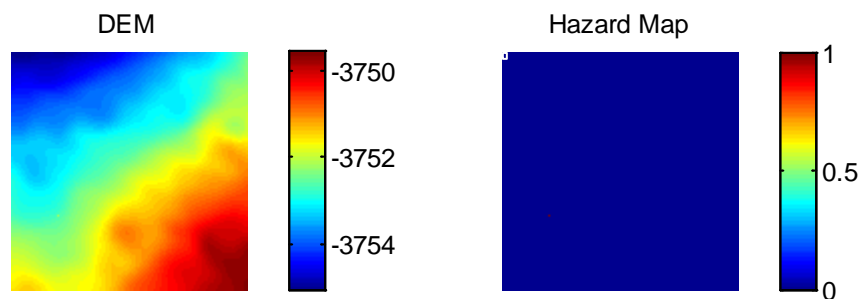


Figure 78 – Landing Region 1 selected Landing Area. Landing Area DEM (left) with corresponding hazard map (right). The chosen landing aim point is given by the white box in the hazard map.

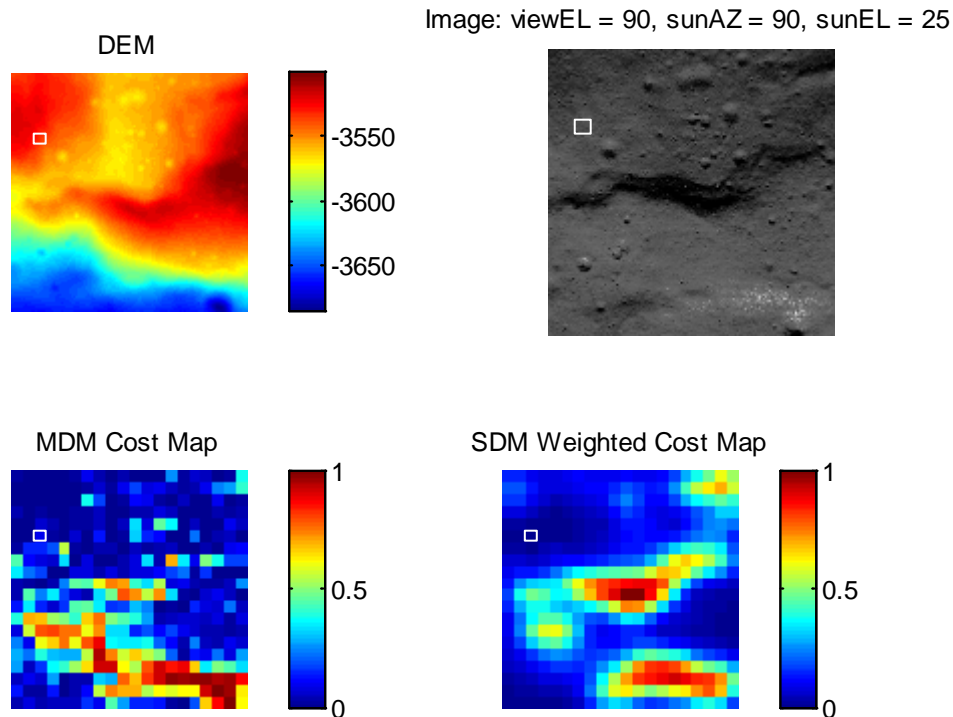


Figure 79 – Landing Region 8. DEM (top-left) with corresponding MDM cost map (bottom-left). Rendered image (top-right) with corresponding SDM cost map (bottom-right). The chosen landing area is given by the white box in each image.

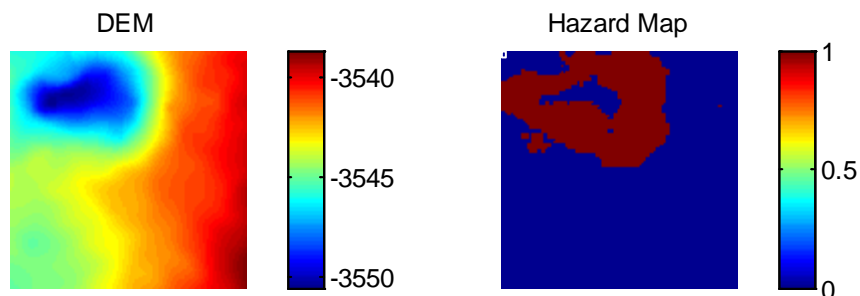


Figure 80 – Landing Region 8 selected Landing Area. Landing Area DEM (left) with corresponding hazard map (right). The chosen landing aim point is given by the white box in the hazard map.

5.6 Chapter 5 Summary

In this chapter, a method for detecting safe landing aim points using a short-range LIDAR for slope and roughness hazard detection was described. This method provides more precise hazard detection near the landing aim point, as the hopper is near the end of the hop and preparing to land. This method can be used in concert with the landing area selection method described in the previous chapter.

The method is predicated on using a simple sensor that scans the terrain ahead of the vehicle while it is traversing forward. Samples taken using the short-range LIDAR are used to estimate the surface slope and roughness.

The analysis of this method shows that it runs extremely fast, and performs well at detecting overall surface slope and roughness. The method is limited by very rough terrain, rapid traverse speeds and poor sensor range precision. For practical terrain and sensor choices, the method performs very well.

Coupled with the Size Density Method, slope and roughness detection using a short-range LIDAR near landing is a highly reliable tool for enabling safe landing. Over the SDM and SSR tradespace 143,360 individual simulation runs were performed and the final landing aim point was safe 99% of the time. Success over a large parameter tradespace of sun angles, view angles, scan densities, sensor noise, and hazard tolerances demonstrates a powerful solution using SDM combined with SSR.

6 Conclusions

This thesis has provided a description of the hopper traverse mission and methods to enable safe hopping from one planetary location to another. Different hopper mission scenarios were described along with their unique challenges. An operational concept was described for the overall hopper traverse mission and two complimentary methods were identified to enable landing area selection during traverse and hazard detection once near the landing site. The first method, the Size Density Method, detects features and uses them to calculate the relative safety between landing areas and is effective at shallow path angles and long ranges. The second method, Sparse Slope and Roughness, detects slope and roughness using a short-range LIDAR. This second method is more precise and works well from short range, near the end of the hop.

Current systems under development are being designed to precisely detect hazards upon descent for landing, but they are range limited and require mass, volume, power, and computational processing that would inhibit their use on a small robotic vehicle. The methods described in this thesis aim to use simple sensors and fast algorithms to enable hopper missions by reducing the mass, volume, power, and computational processing required as part of the navigation and hazard detection suite of sensors.

6.1 Summary of Contributions

A need was identified to supply a description of how a hopper could be precisely flown and how safe multiple landings could be enabled without using complex sensors. These descriptions were provided from the development of the hopper mission scenarios and constraints, to the understanding of the current methods used for planetary landers and rovers.

6.1.1 Description of Hopper Mission Scenarios

Several hopper mission scenarios were described with operational concepts for carrying out each mission.

The traverse hop can be done with a fixed attitude, fixed altitude maneuver, or can be performed with a ballistic maneuver. Inertial and surface relative measurements can be combined to estimate the hoppers position, velocity, and attitude during traverse.

To navigate steep slopes, a short-range active sensor can be used to maintain a safe distance between the vehicle and the steep surface. As the hopper traverses up or down the steep surfaces, it scans ahead to prepare for juts or crags in the surface ahead.

Crater exploration can be achieved using both a short-range LIDAR and passive optical camera. Knowing the morphology of the crater (simple or complex), the relationship between the diameter and depth of the crater, and understanding where the sun is and how shadows are cast within craters, a hopper can navigate within a crater. The short-range LIDAR can be used to estimate relative slope between the vehicle and the surface, and use it to estimate its radial location within the crater. Tracking the terminator of the shadow cast by the limb of the crater allows the vehicle to estimate the azimuth location within the crater.

6.1.2 Method for Safe Landing Area Selection using a Passive Camera

The Size Density Method (SDM) was developed in this thesis to pick the safest landing area within a landing region. The method uses the size and number of features as a corollary to determine relative safety between different landing areas. A site is relatively safer than the other sites in the landing area if it has both fewer and smaller features. This method can be used from long ranges and low path angles to help point the hopper towards an area that is more likely to have a safe landing aim point within the landing site.

The method for site selection using feature detection from images gathered with a passive camera is limited by lighting conditions. Their effects must be taken into account for each hop. However, the mission design can be used to optimize the ability of the hopper to detect features by keeping the sun and viewing angles appropriately adjusted for maximum detectability of features.

6.1.3 Method for Landing Aim Point Selection at Short Range using an Active Range Sensor

The Size Density Method can be coupled with a method for detecting local slope and roughness at the landing site using sparse detections. Using a short-range LIDAR, the surface can be interrogated to estimate the relative slope of the surface with respect to the vehicle. Points on the surface create a sparsely populated digital elevation map that is used to estimate the local surface relative attitude. Once a relative slope is estimated, it can be used to determine the “un-rough” surface. The same measurements taken by the range sensor can be used to understand the deviations from the “un-rough” surface and give an estimate of the roughness of the surface. Slope and roughness can be attributed to the ability of the vehicle to withstand hazards. Once a vehicle has detected a landing aim point within the landing site that is within hazard tolerances, it can safely land.

The Sparse Slope & Roughness (SSR) method demonstrates that a small, short-range LIDAR can be used to provide landing aim point selection at low altitudes near landing.

6.1.4 Combined Landing Area and Landing Aim Point Selection (SDM and SSR)

A concept of operations for the selection of a safe landing aim point during a traverse hop has been developed using a method for landing area coupled with landing aim point selection. A full tradespace across the SDM and SSR is studied and the final safe landing percentage over 35,860 separate landing simulations resulted in 100% safe landings.

This is a powerful result showing that the concept of operations and methods developed in this thesis enable a low mass, low power, low computational solution for hopper safe landing.

6.2 Future Work

Future work involves a progression of development and testing to eventually mature and fly a hopper mission on another planetary body. The prospects of doing this are not in the too distant future. Many of the sensors and algorithms have been described in this thesis and the listed references. The body of work is currently being combined to generate high fidelity simulations, with the goal of demonstrations on terrestrial vehicles. Once this has been successful, the complete hopping concept will have matured to TRL6 (system demonstration in a relevant environment) and will be ready for a planetary mission.

6.2.1 Navigation

Navigation analysis of hopper architectures has been described in the literature (37)(53), but demonstration of several of the concepts has not been performed in depth: ultra-precise landing methodology (41), localization (132), steep slope traverse, and crater exploration.

The ultra-precise landing mission scenario can be studied in much greater depth. Preliminary analysis has shown the control authority (33), navigation error (37)(53) and delta-V costs (30)(54) of various hopper configurations. A detailed analysis has not been done to show the gain in precision, delta-V costs and overall mass and complexity differences between a mission attempting to land precisely from orbit and one that uses coarse sensors to hop to ever-more precise planetary locations. Based on current technology for precise orbital landing, estimates of the global landing precision are on the order of 100 meters (133)(134). Hopper navigation is capable of 1 to 10 meter hop precision (based on range traveled, onboard map quality from orbital reconnaissance and onboard sensor quality) (37)(53). With this basic measure, it can be seen that gaining precision through multiple landings has high potential for providing gains in overall global landing precision of a lander or hopper.

The localization problem for space has been studied for rovers on Mars (72)(73) but, from the literature review, it does not seem to have been implemented in a real-time self-contained system. Development of the methodology and real-time demonstration would be a powerful tool for localization while sitting on the planetary surface (between hops), as well as demonstrating a technique to use surface features, with the sun and stars to enable planetary localization during traverse on a real-time platform.

Steep slope and crater exploration navigation methods can be expanded upon to better understand the precision and delta-V trades for performing these types of missions with a hopper.

Current test systems include Earth-demonstrators that can be used for landing or hopping technology development (32)(135)(136)(137). Some of these testbeds are commercially built and owned, while others have been developed directly by NASA. Future work would include use of these systems to study the different architectures and methods described in this thesis over a representative terrain.

6.2.2 Site Selection and Hazard Detection

Further improvements in the algorithm for the Size Density Method can come from studying the coupling between system hardware. A study in optical cameras that could be used onboard to provide the best dynamic range, field-of-view, and pixel resolution to provide the best performance and speed when coupled with the algorithm and mission design, would be a step closer to the development of a space-based system.

The site selection, coupled with slope and roughness detection algorithms, have been tested in simulation and with simple laboratory setups in the work done for this thesis. Future work would involve developing a real-time system that includes an optical camera and range sensor, and to test it with real hardware and software on a planetary-like landscape. A planetary-like landscape (with craters and proper lighting conditions) is difficult to find on Earth, but representative landscapes can be created in the laboratory or on a small scale at an outdoor test range.

6.3 Final Remarks

The basis of much of this work has come from work and discussions on lunar landing. The Google Lunar X-Prize (82) was announced and MIT's team developed the hopping concept for completion of the surface mission. There were many aspects of lunar/Mars landing, as well as rover traverse, that were applicable to this problem, but there were several aspects of the mission that made navigation and site selection of the hopper traverse mission unique.

As has been described, hoppers are propulsive mobility vehicles. Thus, the more mass fraction that can be applied to propellant, the longer missions can be. Hoppers also fly in a trajectory regime that falls between landing from orbit and traversing on the surface. They are low flying, rapidly traversing vehicles meant to quickly locate from one landing area to another, or to traverse into and over hazardous areas (such as cliffs, rock fields, or craters). Unlike rovers, they do not enjoy the benefit of being able to stop mid-traverse and compute a new navigation solution for the next destination. Hoppers must make decisions during flight and thus faster autonomous methods are needed to help enable these missions.

The basis of this thesis was to apply the work done on landing and roving to the hopper problem, and also add useful new methods that would enable the hopper mission scenarios. The desire to carry less mass and reduce computational workload, while also maintaining safety and precision in the hopper mission scenarios, led to the ideas presented in this thesis. Passive optical cameras and short-range LIDARs enable many of the detections needed for safe landing. From the literature, algorithms that attempted to directly image hazards required high amounts of processing and were not easy to implement on a real-time flying spacecraft.

In the future, advanced sensors, such as Flash LIDARs (97) will be flown in space and used for assessing safe planetary landing. Even with those very precise techniques, there is still a place for performing evaluation of landing areas upon approach (from orbit or during a hop traverse) that will always be difficult for active, range-limited sensors. The Size Density Method provides a method to perform site selection using an algorithm with low computational overhead and requiring only a passive optical sensor. This is limited by lighting conditions, but provides advantages in being able to detect over long ranges and shallow path angles. In the future, the passive optical and active high precision techniques can be combined to make for an even better solution to this problem.

Slope and roughness detection using a short-range LIDAR is an adaptation of solving the problem during descent using a Flash LIDAR (57). The benefits of using a short-range single beam range sensor are that the sensor is simpler and smaller. Such a sensor has been built and flown in space as early as Apollo (138) and such sensors are actively used for docking with the International Space Station (139) and for science missions (140)(141). A short-range LIDAR can be built small, and with low power, and can be gimballed or use a steering mirror to create a low mass scanning LIDAR that can be used onboard a hopper for slope and roughness detection.

The concepts in this thesis can be applied to lunar and Martian missions, but are also applicable for atmosphere-less, rocky, and cratered planetary bodies that have not been visited yet. The concepts work without any a priori knowledge of the planetary surface that is being visited. There are dozens, if

not more, bodies in our solar system that could be visited by hoppers (20). A low mass, low power, low computational method of safely and precisely traversing from one landing location to another can be enabled by the concepts in this thesis.

6.4 Acknowledgements

I would like to thank my committee members for all they have done for me: Professor Miller, for providing the tenants that I followed in developing a research idea and thesis, and all his advice in shaping my work; Professor deWeck, for believing in me and giving me the opportunity to return to MIT for a doctorate; Tye Brady for all the opportunities that have been given to me and his mentorship through them; and Professor Hoffman, for all the hours spent discussing my work, enabling opportunities, and mentorship through the past several years.

I'd like to thank Andrew Johnson at JPL, and Brett Streetman at Draper for taking the time and effort to help me improve the thesis.

I would like to thank all the students I have worked with the past several years on the TALARIS project, especially Phillip, Farah, Akil, ChrisH, Sarah, ChrisR, Joe, Ted, and Simran for all the hard work they put in the lab and the successes and failures we had together.

I would like to thank Draper Laboratory, for enabling me to get my doctorate while working, and to my colleagues for being supportive through the process. I'd especially like to thank Brett, Tom, and Mike for all the work they put in on hoppers the past several years, and the mentorship they have provided to all the students working on the project.

Finally, I'd like to thank my family for all the encouragement they have provided me these past few years. Most of all, I want to thank my wife, Laura, for being by my side through everything, and being so understanding of all the time I spent in my office trying to finish, instead of being at home, with her and our newborn, Lily!

Bibliography

1. **NASA.** *Surveyor Program Results.* 1969. NASA-SP-184.
2. —. Surveyor 6. *NSSDC ID: 1967-112A.* [Online] July 2012.
<http://nssdc.gsfc.nasa.gov/nmc/spacecraftDisplay.do?id=1967-112A>.
3. *The Lunar Pogo Stick.* **Seifert, H. S.** 1967 , *Journal of Space and Rockets*, pp. 941-943.
4. **Meetin, Ronald J. and Seifert, Howard S.** Propulsion Dynamics of Lunar Hoppers. *Journal of Spacecraft and Rockets.* 1974, pp. 852-856.
5. *Hopping Transporters for Lunar Exploration.* **Kaplan, Marshall H. and Seifert, Howard S.** 1969 , *Journal of Spacecraft and Rockets*, pp. 917-922.
6. *Dynamical Equations for the Plane Change Maneuver of the Lunar Hopping Laboratory.* **Kaplan, Marshall H.** 1970 , *Journal of Spacecraft and Rockets*, pp. 491-493.
7. *Comparison of Alternative Concepts for Lunar Surface Transportation.* **Apel, Uwe.** 1988 , *Acta Astronautica*, pp. 445-456.
8. *Lunar Lander Configuration Study and Parametric Performance Analysis.* **Donahue, Benjamin and Fowler, C. Robert.** Monterey, CA : s.n., 1993. 29th Joint Propulsion Conference. pp. AIAA-93-2354.
9. *High Autonomy Lunar Surface Mobility Systems.* **Vallerani, Ernesto, et al.** 2006. International Astronautical Conference. pp. IAC-06-A3.6.08.
10. *Mechanical Design of a Hopper Robot for Planetary Exploratio Using SMA as a Unique Source of Power.* **Montminy, Steve, Dupuis, Erick and Champlaud, Henri.** 2006. International Astronautical Conference. pp. IAC-06-C2.5.4.
11. *In Situ Propellant Production: The Key to Global Surface Exploration of Mars?* **Hoffman, S. J., Niehoff, J. C. and Stancati, M. L.** San Diego, CA : s.n., 1982. AIAA/AAS Astrodynamics Conference. pp. AIAA-82-1477.
12. *The Ballistic Mars Hopper: An Alternative Mars Mobility Concept.* **Sercel, J. C., Blandino, J. J. and Wood, K. L.** San Diego, CA : s.n., 1987. AIAA/SAE/ASME/ASEE 23rd Joint Propulsion Conference. pp. AIAA-87-1901.
13. *Diborance/CO2 Rockets for Use in Mars Ascent Vehicles.* **Zubrin, Robert.** San Diego, CA : s.n., 1995. 31st AIAA/ASME/SAE/ASEE Joint Propulsion Conference and Exhibit. pp. AIAA-95-2640.
14. *Methods for Achieving Long Range Mobility on Mars.* **Zubrin, Robert.** Nashville, TN : s.n., 1992. AIAA/SAE/ASME/ASEE Joint Propulsion Conference and Exhibit. pp. AIAA-92-3862.

15. *A Mars Rocket Vehicle Using In-situ Propellants*. **Landis, Geoffrey A., Linne, Diane L. and Taylor, David**. Huntsville, AL : s.n., 2000. 36th AIAA/ASME/SAE/ASEE Joint Propulsion Conference and Exhibit. pp. AIAA-2000-3120.
16. *Mars Rocket Vehicle Using In Situ Propellants*. **Landis, Geoffrey A. and Linne, Diane L.** 2001 , Journal of Spacecraft and Rockets, pp. 730-735.
17. *Mars Hopper versus Mars Rover*. **Shafirovich, Evgeny, Salomon, Michael and Gokalp, Iskender**. 2006 , Acta Astronautica, pp. 710-716.
18. **Maryland, University of**. Comet Hopper, a UMD/NASA Goddard Proposal, Moves to 'Final Round' in NASA Selection Process. [Online] 2011 11-May.
<http://www.newsdesk.umd.edu/scitech/release.cfm?ArticleID=2428>.
19. *Initial Development of an Earth-Based Prototype for a Lunar Hopper Autonomous Exploration System*. **Cunio, Phillip M**. Pasadena, CA : s.n., 2009. AIAA Space 2009. pp. AIAA-2009-6713.
20. *Options in the Solar System for Planetary Surface Exploration via Hopping*. **Cunio, Phillip M., et al**. Big Sky, MT : s.n., 2010. IEEE/AIAA Aerospace.
21. **Cunio, Phillip M**. *Tradespace Model for Planetary Surface Exploration Hopping Vehicles*. Massachusetts Institute of Technology. Cambridge, MA : s.n., 2012. PhD Thesis.
22. *Further Development and Flight Testing of a Prototype Lunar and Planetary Surface Exploration Hopper: Update on the TALARIS Project*. **Cunio, Phillip M. and al, et**. Anaheim, CA : s.n., 2010. AIAA Space.
23. *TALARIS Project Update: Overview of Flight Testing and Development of a Prototype Planetary Surface Exploration Hopper*. **Rossi, Christopher and al, et**. Cape Town, South Africa : s.n., 2011. International Astronautical Federation. pp. IAC-11.A3.2A.7.
24. *Shared Human and Robotic Landing and Surface Exploration in the Neighborhood of Mars*. **Cunio, Phillip M. and al, et**. Anaheim, CA : s.n., 2010. AIAA Space.
25. **Michel, Wendelin**. *Use and Sizing of Rocket Hoppers for Planetary Surface Exploration*. Massachusetts Institute of Technology. Cambridge, MA : s.n., 2010. SM Thesis.
26. **Yue, Howard K. and al, et**. *Integrated Model for a Cost Tradeoff Study Between a Network of Landers and Planetary Hoppers*. Massachusetts Institute of Technology. Cambridge, MA : s.n., 2010.
27. **Lanford, Ephraim R**. *Unique Abilities of Hopper Spacecraft to Enable National Objectives for Solar System Exploration*. Massachusetts Institute of Technology. Cambridge, MA : s.n., 2011. SM Thesis.
28. **Olthoff, Claas T**. *Application of Flexibility Principles and Strategies to the TALARIS Avionics System*. Technische Universitaet Muenchen. Munich, Germany : s.n., 2010. Diplomarbeit.

29. **Nothnagel, Sarah N.** *Development of a Cold Gas Propulsion System for the TALARIS Hopper.* Massachusetts Institute of Technology. Cambridge, MA : s.n., 2011. S.M. Thesis.
30. **Middleton, Akil J.** *Modeling and Vehicle Performance Analysis of Earth and Lunar Hoppers.* Massachusetts Institute of Technology. Cambridge, MA : s.n., 2010. S.M. Thesis.
31. **Han, Christopher J.** *Development of Modular Real-Time Software for the TALARIS Lunar Hopper Testbed.* Massachusetts Institute of Technology. Cambridge, MA : s.n., 2011. S.M. Thesis.
32. *Demonstration of a Safe & Precise Planetary Landing System On-board a Terrestrial Rocket.* **Paschall, Stephen and Brady, Tye.** Big Sky, MT : s.n., 2012. IEEE Aerospace Conference.
33. **Morrow, Joseph M.** *Design and Analysis of Lunar Lander Control System Architectures.* Massachusetts Institute of Technology. Cambridge, MA : s.n., 2012. S.M. Thesis.
34. **Steiner, Theodore J.** *Design and Analysis of a Navigation System for Planetary Hopping Vehicles.* Massachusetts Institute of Technology. Cambridge, MA : s.n., 2012. S.M. Thesis.
35. *Self Contained Method for Safe & Precise Lunar Landing.* **Paschall, Stephen C., Brady, Tye M. and Sostaric, Ron A.** Big Sky, MT : s.n., 2008. IEEE Aerospace Conference. p. 1643.
36. *Lunar Landing and Ascent Trajectory Guidance Design for the Autonomous Landing and Hazard Avoidance Technology (ALHAT) program.* **Fill, Thomas.** 2010. AAS GNC Conference. pp. AAS 10-257.
37. *Small Lunar Lander/Hopper Navigation Analysis using Linear Covariance.* **Huxel, Paul and Cohanim, Babak E.** Big Sky, MT : s.n., 2010. IEEE Aerospace Conference. p. 1091.
38. **Ambrose, William A. and Williams, D. A.** *Recent Advances and Current Research Issues in Lunar Stratigraphy.* Boulder, Colorado : Geological Society of America, 2011.
39. **Borg, Lars, Des Marias, David and Beaty, David W.** *Science Priorities for Mars Sample Return.* Lawrence Livermore National Laboratory. 2008. MEPAG Next Decade Science Analysis Group.
40. **Rochette, Pierre, Weiss, Benjamin P. and Gattacceca, Jerome.** *Magnetism of Extraterrestrial Materials.* Mineralogical Society of America. 2009.
41. *Small Lunar Exploration and Delivery System.* **Cohanim, Babak E.** Pasadena, CA : s.n., 2009. AIAA Space Conference. pp. AIAA-2009-6712.
42. **JPL, NASA.** *Flight Projects - Mars Exploration Rovers.* [Online] <http://www-robotics.jpl.nasa.gov/projects/MER.cfm?Project=1>.
43. **Jaffe, Leonard D.** *The Surveyor Lunar Landings.* *Science.* 1969 May, Vol. 164, 3881, pp. 775-788.
44. *Autonomous Landing and Hazard Avoidance Technology (ALHAT).* **Epp, Chiold D., Robertson, Edward A. and Brady, Tye M.** Big Sky, MT : s.n., 2008. IEEE Aerospace Conference. p. IEEEAC #1644.

45. **NASA.** *Mars Pathfinder*. [Online] http://www.nasa.gov/mission_pages/mars-pathfinder/.
46. **Laboratory, Jet Propulsion.** *Mars Exploration Rovers*. [Online] <http://www.jpl.nasa.gov/missions/mer/>.
47. *Two years of Visual Odometry on the Mars Exploration Rovers*. **Maimone, Mark, Cheng, Yang and Matthies, Larry.** 3, 2007 Mar, Journal of Field Robotics, Vol. 24, pp. 169-186.
48. *Taking the Next Giant Leap*. **Cohanim, Babak E.** Breckenridge, CO : s.n., 2010. AAS GNC Conference. pp. AAS 10-061.
49. *Small Lunar Lander/Hopper Performance Analysis*. **Middleton, Akil, Paschall, Stephen C. and Cohanim, Babak E.** Big Sky, MT : s.n., 2010. IEEE Aerospace Conference. p. 1160.
50. *Lunar Radio Array (LRA)*. **Lazio, J., et al.** 2009. UV/Optical/IR Space Telescopes: Innovative Technologies and Concepts IV. Proceedings of SPIE. Vol. 7436.
51. *Apollo Looking Forward: Crew Task Challenges*. **Major, Laura M., Brady, Tye M. and Paschall, Stephen C.** Big Sky, MT : s.n., 2009. IEEE Aerospace Conference. p. IEEEAC #1149.
52. *The Challenge of Safe Lunar Landing*. **Brady, Tye M. and Paschall, Stephen C.** Big Sky, MT : s.n., 2010. IEEE Aerospace Conference. p. IEEEAC #1177.
53. *Talaris Hopper Testbed Navigation Analysis*. **Huxel, Paul and Cohanim, Babak E.** Big Sky, MT : s.n., 2011. IEEE Aerospace Conference. p. 1325.
54. *Development and Deployment of a Performance Model for the Prototype Planetary Exploration Hopper*. **Middleton, Akil and Paschall, Stephen.** Big Sky, MT : s.n., 2011. IEEE Aerospace Conference.
55. *New Platforms for Science on the Lunar Surface*. **Cohanim, Babak E., et al.** NASA Ames Research Center : s.n., 2011. Lunar Science Forum.
56. *Lidar-based Hazard Avoidance for Safe Lunar Landing on Mars*. **Johnson, Andrew E., et al.** 6, 2002 , Journal of Guidance, Control, and Dynamics, Vol. 25, pp. 1091-1099.
57. *Analysis of On-Board Hazard Detection and Avoidance for Safe Lunar Landing*. **Johnson, Andrew E.** Big Sky, MT : s.n., 2008. IEEE Aerospace Conference. p. 1091.
58. *Real-time Landing Point Redesignation (LPR) Algorithm*. **Cohanim, Babak E. and Collins, Brian K.** 2008. AIAA GNC Conference.
59. *Landing Point Designation Algorithm for Lunar Landing*. **Cohanim, Babak E. and Collins, Brian.** 4, 2009 July-August, AIAA Journal of Spacecraft and Rockets, Vol. 46, pp. 858-864.
60. *Real-time Hazard Detection for Landers*. **Huertas, Andres, Cheng, Y. and Matthies, L. H.** Adelphi, MD : s.n., 2007. NASA Science Technology Conference.

61. *Passive Imaging Based Multi-cue Hazard Detection for Spacecraft Safe Landing*. **Huertas, Andres, Cheng, Y. and Madison, Richard**. Big Sky, MT : s.n., 2006. IEEE Aerospace Conference.
62. **Huertas, Andres, Johnson, Andrew E. and Werner, Robert A.** Performance Evaluation of Hazard Detection and Avoidance Algorithms for Safe Lunar Landings. Big Sky, MT : s.n., 2010 . p. IEEEAC 1662.
63. *Stereo Vision and Shadow Analysis for Landing Hazard Detection*. **Matties, L.** 2008. IEEE International Conference on Robotics and Automation.
64. *Landing Site Selection using Fuzzy Rule-Based Reasoning*. **Serrano, N. and Seraji, H.** 2007. IEEE International Conference on Robotics and Automation.
65. **Rivellini, T.** Challenges of Landing on Mars. *National Academy of Engineering*. 2004 , Vol. 34.
66. *Hazard Detection Methods for Lunar Landing*. **Brady, Tye M.** Big Sky, MT : s.n., 2008. IEEE Aerospace Conference. p. IEEEAC #1087.
67. *Lunar Surface Navigation*. **Trexler, T. T. and Odden, R. B.** 6, 1966 Nov, Supplement to IEEE Transactions on Aerospace and Electronic Systems, Vols. AES-2.
68. *Overview of Terrain Relative Navigation Approaches for Precise Lunar Landing*. **Johnson, Andrew E. and Montgomery, James F.** Big Sky, MT : s.n., 2008. IEEE Aerospace Conference. p. 1657.
69. *Passive Optical Terrain Relative Navigation using APLNav*. **Adams, D., Criss, T. B. and Shankar, U. J.** Big Sky, MT : s.n., 2008. IEEE Aerospace Conference. p. IEEEAC #1646.
70. *Optical Landmark Detection for Spacecraft Navigation*. **Cheng, Y., et al.** 2002. AAS GNC Conference. pp. AAS 02-224.
71. *Ground Mobility Systems for Planetary Exploration*. **Fiorini, P.** San Francisco, CA : s.n., 2000. Robotics and Automation Conference.
72. *Robot Localization using a Computer Vision Sextant*. **Cozman, F. and Krotkov, E.** 1995. IEEE International Conference on Robotics and Automation.
73. *Automatic Mountain Detection and Pose Estimation for Teleoperation of Lunar Rovers*. **Cozman, F. and Krotkov, E.** Albuquerque, NM : s.n., 1997. IEEE Conference on Robotics and Automation.
74. *Over-the-Horizon Autonomous Rover Navigation*. **Dupuis, E.** 2007. Experimental Results, CSA.
75. *Combined Optic-Flow and Stereo-Based Navigation of Urban Canyons for a UAV*. **Hrabar, S.** 2005. IEEE International Conference on Intelligent Robots and Systems.
76. *Mars Rover Navigation Results Using Sun Sensor Heading Determination*. **Volpe, R.** 1999. IEEE/RSJ International Conference on Intelligent Robots and Systems.
77. *Titan Airship Explorer*. **Hall, J. L.** 2002. IEEE Aerospace Conference.

78. *Mars Airplane Guidance and Navigation*. **Brand, T., Tao, Y. C. and Norris, L.** 2003. 2nd AIAA "Unmanned Unlimited" Systems, Technologies, and Operations. pp. AIAA-2003-6608.
79. **Brady, Tye.** *Operational Concept for the Autonomous Landing and Hazard Avoidance Technology (ALHAT) System*. NASA. 2008.
80. *Lunar Landing Trajectory Design for Onboard Hazard Detection & Avoidance*. **Paschall, Stephen, et al.** 2009. 32nd Annual AAS Guidance and Control Conference. AAS 09-097.
81. *Approach Phase deltaV Considerations for Lunar Landing*. **Cohanin, Babak E., et al.** Big Sky, MT : s.n., 2009. IEEE Aerospace Conference. IEEEAC paper #1195.
82. **X-Prize Foundation.** *Google Lunar X-Prize*. [Online] <http://www.googlelunarxprize.org/>.
83. **NASA.** *LUNAR IMPACT, A History of Project Ranger*. [Online] 2006 Nov. http://history.nasa.gov/SP-4210/pages/Cover.htm#C_Top.
84. —. *Hiten*. [Online] 2012 May. <http://nssdc.gsfc.nasa.gov/nmc/spacecraftDisplay.do?id=1990-007A>.
85. **ESA.** *Set your own course for the stars*. [Online] 2002 November. http://www.esa.int/esaCP/ESANR77708D_Expanding_0.html.
86. **Organisation, India Space Research.** *Chandrayaan-1 Spacecraft Description*. [Online] 2008 November. http://www.isro.org/chandrayaan/htmls/spacecraft_description.htm.
87. **NASA.** *Luna 9*. [Online] 2012 May. <http://nssdc.gsfc.nasa.gov/nmc/spacecraftDisplay.do?id=1966-006A>.
88. —. *NASA Surveyor Program*. [Online] 2012 May. <http://nssdc.gsfc.nasa.gov/nmc/spacecraftDisplay.do?id=1966-045A>.
89. —. *Soviet Union Lunar Rovers*. [Online] 2010 March. http://www.nasa.gov/mission_pages/LRO/multimedia/lroimages/lroc-20100318.html.
90. *Navigation Flight Operations for Mars Pathfinder*. **Vaughan, Robin M., et al.** 1998. AAS 98-145.
91. **NASA.** *Phoenix Mars Mission*. [Online] <http://phoenix.lpl.arizona.edu/phases04.php>.
92. **JPL, NASA.** *Mars Science Laboratory - Mission - Eyes and Other Senses*. [Online] <http://marsprogram.jpl.nasa.gov/msl/mission/rover/eyesandother/>.
93. —. *MFEX: Microrover Flight Experiment - Control and Navigation Subsystem*. [Online] 1997 February. <http://mars.jpl.nasa.gov/MPF/roverctrlnav/rovercntrlnav.html>.
94. *The Lunar Opposition Surge: Observations by Clementine*. **Buratti, Bonnie J., Hillier, John K. and Wang, Michael.** 2, s.l. : Icarus, 1996 , Vol. 124.

95. **Kumar, Ganesh.** *Development and Characterization of Surface Relative Attitude Sensor System for a Hopper Mobility Scheme using Laser Altimeters.* International Space University. Cambridge, MA : s.n., 2010. M.Sc Thesis.
96. *MER-DIMES: A Planetary Landing Application of Computer Vision.* **Cheng, Yang, Johnson, Andrew and Matthies, Larry.** 2005. IEEE Computer Society Conference on Computer Vision and Patter Recognition.
97. *Lidar systems for precision navigation and safe landing on planetary bodies.* **Amzajerdian, Farzin, et al.** Beijing, China : s.n., 2011. International Symposium on Photoelectronic Detection and Imaging 2011.
98. *Flight test performance of a high precision navigation Doppler Lidar.* **Pierrottet, Diego, et al.** 2009. Laser Radar Technology and Applications XIV, Proc. of SPIE Vol. 7323.
99. *Navigation Doppler lidar sensor for precision altitude and vector velocity measurements: flight test results.* **Pierrottet, Diego, et al.** Orlando, FL : s.n., 2011. Sensors and Systems for Space Applications IV, Proc of SPIE 8044.
100. *Coherent Doppler Lidar for Precision Navigation of Spacecrafts.* **Amzajerdian, Farzin, et al.** Long Beach, CA : s.n., 2011. 16th Coherent Laser Radar Conference.
101. *Fiber Doppler Lidar for Precision Navigation for Space Vehicles.* **Amzajerdian, Farzin, et al.** San Diego, CA : s.n., 2012. Fiber Lasers and Applications.
102. *Fiber-based Coherent Doppler Lidar for Precision Landing on the Moon and Mars.* **Amzajerdian, Farzin, et al.** Istanbul, Turkey : s.n., 2011. Fiber Laser Applications.
103. *Doppler lidar sensor for precision landing on the Moon and Mars.* **Amzajerdian, Farzin, et al.** Big Sky, MT : s.n., 2012. IEEE Aerospace Conference.
104. *Analysis and Testing of a LIDAR-Based Approach to Terrain Relative Navigation for Precise Lunar Landing.* **Johnson, Andrew E. and Ivanov, T.** 2011. AIAA Guidance, Navigation, and Control Conference.
105. **de Pater, Imke and Lissauer, Jack J.** *Planetary Science.* Cambridge : Cambridge University Press, 2001.
106. **Hamilton, Calvin J.** *Terrestrial Impact Craters.* [Online] 2001 .
<http://www.solarviews.com/eng/tercrate.htm>.
107. **NASA.** JSC Digital Image Collection. [Online]
<http://www.hq.nasa.gov/office/pao/History/alsj/a410/AS10-29-4324.jpg>.
108. **Gonzalez, Rafael C. and Woods, Richard E.** Image Segmentation: Thresholding. *Digital Image Processing.* Upper Saddle River, New Jersey : Prentice Hall, 2002, 10, pp. 595-611.
109. *A Threshold Selection Method from Gray-Level Histograms.* **Otsu, Nobuyuki.** 1, 1979 , IEEE Transactions on Systems, Man, and Cybernetics, Vol. 9, pp. 62-66.

110. **Wertz, James R. and Larson, Wiley J.** *Space Mission Analysis and Design (SMAD)*. 3rd Edition. El Segundo, CA : Microcosm, 1999.
111. **Haralick, Robert M. and Shapiro, Linda G.** *Computer and Robot Vision*. Boston, MA : Addison-Wesley, 1992.
112. *Robust Horizon Finding Algorithm for Real-Time Autonomous Navigation based on Monocular Vision*. **Neto, A. Miranda, et al.** Washington, D.C. : s.n., 2011. 14th International IEEE Conference on Intelligent Transportation Systems.
113. **The Mathworks, Inc.** *bwconncomp*. [Matlab Function] 2008, rev1.1.6.2 .
114. **Arizona State University.** Lunar Reconnaissance Orbiter Camera. [Online] <http://www.lroc.asu.edu/>.
115. **JAXA.** *Kaguya (SELENE)*. [Online] 2007 November. http://www.jaxa.jp/press/2007/11/20071107_kaguya_e.html.
116. *What shadows reveal about object structure*. **Kriegman, David J. and Belhumeur, Peter N.** 8, 2001 August, Journal of Optical Society of America, Vol. 18, pp. 1804-1813.
117. **Kulling, Karl Christian.** *Optimal and Receding-Horizon Path Planning Algorithms for Communciaions Relay Vehicles in Complex Environments*. Massachusetts Institute of Technology. Cambridge, MA : s.n., 2007. SM Thesis.
118. **NASA - Goddard Space Flight Center.** MOLA-2 Instrument Specification. [Online] <http://tharsis.gsfc.nasa.gov/spec.html>.
119. *Initial Mars Orbiter Laser Altimeter (MOLA) Measurements of the Mars Surface and Atmopshere*. **Abshire, James B., Sun, Xiaoli and Afzal, Robert S.** s.l. : NASA Technical Report Server, 1998. Nineteenth International Laser Radar Conference. 19980236815.
120. **NASA - Goddard Space Flight Center.** Planetary Laser Altimety - LOLA. [Online] <http://tharsis.gsfc.nasa.gov/LOLA/lola.php>.
121. *Lunar Reconnaissance Orbiter Overview: The Instrument Suite and Mission*. **Chin, Gordon and al., et.** s.l. : Space Science Review, 2007 , Vol. 129, pp. 391-419.
122. **John Hopkins - Applied Physics Laboratory.** Messenger - Mercury Laser Altimeter (MLA). [Online] <http://messenger.jhuapl.edu/instruments/MLA.html>.
123. —. Mercury Laser Altimeter (MLA). *Education and Public Outreach*. [Online] <http://messenger-education.org/instruments/mla.php>.
124. —. *NEAR Laser Rangefinder - Specifications*. 1998. http://near.jhuapl.edu/fact_sheets/NLR.pdf. 98-9349.

125. **Velodyne**. *High Definition LIDAR: HDL-32E*. 2012. 97-0038c.
126. **Acuity**. *Acuity - AR3000 manual*. 2009.
127. *Stable Deconvolution of Noisy LIDAR Signals*. **Harsdorf, Stefan and Reuter, Rainer**. Dresden, FRG : s.n., 2000. Proceedings of EARSeL-SIG-Workshop LIDAR.
128. **Bowman-Cisneros, Ernest and Eliason, Eric**. *LROC RDR Data Products Software Interface Specification*. 2008.
129. **Golombek, M. and Rapp, D**. Size-frequency distributions of rocks on Mars and Earth analog sites: Implications for future landed missions. *Journal of Geophysical Research and Planets*. 1997 , Vol. 102, E2, 4117-4129.
130. **Ivanov, B. A., et al**. *The Comparison of Size-Frequency Distributions of Impact Craters and Asteroids and the Planetary Cratering Rate*. s.l. : Lunar and Planetary Institute.
131. *Size frequency distribution of small craters on the Moon*. **Trey, B., et al**. 2011. EPSC-DPS2011-808.
132. *Map-Based Localization using the Panoramic Horizon*. **Stein, Fridtjof and Medioni, Gerard**. Nice, France : s.n., 1992. International Conference on Robotics and Automation.
133. *Linear Covariance Analysis for Lunar Powered Descent and Landing Navigation*. **Geller, D**. 2007. AAS 07-055.
134. *Precision Descent Navigation for Landing at the Moon*. **DeMars, Kyle J. and Bishop, Robert H**. 2007. AAS 07-314.
135. *Morpheus Lander Testing Campaign*. **Hart, Jeremy J. and Mitchell, Jennifer D**. Big Sky, MT : s.n., 2012. IEEE/AIAA Aerospace Conference.
136. *Exploring the Benefits of Commercial Robotic Lander Testbeds*. **Ake, Colin, et al**. Big Sky, MT : s.n., 2012. IEEE/AIAA Aerospace Conference.
137. *Robotic Lunar Landers for Science and Exploration*. **Chavers, D. G. and al, et**. 2010. International Planetary Probe Workshop 7, p412.
138. **Sjoren, William L**. *Apollo Laser Altimeter Analysis*. NASA JPL. January, 1975. S-216.
139. *Rendezvous Lidar Sensor system for Terminal REndezvous, Capture, and Berthing to the International Space Station*. **Allen, Andrew C.M. and al, et**. 2008. Proc. of SPIE Vol. 6958.
140. *Optical system design and integration of the Lunar Orbiter Laser Altimeter*. **Ramos-Izquierdo, Luis and al, et**. 16, 2009 June, Optical Society of America, Vol. 48, pp. 3035-3049.
141. *The Mars Observer Laser Altimeter Investigation*. **Zuber, M. T**. E5, 1992 February, Journal of Geophysical Research, Vol. 97, pp. 7781-7797.

142. **Hillier, John K., Buratti, Bonnie J. and Hill, Kathryn.** Multispectral Photometry of the Moon and Absolute Calibration of the Clementine UV/Vis Camera. *Icarus*. 1999 , Vol. 141, 2.

Appendix A – Surface Image Rendering

To properly assess the Size Density Method, precise control of the lighting and viewing angles is required. This appendix describes the method used to create rendered surface images with controlled lighting and view angles. The rendered surface is compared against a real photograph of a lunar image to validate the ability of the rendering algorithm to properly reflect a realistic surface.

Surface Shading and Shadowing Algorithm

The surface shading and shadowing algorithm uses the DEM to generate a properly lit 3D rendering of the surface. The simulation values for view-to-sun azimuth, sun elevation, and view angle elevation are taken in and used to properly place the light source and viewing perspective in the image.

The surface shading is done assuming a surface with lunar regolith coloring and reflectance properties. The lighting curves used are from Hillier 1999 (142), where the reflectance properties of the surface are given as a function of sun angle and observer view angle relative to the surface.

Shadowing occurs by running a tracing algorithm across the surface points. A vector is drawn from the surface point under evaluation, to the Sun. If the vector passes through the DEM, then the point is flagged as being under shadow. Figure 81 provides an illustration of the conditions that determine if a point on the surface is considered shadowed or not. The shadowing trace is run over every point on the DEM, traced back to the light source (which is assumed to be at infinity).

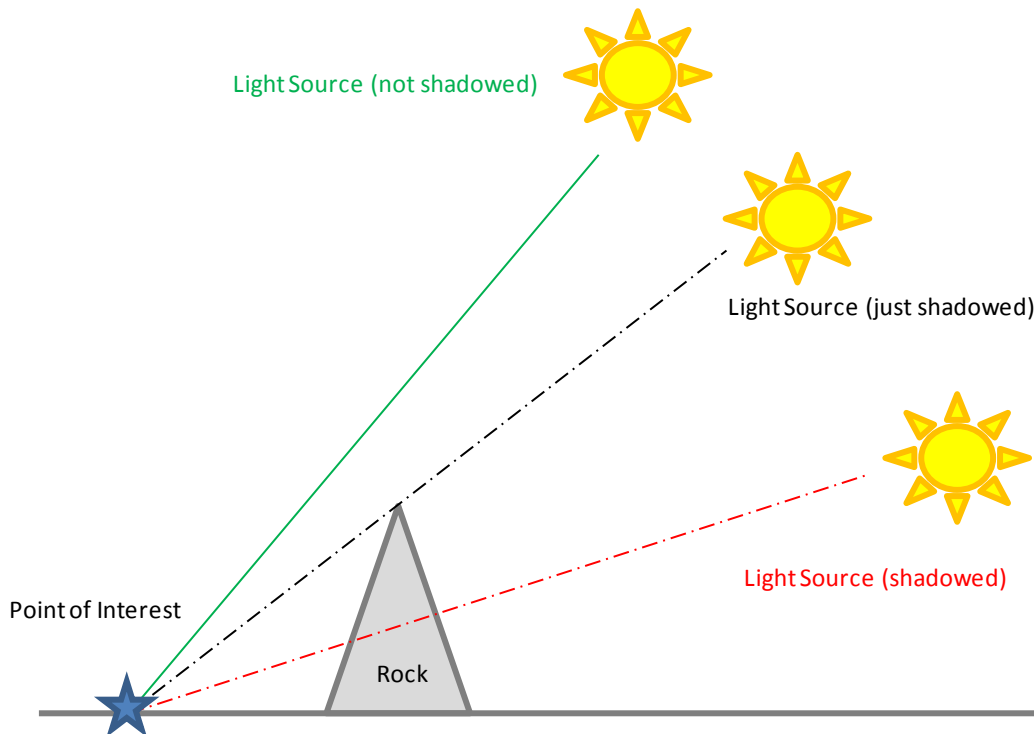


Figure 81 – Illustration of Shadowing Algorithm. If the vector from surface point under evaluation crosses through the DEM, that point is considered shadowed.

The identified shadowed points are determined and the shadowing is properly rendered onto the meshed surface. The view is adjusted to the desired view angle and the image is saved as an image file.

For traverse images, the meshed surface background is darkened (to simulate a dark sky, as would be seen on most planetary bodies of interest in our solar system), to create a proper horizon. The proper perspective and view elevation is given to the image by placing the observer view position and camera field of view properly. A simulated traverse image is given below in Figure 82.

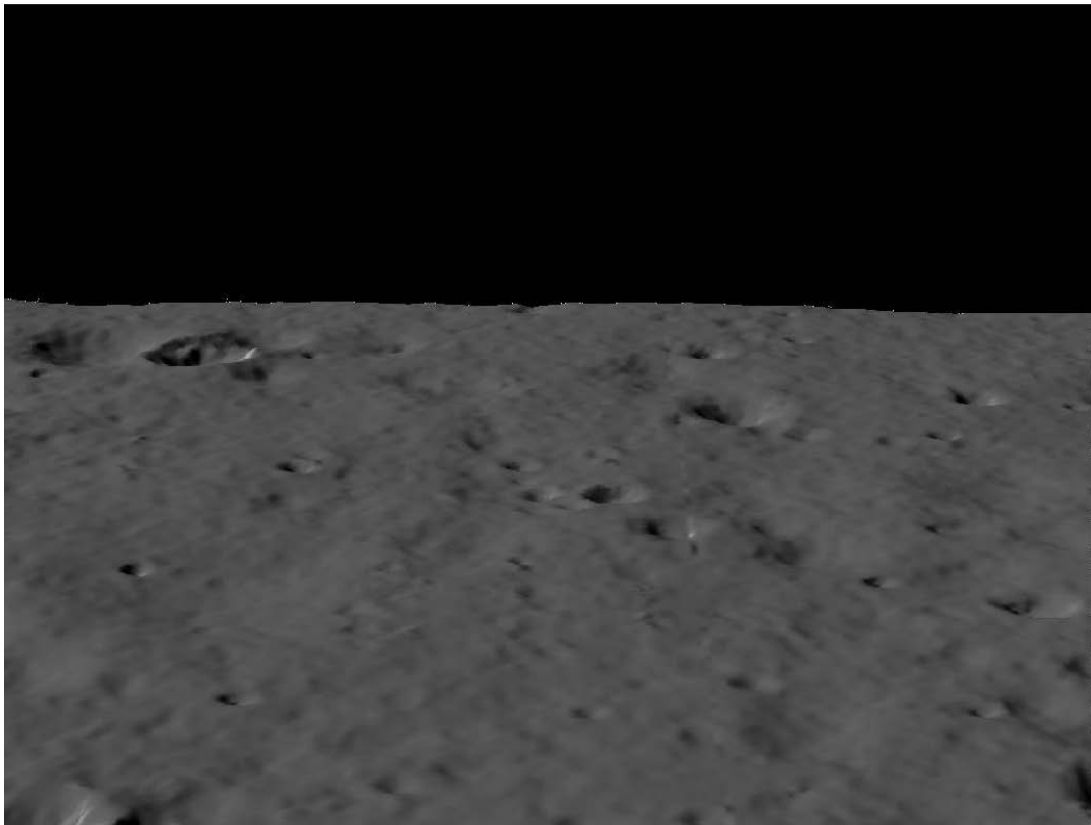


Figure 82 – Rendered traverse image of Luna 23/24 landing site

Validation of Surface Image Rendering

To validate the use of the rendered images, a comparison is done between a known lunar location with a photographed landing area and a rendered image of that landing area using an available LRO DEM (the Luna 23/24 landing region). For the analysis that needs to be done in this thesis, the variables of sun elevation, view elevation, and view-to-sun azimuth need to be controlled very precisely. The historical photographic data to assess lighting conditions for different sun and view angles does not exist for one spot on any planetary body, so the use of the rendered images enables detailed analysis to be performed in this thesis. The Size Density Method is concerned with detecting light and dark features as a representation of the hazard level for a given landing area. Even though the rendered image does not look exactly like the photograph, the features and shadows are well represented by the rendering. Comparing a photograph to the rendered image is used as validation to show that the algorithm

behaves similarly on the photograph and rendered image, and that the rendering technique applied to the DEMs can be used for further analysis.

The photograph is of the Luna 23 and 24 landings sites. This photograph has a corresponding LRO DEM (114) that can be used for further analysis of the rendered image against a more precise hazard detection method to statistically assess the ability of the Size Density Method to select landing areas.

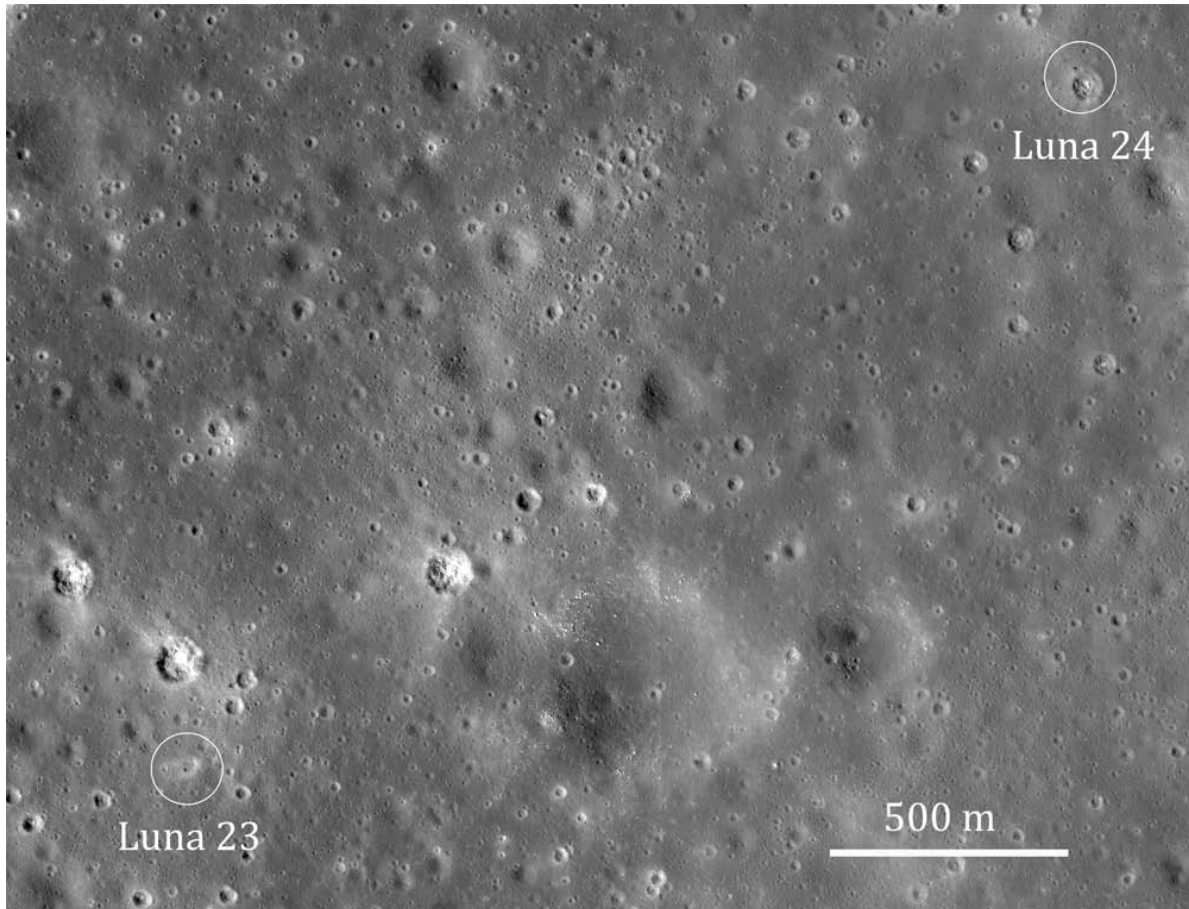


Figure 83 – Real image of the Luna 23/24 Landing Site (114)

The real photograph in Figure 83 has some interesting properties to note. The areas of lower elevation have darker Mare (the top-left corner of the map). Some of the craters also have a very high specular reflectance that is not captured in the Hillier models. There is also white text on the photograph that has not been removed so as not to alter the LRO photograph in any way. Very close inspection of the image also shows seams. The different areas of the photograph have slightly different mean values across seam boundaries. This is a very large area (2km x 2.5km) and is being used for comparison purposes to validate the rendering method. Single snapshots with one baseline camera setting are more beneficial for the SDM to function properly.

Figure 84 is the rendered version of the Luna 23/24 landing site with lighting conditions set to match that of the actual photograph in Figure 83 as closely as possible. The photographed surface image shows how the lunar Mare can vary in color. This was simulated in the rendered image as best as possible by

analyzing the photograph to understand the coloring characteristics of the flat Mare at different elevations and across seams. This correction was applied to the rendered image to give a better comparison of the photograph to the rendered image. Lower elevations are darker than higher elevations, which is typical on the large scale of the Moon, but difficult to characterize precisely, and is accentuated across the seams in the photograph.



Figure 84 – Rendered image of the Luna 23/24 Landing Site

Since the rendered image is created directly from the DEM (which has a resolution of 2m per pixel and 1m vertical resolution), not all features are caught. The bright reflectance seen in some of the craters is also not seen between the real and rendered image.

Figure 85 shows the real and rendered images, and their corresponding grayscale histograms. Both images have similar means and standard deviations. Both images also have values at 255 (bright white). The real image has text in it that was not removed and the rendered image has a white border around it (created in the saving process in Matlab). Both of these high value relics are filtered out during analysis.

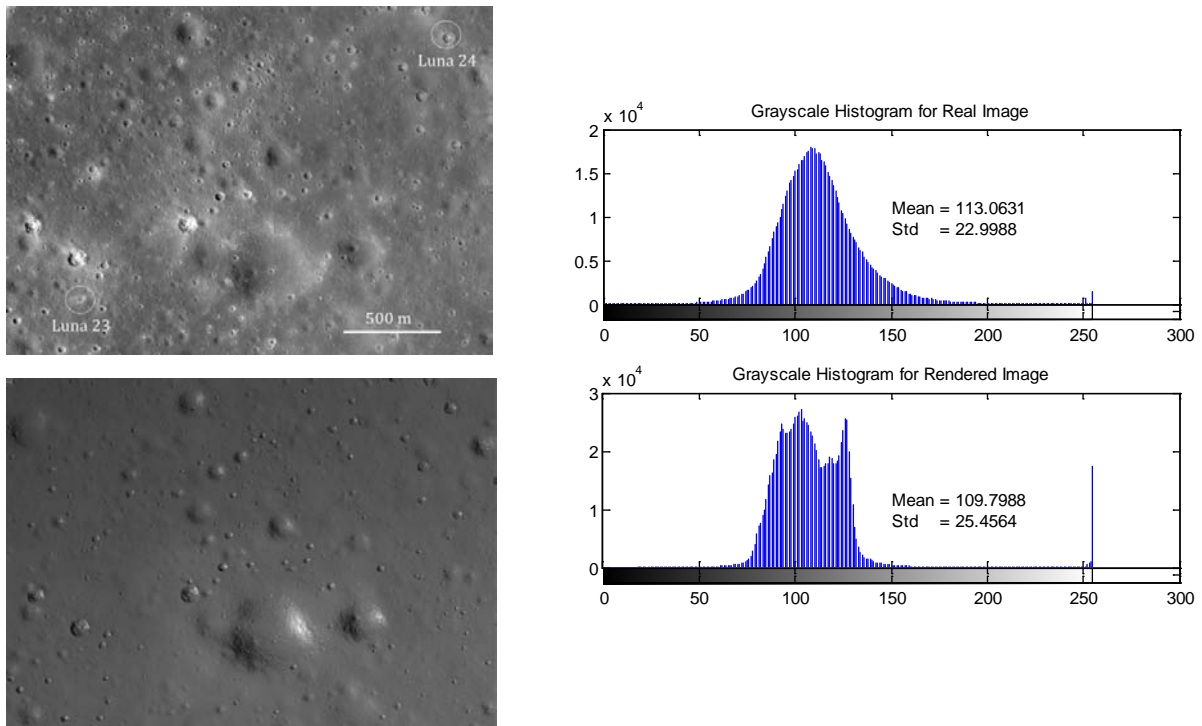


Figure 85 – Real and Rendered Image Histograms

The underlying LRO DEM that is used to create the rendered image in Figure 84 is given below in Figure 86. The DEM has 2 meter postings and is 941 x 1231 pixels (2km x 2.5km). The color bar shows the elevations in meters (1 meter vertical precision) and is referenced from a mean lunar radius (the values are negative, so this portion of the lunar surface is lower than the mean spherical radius).

This figure is the same as Figure 31, and is placed here again for reference.

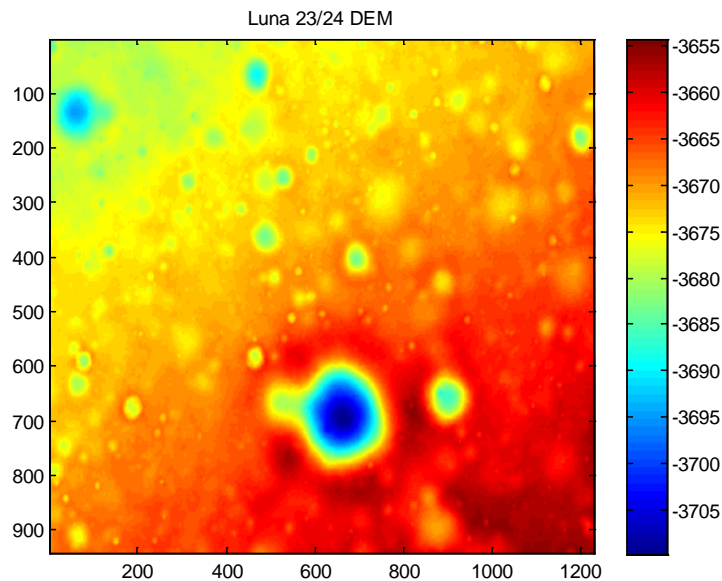


Figure 86 – Luna 23/24 DEM

The figures in Figure 87 show the DEM, rendered image, and real image weighted cost maps. The left image is the output of the modified DEM-based method on the DEM. The middle image is the output of the Size Density Method applied to the rendered image, showing the Weighted Cost Map. The right image is the output of the Size Density Method applied to the real image of the same location. As can be seen, the outputs of running the algorithm on the photograph and on the rendered image are similar, and compare well to identifying the major hazards in the DEM. The algorithm is designed to select landing areas that have relatively lower cost (areas of dark blue). Areas that have many and large features have the highest cost (redder in the spectrum).

To compare the relative costs between the methods and images, all factors were kept the same:

- N = 1 (weighting between feature size and density)
- 32x32 landing area grid
- Same Gaussian smoothing parameters (1σ normal distribution)

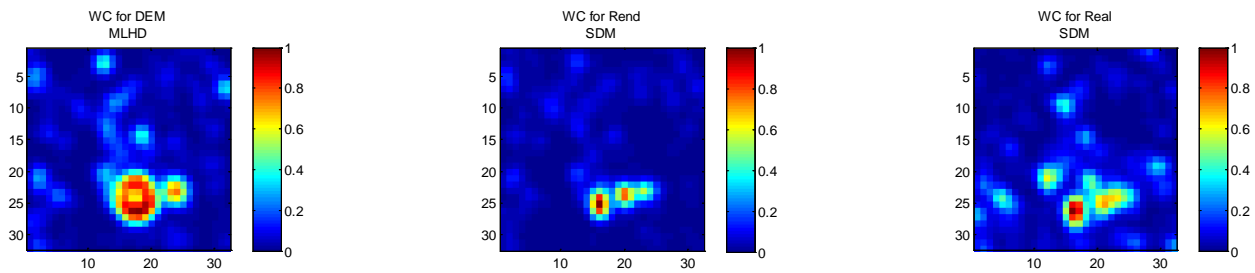


Figure 87 – DEM vs. Rendered vs. Real Weighted Cost Maps

The cost maps for both the photograph and the rendered image identify the major craters and give relatively low costs to areas with smaller and fewer craters. The area in the top left corner of the real image is darker (because of the Mare being darker at lower elevations) and is particularly difficult to model accurately in the rendered image. Because of this, the real image shows more features in the upper-left corner of the map, and thus the cost for landing in that area is higher.

Even though the cost maps are not exactly the same, the low cost areas (areas of darkest blue) overlap well. This can better be seen by overlaying the maps and assessing the relative cost between them.

Figure 88 shows the three maps compared in different ways. The left column of figures compares the SDM applied to both the rendered and real image. The middle column of figures compares the DEM modified DEM-based hazard detection method compared to the SDM for the rendered image. The right column of figures compares the modified DEM-based hazard detection method compared to the SDM for the real image.

The top row of figures shows the weighted cost maps compared and displayed as the costs given in each map, landing area by landing area. The x-axis represents the number of landing areas in the weighted cost map (1024 for a 32x32 cost map). The y-axis is the cost (0 having the best relative safety corresponding to blue areas in the weighted cost map, and 1 being the relatively most dangerous corresponding to the red areas in the weighted cost map). The x-axis is sorted by a given cost maps

landing area costs. The sort is done to show the monotonically increasing costs from one of the weighted cost maps (in the left and middle figure it is sorted on the rendered image's SDM weighted costs, in the right figure it is sorted on the real image's SDM weighted costs). The red dots are the corresponding costs for the weighted cost map of the LRO photograph (real image).

Each location on the x-axis is a landing area location in the weighted cost map, with the blue dot representing the cost derived from the Size Density Method, and the red dots being the same landing area location (coordinate-wise) from another weighted cost map.

The middle and bottom rows of figures overlays the weighted cost maps and differences them. The middle row shows the absolute values of the difference, while the bottom row shows the true differences between landing areas.

There is a good correlation between the landing areas that have low cost in the rendered image and the landing areas that have low cost in the real image. Some of the scatter can be attributed to misalignment between the photograph and rendered/DEM image (which is very difficult to align perfectly). Most of the scatter can be attributed to small differences in cost and rendering imperfections.

The SDM is good at detecting a majority of the hazardous areas identified by the MDM method. The large craters in the lower portion of the DEM are large and SDM detects both the dark and bright features that define the craters. The horizontal extent of the craters is captured well, but the vertical extent is not (since the sun is casting shadows from the left side of the image). Still, the method has no major outliers and the relative costs between the DEM, rendered, and real images is very comparable.

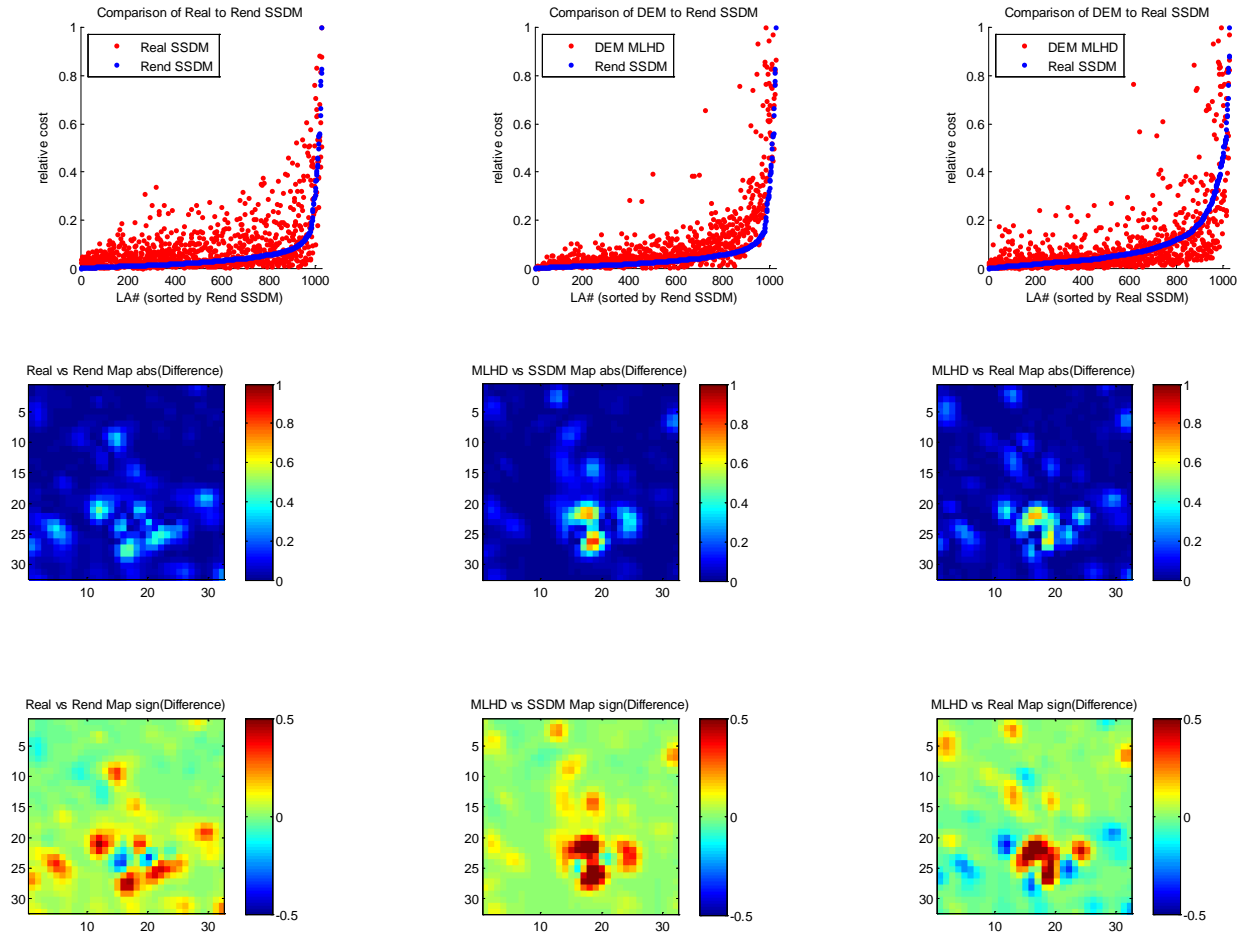


Figure 88 – DEM vs. Rendered vs. Real Weighted Cost Map differences

The portions of the comparison that are key are the lowest cost points and the highest cost points. The Table 11 shows the mean, standard deviation, and maximum absolute errors for the relative data comparisons between each weighted cost map for all the data, the best 10% of points, and the worst 10% of the points. The mean and standard deviation are close throughout the data. The mean, standard deviation, and maximum absolute error is low for the best 10% (the landing locations that would be chosen) of landing areas across all 3 comparisons.

Table 11 – Cost Comparison for Rendered vs. Real Image

Rend SDM vs. Real SDM				DEM MDM vs. Rend SDM				DEM MDM vs. Real SDM			
	All Data	Best 10%	Worst 10%		All Data	Best 10%	Worst 10%		All Data	Best 10%	Worst 10%
Mean Abs Error	0.059	0.027	0.15	Mean Abs Error	0.051	0.0022	0.25	Mean Abs Error	0.013	0.00077	0.11
Std Abs Error	0.075	0.019	0.12	Std Abs Error	0.077	0.00085	0.081	Std Abs Error	0.041	0.00046	0.083
Max Abs Error	0.48	0.096	0.48	Max Abs Error	0.38	0.0036	0.38	Max Abs Error	0.27	0.0018	0.27

This analysis in this section is just a comparison between the relative costs. This analysis was done to show that the rendering can be used for the lighting and view angle analysis key to demonstrating the power of the Size Density Method.

Comparison of SDM Relative Costs to MDM Absolute Costs

As is done in the main body of the thesis between the rendered images and DEM, this section does a comparison of the relative costs determined by the SDM against an absolute metric (% hazardous area) based on using the MDM.

Figure 89 shows the relative costs for the rendered (left) and real (right) SDM methods compared against the absolute metric. As can be seen, there are no outliers in the top-left corner of the plot, which means the method does a good job of sorting landing areas by relative safety and providing solutions that have a greater probability of finding more landing aim points in the chosen landing areas.

Note that this comparison does not weight the landing areas in the DEM MDM method against neighboring landing areas. The landing area costs are purely based on their own percentage of hazardous area and not of any of the neighboring landing areas.

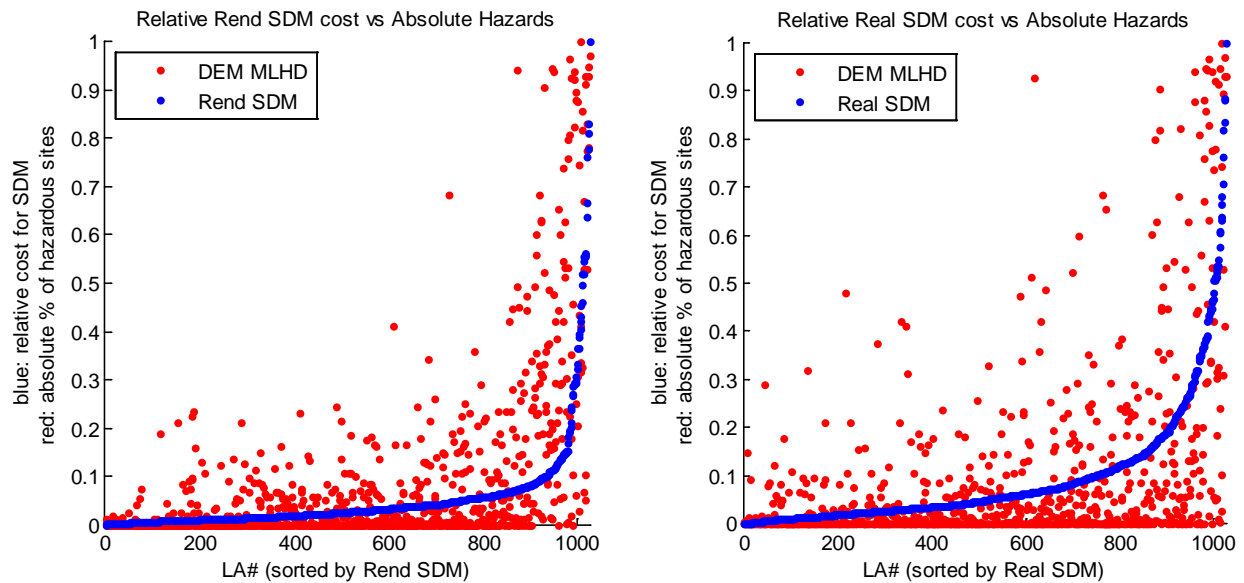


Figure 89 – Comparison of SDM Relative Costs to MDM Absolute Costs